University of Rome "La Sapienza"

Department of Physics

Graduate School in Astronomical, Chemical, Mathematical, Physical and Earth Sciences "Vito Volterra" - XXIX cycle

Doctoral Thesis

A Quantum Monte Carlo study of high pressure solid and liquid hydrogen

Giovanni Rillo

Advisors:
Prof. Andrea Pelissetto
Prof. Carlo Pierleoni

January 27, 2017

Contents

Introduction

Hydrogen is the first element of the periodic table. As such, it is often regarded as the simplest one: the non-relativistic hydrogen atom is a problem exactly solved in many textbooks; the hydrogen molecular ion H_2^+ and the diatomic molecule H_2 are, correspondingly, the first systems to be considered when more than one nucleus is involved. As a thermodynamic system, its phase diagram at low pressures is quite standard: at room temperature and ambient pressure, hydrogen is a molecular fluid; upon cooling, it becomes a molecular solid; its critical point is T=33 K and P=1.3 Pa [1].

Nevertheless, even such a simple system becomes really interesting when pressure is increased by several orders of magnitude. Speculations about the existence of a metallic solid state at 25 GPa and 0 K temperature started with Wigner and Huntington [2]; later calculations suggested that this state could become a high-temperature superconductor [3]. When experiments achieved the predicted transition temperature, they did not find a metallic state; on the other hand, they found a rich phase diagram, where several different solid phases exist [4, 5]. Nowadays, the quest for solid metallic hydrogen at low temperature is still an on-going activity.

As temperature is increased above ≈ 1000 K, the system enters the liquid phase: it is important to obtain an accurate equation of state at high temperature and high pressure, in order to model the properties of gas giants, such as Jupiter and Saturn, which are mostly made of hydrogen and helium. Metallic hydrogen, which is yet to be seen in the solid state, was experimentally measured in the liquid phase [6].

Performing experiments at such high pressures is complicated; the information obtained is partial. At low temperatures, the boundaries among the different solid phases can be drawn, but most of their structural properties are still an open problem; at high temperatures, characterizing the insulator-metal transition is hard because of large uncertainties and conflicting results.

Ab Initio simulations can be a valuable tool to complement and interpret experimental data; they can also guide experiments with their predictive power. For condensed matter, Density Functional Theory (DFT) is the method of choice to perform Ab Initio simulations at reasonable computational cost. However, their predictive power for high pressure hydrogen is questioned due to several levels of approximation which will be discussed in our work: in particular, the fact that DFT is plagued by an uncontrolled approximation (the exchange-correlation functional approximation) will be elaborated.

In this thesis, we will employ a different method to run Ab Initio simulations of high pressure hydrogen at finite temperature: the Coupled Electron Ion Monte Carlo (CEIMC). We will discuss how CEIMC, combining the Path Integral formalism to treat the nuclear degrees of freedom and the Variational Monte Carlo (VMC) method to accurately compute electronic energies in a Born-Oppenheimer framework, can perform finite temperature simulations without suffering from the same kind of uncontrolled approximation which plagues DFT. We will then apply the method to the low temperature, solid phase and to the high-temperature, liquid one. In the first case, finite temperature simulations of different candidate structures for the various solid phases will be performed, comparing CEIMC results with DFT ones. In the second case, the liquid-liquid phase transition will be investigated, drawing attention to the relationship between molecular dissociation and metallization; to do so, the system will be characterized across the transition with the computation of relevant optical properties.

This work is organized as follows. In Chapter 1, a short review of the experimental phase diagram of high pressure hydrogen is presented, discussing the strengths and the limitations of the experimental techniques employed, which information can be extracted and which cannot. In Chapter 2, the theoretical framework necessary to perform DFT and CEIMC simulations is discussed: Density Functional Theory and Variational Monte Carlo are introduced to compute electronic energies. In particular, the form of the trial wavefunction, the key ingredient of the VMC method, is discussed in detail. To account for quantum nuclear effects, the Path Integral formalism is introduced together with efficient ways of sampling the associated probability distribution: Path Integral Molecular Dynamics (PIMD) and Path Integral Monte Carlo (PIMC). In Chapter 3, after a small review of relevant previous theoretical calculations, we present our results about finite temperature simulations of different candidate structures for solid hydrogen. In particular, we performed DFT-PIMD and CEIMC simulations at T=200 K and T=414 K, analyzing the structural and electronic properties of the system and comparing at the same time the results produced by the two methods. Finally, in Chapter 4, we focus on the liquid-liquid phase transition. After reviewing previous literature, the system is characterized through the computation of optical properties across the transition, deducing its metallic or insulating state. The study of optical properties is also expanded in a larger region of the phase diagram.

Papers associated to the thesis work

- Liquid–liquid phase transition in hydrogen by coupled electron–ion Monte Carlo simulations, Pierleoni, Carlo, Morales, Miguel A., Rillo, Giovanni, Ho lzmann, Markus, Ceperley, David M., PNAS, vol. 113 | no. 18 | 4953–4957 (2016).
- Optical properties of liquid hydrogen across the molecular dissociation, G. Rillo, M.A. Morales, D.M. Ceperley and C. Pierleoni, in preparation
- Coupled Electron-Ion Monte Carlo simulation of the crystalline phases III and IV of molecular hydrogen, G. Rillo, M.A. Morales, D.M. Ceperley and C. Pierleoni, in preparation

Chapter 1

Hydrogen at high pressures

Interest in high pressure hydrogen was firstly drawn by Wigner and Huntington [2], who in 1935 speculated about a possible stable metallic phase of solid atomic hydrogen at pressures higher than 25 GPa. At the time, achieving such high pressures for hydrogen was experimentally unfeasible: H_2 was compressed at 2 GPa only in 1956 [7]. In the seventies, the development of diamond anvil cells allowed to generate pressures of hundreds of GPa under static conditions [8] (more precisely, up to 170 GPa at 25 °C). Solid hydrogen was thus obtained by Mao and Bell at a temperature of 25 °C and at a pressure of 50 GPa in 1979 [9]. The material was found to be transparent, a clear indication that the metallic state was yet to be reached, in contrast with the early prediction by Wigner. Since then, diamond anvil cells have been the standard tool to investigate high pressure hydrogen at relatively low temperatures. Technical improvements in DAC experiments pushed the highest reachable pressure further and further: nowadays, pressures above 300 GPa can be obtained consistently. A rich phase diagram with different solid phases was discovered, even if a full characterization of these phases is still missing.

High pressure hydrogen is also interesting at higher temperatures (thousands of kelvins), where the system is in its liquid phase. Knowledge of hydrogen in this regime is relevant for modeling the interiors of planets like Saturn and Jupiter, made up hydrogen (90 %) and helium (9%). This region of the phase diagram can nowadays be probed using DAC [10, 11], as in the solid case, using special heating techniques. A more complete picture of the liquid state can be achieved using dynamic shock compression, a technique that allows one to drive the system to pressures of ≈ 500 GPa and temperatures of ≈ 10000 K [12, 13]. Using this method, liquid metallic hydrogen was detected at 140 GPa and 3000 K [6]. However, large uncertainties usually affect measurements due to the very dynamic nature of the process: while the existence of metallic hydrogen was proven, the transition from an insulating to a metallic liquid is still poorly characterized, with different experiments obtaining conflicting results [10, 14].

In the following sections, we will discuss the experimental phase diagram of high pressure hydrogen, both in the solid and in the liquid region. The experimental evidence will be described, pointing out at the same time missing relevant features that are still object of discussion.

1.1 Experimental solid phase diagram

When looking for crystal structures of solid phases, the two techniques of choice are X-ray diffraction and neutron scattering. In particular, X-ray diffraction probes the electronic density and, for molecular systems, can identify the positions of the molecular centers; neutron scattering, being sensitive to the positions of the individual nuclei, gives information about the single atoms. Unfortunately, the hydrogen cross-section is extremely low in both cases: X-ray diffraction was performed up to 180 GPa [15], while neutron scattering up to 60 GPa [16]. At higher pressures, structural information is extracted through Raman and infrared (IR) spectra.

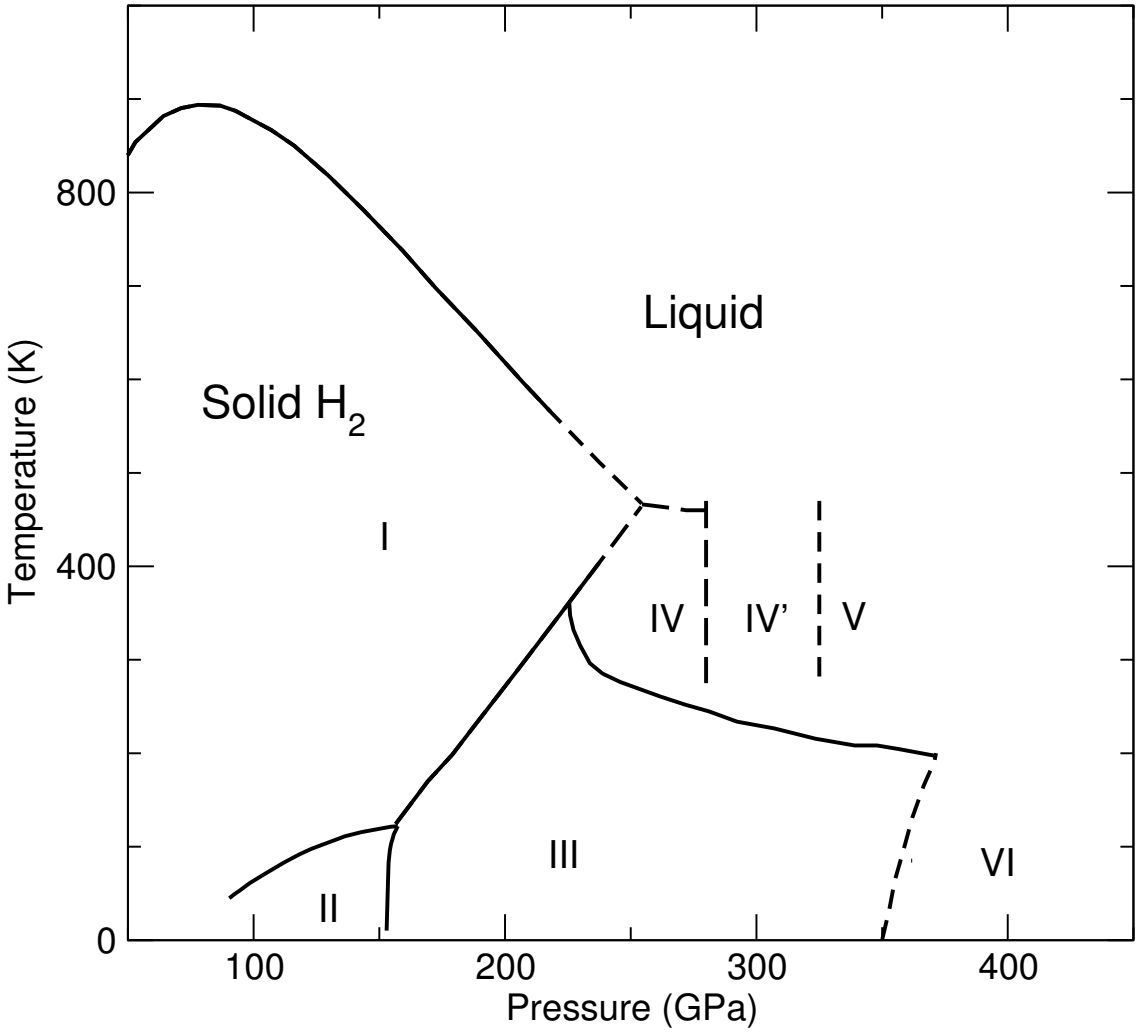

FIGURE 1.1: Experimental phase diagram of solid hydrogen. Black continuous lines indicate the melting line as well as the transition lines between different experimentally detected [4, 5] crystalline phases: I–IV. New phases and boundaries indicated by dashed black lines are still speculative: the last portion of the melting line and the IV-IV' line is proposed in [5]; phase V and the associated transition line is proposed by [17]; phase VI is observed by [18] and [19], even if with conflicting properties.

1.1.1 Phase I

At relatively low pressures and temperatures, interactions are weak and the molecular angular momentum J can be regarded as a good quantum number: we can then talk about para-hydrogen $p-H_2$ (even J) or ortho-hydrogen $o-H_2$ (odd J) as we usually do when dealing with isolated molecules. Since transitions between odd and even J states are prohibited for isolated molecules, conversion from one species to another is very slow at low pressures and the two species can be studied separately or in mixtures with constant concentrations.

At room temperature and atmospheric pressure, hydrogen is a diatomic gas; at first, solid hydrogen was obtained at approximately zero pressure by cooling the system at helium temperatures. Early X-ray diffraction studies showed that at these temperatures the molecular centers were arranged according a hexagonal close packed structure (hcp) regardless of the ortho-para ratio [20–22]. Using diamond anvil cells, solid hydrogen was observed at room temperature [9] at 5.7 GPa; subsequent X-ray diffraction studies were performed, reaching pressures of tens of GPas [23,24], finding the same hcp structure reported at zero pressure and helium temperatures. These results can be integrated with observations coming from Raman and infrared spectra experiments, which are successfully used to probe rotational and vibrational properties of molecular systems. For high pressure hydrogen, these spectra can be consistently interpreted assuming the anisotropic part of the intermolecular interaction to be negligible. In this case, in fact, only the molecular radial coordinates are coupled, resulting in a collection of independent quantum rotors [22, 25]. Para-hydrogen molecules, being in a $J = 0$ ground state, have spherical symmetry; on the other hand, the $J = 1$ degenerate states of ortho-hydrogen molecules are equally populated, producing a spherical symmetry also in this case. The consistency of this approach is verified at low pressures and temperatures, obtaining sharp rotovibrational Raman peaks [26, 27]: this indicates that the mixing of different rotational levels is small. At higher temperatures and pressures, a continuous broadening of the rotational peaks takes place [28], corresponding to an increasing strength of the neglected anisotropic interaction, which could drive the system towards a rotationally ordered system. This solid phase of free quantum rotors is known as phase I.

1.1.2 The broken symmetry phases: phase II and III

Measurements of Raman and infrared spectra can be performed beyond the pressure and temperature range imposed by X-ray diffraction, probing vibrational properties of the system in a larger portion of the phase diagram. Vibrational properties are sensitive to changes in crystal structure or rotational order: the region of stability of phase I can thus be naturally prolonged as long as the vibrational spectra do not display significant changes; on the other hand, discontinuities in these quantities are related to phase transitions.

This is the case, for example, for deuterium and hydrogen below 140 K in a pressure range of 40-150 GPa: the position of the Raman and IR peaks associated with the vibration of the molecular bond (typically referred to as vibrons) shows a discontinuity of tens of cm^{-1}; at the same time, a cusp is observed in its temperature dependence and several changes take place in the low-frequency spectrum [4, 29–35]. In particular, the appearance of new peaks at low frequency is associated to the presence of librons, phonons associated to a restricted orientational motion: for this reason

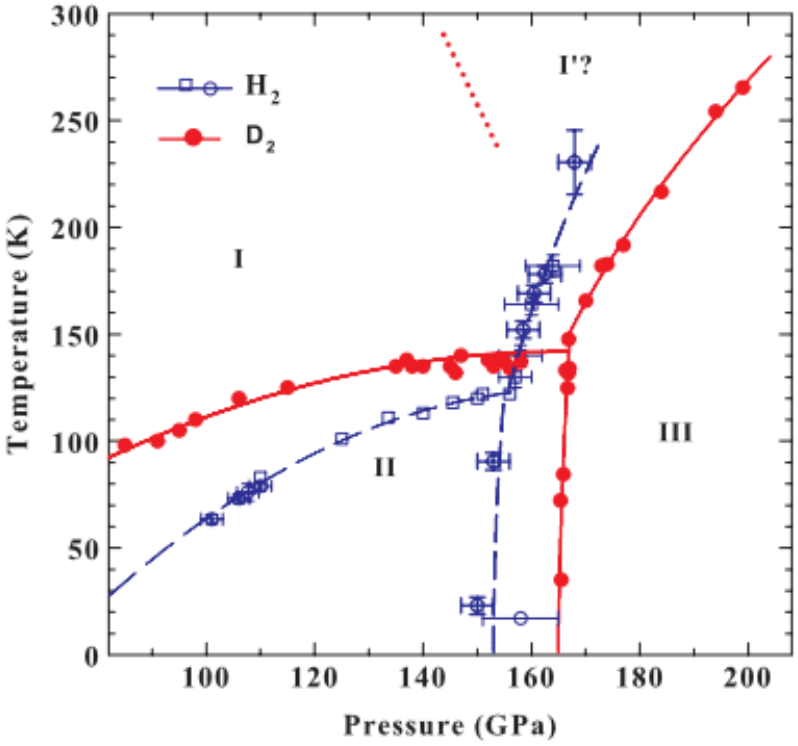

FIGURE 1.2: Phase boundaries of low temperature solid phases for normal hydrogen and deuterium, based on optical Raman and IR spectra. Picture from [29].

the transition to the new phase, called phase II, is supposed to involve orientational ordering, even for spherical $J = 0$ species (para-hydrogen and ortho-deuterium). This is consistent with the expectation that at high enough pressures the electric quadrupole-quadrupole interaction would mix different rotational states, resulting in an ordered, anisotropic state.

The boundaries of phase II, based on optical spectra, are depicted in fig. 1.2 for normal H_2 and D_2 with an equilibrium ortho-para concentration. While Raman and IR experiments signal the transition, they can at best provide constraints for the symmetry of the structure. An early candidate for phase II was the Pa_3 structure, where the molecular centers are on the sites of a face centered cubic crystal while the molecules are oriented according to a specific pattern; this is the structure found for the orientational ordered phase of ortho-hydrogen and para-deuterium at ambient pressure and $T < 3 - 4$ K [30]. Unfortunately, a group theory analysis of the number of Raman and IR peaks deemed this structure incompatible with experimental results [36]. Recent X-ray diffraction and neutron scattering studies [15, 16] suggest that the hcp lattice is retained, with molecules being locally oriented similarly to Pa_3.

Following the argument of increasing anisotropic interaction when increasing pressure, a break of the rotational symmetry is expected even at higher temperature. This is indeed the case: a transition to a new phase, phase III, is detected for hydrogen around 150 GPa. The transition, however, takes place at high and low temperatures, starting from both phase I and II (see fig. 1.2): it seems to involve more than only rotational ordering. Similarly to the I-II transition, the I-III and II-III transitions are characterized by a discontinuity in the vibron frequency (that can be of hundreds of cm^{-1}), a change in the slope of the vibron dependence on temperature and

a change of the low frequency spectrum, even larger than in the I-II transition [29, 30, 34]. The more pronounced features may correspond to a larger structural change. Moreover, a peculiarity of transitions to phase III is the sudden increase in IR absorption (three orders of magnitude) for the vibronic peak [4, 18, 33], which hints at a primitive cell with a large (compared to the other phases, at least) dipole moment. An X-ray diffraction experiment [15] found that molecular centers in phase III remain close to the hcp lattice sites, at least up to 183 GPa; no direct information about molecular orientation could be extracted. A classical orientational ordering process is speculated to take place [37]. Phase III is transparent [4, 38] and insulating in the experimentally accessible thermodynamic conditions. Phases I, II, and III coexist at a triple point at 125 K and 155 GPa for H_2 (135 K and 165 GPa for D_2)

1.1.3 Mixed phases: phase IV and IV'

In 2011, Eremets et al. [39] reported the observation of a semiconducting phase of hydrogen at T=295 K above 220 GPa, using photoconductivity and resistance measurements; a metallic state was claimed to be produced above 260 GPa. At the same time, significant changes in the low frequency Raman peaks take place at the transitions. Subsequent Raman and IR studies [5, 40–42] show that when the first transition occurs at 220 GPa, a new high-frequency peak appears at ≈ 4150 cm^{-1}, next to the vibron peak present in phase III, which displays a discontinuity of hundreds of cm^{-1} and softens very rapidly after the transition. The presence of two high frequency peaks is interpreted as the existence of two different local atomic environments: in particular, theoretical calculations [43] suggest the possible stability of layered mixed structures, where atoms belonging to different layers are bonded in a different manner. This topic will be treated in more detail in chapter 3. More recent optical measurements [38, 41] contradict the reported metallicity; semimetallic or semiconducting behaviour is still not ruled out. This new phase is labelled as phase IV. At the same time, the change in intensity and number of the low frequency phononic peaks at higher pressure was confirmed [5, 41] and the new phase resulting from the transition is labelled as IV' or V. The experimental boundaries of the distinct five solid phases are pictured in fig. 1.1.

1.1.4 Possible phases at higher pressures

With the improvement of DAC techniques, the experimental exploration of the solid region of hydrogen phase diagram is still an on-going activity, reaching higher and higher pressures. Different experiments display conflicting results. Eremets et al. [18] study hydrogen at pressures up to 380 GPa and T<200 K with Raman scattering. For P>360 GPa they find that the intensity of the Raman spectra goes to zero when cooling the system below 200 K; at the same time, a strong drop in resistance is observed in the same thermodynamic conditions (P>360 GPa and T<200 K). They thus draw a vertical transition line in the P-T plane, introducing a new conducting phase VI for pressures higher than P=360 GPa. Dalladay-Simpson et al. [17] investigate the system at $T \geq 300$ K. They propose a new phase (V) for P>325 GPa, based on arguments similar for phase transitions at lower pressures: change in the low frequency peaks, change in the slope of the pressure dependence of the vibron, broadening and weakening of the vibrational peak itself. The Raman intensity, in general, decreases: this, coupled to the weak vibronic signal, is interpreted as

quasi-atomic state, precursor of a fully non molecular, metallic system. Dias et al. [19] probe the system at low temperature (T<200 K), as in [18], using infrared radiation. Above 355 GPa, the IR vibron disappears, and two new peaks close to 3000 cm^{-1} appear; they come up with a vertical transition line, similar to [18]. At variance with [18], though, no evidence of metallicity is found.

As we can see, the region of the phase diagram at low temperature ($T \approx 200$ K) and high pressure (P>300 GPa) displays interesting phenomena, either the long-yearned-for metallic transition or a "simple" structural transition; moreover, we must not forget that even the crystal lattice corresponding to phase III, which is relatively well established in the solid phase diagram, is still an object of debate. At higher temperatures, experiments point to the stability of mixed structures, whose finite temperature properties may be difficult to predict. These will be the starting points of our discussion in chapter 3.

1.2 Liquid-liquid phase transition

As anticipated in the first paragraph, metallic hydrogen was first produced in the liquid state [6]: using multiple shock compression, liquid hydrogen was compressed to 140 GPa and heated to 3000 K; a sharp drop in resistivity ($\approx 500 \mu\Omega cm$) was observed, a clear signal of the metallic state.

Nevertheless, a clear characterization of the insulator-metal (IM) transition is still missing and many questions remain open. Traditionally, dynamic compression experiments are plagued by large uncertainties: for example, temperature is usually estimated through equations of state and not actually measured, introducing systematic source of errors. This is apparent in fig. 1.3 for the yellow and maroon signs. The improvement in static compression using DAC allows to perform such experiments in the liquid phase as well (green and purple signs for hydrogen in fig. 1.3). In particular, laser heated experiments are performed: the sample is usually in contact with a metallic absorber embedded in the diamond anvil cell; the absorber is heated through laser pulses, and the sample is heated by direct contact. The natural effect is that the temperature of the sample rises; Dzyabura et al. [47] found that the temperature does not increase indefinitely while heat is provided, but a plateau is reached. This can be interpreted as latent heat, provided to make a first-order phase transition happen. Rigorous evidence of metallization, however, required a systematic study of optical properties, which could not be performed due to mechanical instabilities. Ohta et al. [11] performed similar experiments at higher temperatures (T>2000 K, see fig. 1.3), finding the same saturation of the maximum reachable temperature. In particular, they assume that the transition under examination is the molecular dissociation of liquid hydrogen; while stating that this could be related to the insulator-metallic transition, they do not provide any measurement of optical quantities.

Zaghoo et al. [10] repeated the laser-heating experiments, integrating the temperature plateaus with measurements of optical reflectivity. Reflectivity, which may provide indications about the metallic state of the system, was measured using a second laser pulse to probe the system. In particular, they start from a transparent sample and, while heating, they measure an increase in reflectivity, that saturates to 0.5. As we can see from fig. 1.3, their results for the liquid-liquid phase transition are compatible with Ohta's; measuring the reflectivity, they provide evidence to link molecular dissociation with metallization of hydrogen.

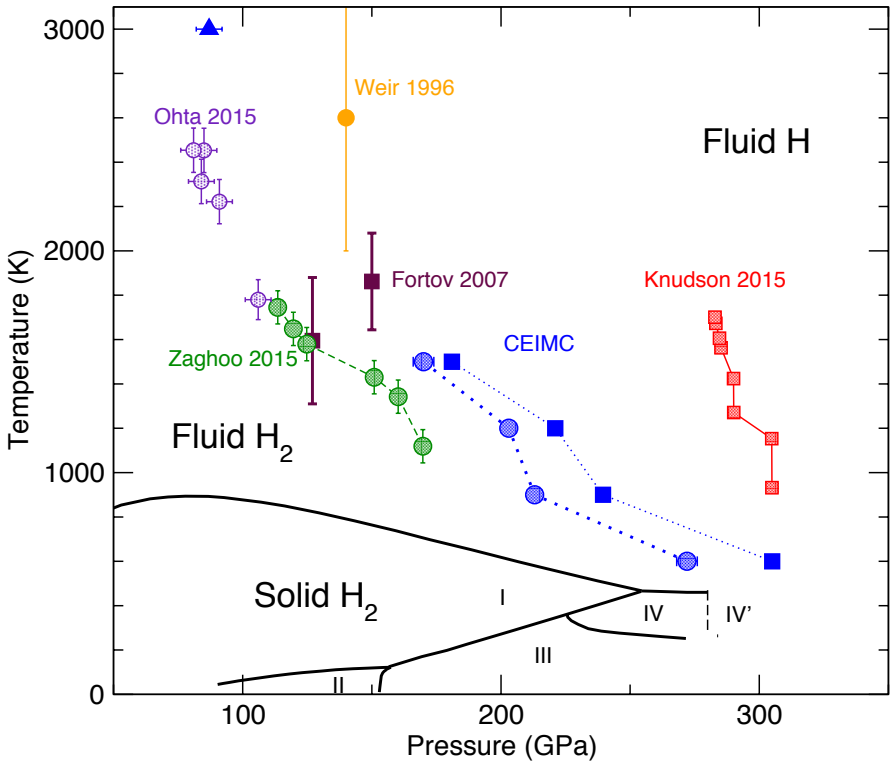

FIGURE 1.3: Hydrogen phase diagram with experimental liquid–liquid transition lines and CEIMC predictions. Blue circles and squares are CEIMC predictions for the liquid–liquid transition line in hydrogen and in deuterium, respectively. DAC experimental results for hydrogen are indicated by green circles [10] and purple circles [11], whereas red squares indicate shock wave experimental data for deuterium [14]. We also report an earlier experimental point for the conductivity onset in liquid hydrogen (yellow circle) [6] and two points for deuterium dissociation and metallization (maroon squares) [44]. The error bars on the temperature for the latter two sets of data reported here were inferred from theories [45]. In fact, all dynamical experiments [6, 14, 44] used models to determine T. The blue triangle at 3000 K indicates the CEIMC prediction for a metallization cross-over above the critical point where the conductivity is $2-4\times10^3(\Omega cm^{-1})$. Figure from [46]

Reflectivity measurements for deuterium by Knudson et al. [14] using dynamical compression find a transition line which is 150 GPa apart from Zaghoo's findings; an isotopic effect is not probable, since previous dynamical compression experiments on deuterium by Fortov [44] found a transition point closer to Zaghoo's line.

A challenging problem with optical measurements is that the different parts of the experimental apparatus must be considered when extracting the sample response from the raw data. Moreover, hydrogen is assumed to have perfect transmittance and zero reflectivity at the wavelength of the probe before the transition; an hypothesis that will be discussed in chapter 4, where we will show our results for the liquid-liquid phase transition, obtained from Ab Initio simulations. We will also provide optical properties, that may help in disentangling the actual contribution of the sample from the rest of the apparatus.

Chapter 2

Simulation methods

Ab Initio computer simulations are a valuable tool to study condensed matter systems. They can cooperate in synergy with experiments, helping in the interpretation of experimental data and providing missing information. But they can also achieve predictive power when exploring new territories, working as an input to design new experiments. Currently, the most popular Ab Initio method is Density Functional Theory (DFT). While the theoretical foundations of the method were laid in 1964 by Hohenberg and Kohn [48], its practical implementation proposed in 1965 by Kohn and Sham [49], it was in the 1990s that DFT became extremely popular : DFT computations on small molecular systems employing hybrid exchange-correlation functionals (such as B3LYP) outperformed other more computationally expensive Ab Initio methods (Hartree-Fock, Self Consistent Field) when compared against experiments [50, 51]. However, even DFT has limitations which will be described in the following sections. In this chapter we give an overview the computational challenges inherent to high pressure hydrogen and introduce the techniques used to deal with them.

2.1 The electronic problem and the Born-Oppenheimer approximation

We consider a system of N_e, spin unpolarized, electrons and N_p protons in a fixed volume Ω in thermal equilibrium at temperature T. In atomic units, the Hamiltonian of the system is

$$\hat{\mathcal{H}} = \hat{\mathcal{K}}_p + \hat{\mathcal{H}}_e \qquad \hat{\mathcal{H}}_e = \hat{\mathcal{K}}_e + \hat{\mathcal{V}} \tag{2.1}$$

$$\hat{\mathcal{K}}_p = -\frac{1}{2M_p}\sum_{\alpha=1}^{N_p}\vec{\nabla}^2_{\vec{R}_\alpha} \qquad \hat{\mathcal{K}}_e = -\frac{1}{2}\sum_{i=1}^{N_e}\vec{\nabla}^2_{\vec{r}_i} \tag{2.2}$$

$$\hat{\mathcal{V}} = \frac{1}{2}\sum_{i\neq j}^{N_e}\frac{1}{|\vec{r}_i-\vec{r}_j|} - \sum_{i=1}^{N_e}\sum_{\alpha=1}^{N_p}\frac{1}{|\vec{r}_i-\vec{R}_\alpha|} + \frac{1}{2}\sum_{\alpha\neq\beta}^{N_p}\frac{1}{|\vec{R}_\alpha-\vec{R}_\beta|} \tag{2.3}$$

where $\vec{r}_i$ and $\vec{R}_\alpha$ are positions for the i-th electron and the α-th proton respectively. This leads to the following time-independent Schrodinger equation written in the electronic and nuclear position basis set:

$$\hat{\mathcal{H}}(\mathbf{R},\mathbf{r})\Phi_k(\mathbf{R},\mathbf{r}) = E_k\Phi_k(\mathbf{R},\mathbf{r}) \tag{2.4}$$

where $\mathbf{R}$ and $\mathbf{r}$ stand for the collection of all nuclear and electronic coordinates, respectively. Solving eq. 2.4 even for small molecules is beyond current computational capabilities: at this point the Born-Oppenheimer approximation [52–54] is introduced to make the problem tractable. We define the wavefunctions $\Psi_n(\mathbf{r};\mathbf{R})$ as

$$\hat{\mathcal{H}}_e\Psi_n(\mathbf{r};\mathbf{R}) = (\hat{\mathcal{K}}_e + \hat{\mathcal{V}})\Psi_n(\mathbf{r};\mathbf{R}) = E_n^e(\mathbf{R})\Psi_n(\mathbf{r};\mathbf{R}) \tag{2.5}$$

i.e. they are eigenfunctions of the operator $\hat{\mathcal{H}}_e$. Since $\hat{\mathcal{H}}_e$ contains the nuclear coordinates in the potential term, both the eigenvalue $E_n^e(\mathbf{R})$ and the eigenfunction Ψ_n parametrically depend of the nuclear coordinates. Expanding the total wavefunction $\Phi_k(\mathbf{R},\mathbf{r})$ as a linear combination of wavefunctions $\Psi_n(\mathbf{r};\mathbf{R})$

$$\Phi_k(\mathbf{R},\mathbf{r}) = \sum_n \chi_{kn}(\mathbf{R})\Psi_n(\mathbf{r};\mathbf{R}) \tag{2.6}$$

and plugging eq. 2.6 in eq. 2.4 we obtain

$$\sum_n \hat{\mathcal{K}}_p\left(\chi_{kn}(\mathbf{R})\Psi_n(\mathbf{r};\mathbf{R})\right) + \sum_n \chi_{kn}(\mathbf{R})E_n^e\left(\mathbf{R}\right)\Psi_n(\mathbf{r};\mathbf{R}) = \sum_n E_k\chi_{kn}(\mathbf{R})\Psi_n(\mathbf{r};\mathbf{R}) \tag{2.7}$$

The action of the nuclear kinetic operator on the total wavefunction produces the following terms:

$$\begin{aligned}
&\hat{\mathcal{K}}_p\left(\chi_{kn}(\mathbf{R})\Psi_n(\mathbf{r};\mathbf{R})\right) = -\frac{1}{2M_p}\sum_\alpha^{N_\alpha}\nabla^2_{\mathbf{R}_\alpha}\left(\chi_{kn}(\mathbf{R})\Psi_n(\mathbf{r};\mathbf{R})\right) = \\
= \;& -\frac{1}{2M_p}\sum_\alpha^{N_\alpha}\left(\nabla^2_{\mathbf{R}_\alpha}\chi_{kn}(\mathbf{R})\right)\Psi_n(\mathbf{r};\mathbf{R}) - \frac{1}{2M_p}\sum_\alpha^{N_\alpha}\left(\nabla^2_{\mathbf{R}_\alpha}\Psi_n(\mathbf{r};\mathbf{R})\right)\chi_{kn}(\mathbf{R}) - \\
- \;& \frac{1}{M_p}\sum_\alpha^{N_\alpha}\left(\nabla_{\mathbf{R}_\alpha}\chi_{kn}(\mathbf{R})\right)\cdot\left(\nabla_{\mathbf{R}_\alpha}\Psi_n(\mathbf{r};\mathbf{R})\right)
\end{aligned} \tag{2.8}$$

Multiplying eq. 2.7 by $\Psi_m(\mathbf{r};\mathbf{R})$, integrating the electronic coordinates and rearranging the terms, we get

$$(\hat{\mathcal{K}}_p + E^e_m(\mathbf{R}) - E_k)\chi_{km}(\mathbf{R}) = \frac{1}{2M_p}\sum_n\sum_\alpha^{N_\alpha}\chi_{kn}(\mathbf{R})\int d\mathbf{r}\Psi_m(\mathbf{r};\mathbf{R})\nabla^2_{\mathbf{R}_\alpha}\Psi_n(\mathbf{r};\mathbf{R}) + \\ +\frac{1}{M_p}\sum_n\sum_\alpha^{N_\alpha}\nabla_{\mathbf{R}_\alpha}\chi_{kn}(\mathbf{R})\cdot\int d\mathbf{r}\Psi_m(\mathbf{r};\mathbf{R})\nabla_{\mathbf{R}_\alpha}\Psi_n(\mathbf{r};\mathbf{R}) \tag{2.9}$$

If we ignore the r.h.s. of eq. 2.9, we obtain an eigenvalue problem for the nuclear coordinates corresponding to a "clamped nuclei" Hamiltonian $\hat{\mathcal{H}}_{cn} = \hat{\mathcal{K}}_p + E^e_m(\mathbf{R})$ with a potential given by the electronic eigenvalue $E^e_m(\mathbf{R})$: this is the Born-Oppenheimer approximation. The terms on the r.h.s. provide both adiabatic and non adiabatic corrections, coupling different electronic eigenstates. If there are no magnetic fields, we can choose to work with real wavefunctions and it is easy to prove by integration by parts that diagonal terms like $\int d\mathbf{r}\Psi_m(\mathbf{r};\mathbf{R})\nabla_{\mathbf{R}_\alpha}\Psi_m(\mathbf{r};\mathbf{R})$ are identically zero. It can be shown that the other non diagonal terms are [54]

$$\langle\Psi_m|\mathcal{K}_p\Psi_n\rangle \propto \frac{1}{E_m - E_n}\langle\Psi_m|\left[-i\nabla_{\mathbf{R}_\alpha}, \hat{\mathcal{H}}\right]\Psi_n\rangle \tag{2.10}$$

The numerator depends only mildly on the nuclear coordinates: thus, if the electronic energy surfaces are well separated, the non diagonal terms are negligible because of the denominator. However, this is not valid for metals, which are an important class of systems: one of the motors driving research on high pressure hydrogen is predicting when the system becomes metallic. In this case, an argument can be made that the most relevant excitations are single-electron ones, which are barely coupled to the nuclear motion [54] . Collective excitations, such as plasmons, are of high energy (some eVs) and the previous line of reasoning stays true.

In this approximation, the original problem can be simplified and resolved in the following way:

- (i) given the configuration $\mathbf{R}$, solve eq. 2.5 and find the electronic ground wave function $\Psi_0(\mathbf{r};\mathbf{R})$
- (ii) assuming that the electrons are in the ground state, use $\Psi_0(\mathbf{r};\mathbf{R})$ to solve

  $$\left(\hat{\mathcal{K}}_p + E^e_0(\mathbf{R}) - E_0\right)\chi_{k0}(\mathbf{R}) = 0$$

  and find the nuclear wavefunction $\chi_{k0}(\mathbf{R})$

The above procedure can be followed to obtain electronic and nuclear wavefunctions for pure states. When different quantum states have finite probabilities of being occupied, density matrices are employed [55]:

$$\hat{\rho} = \sum_s p_s\,|\Phi_s\rangle\,\langle\Phi_s| \tag{2.11}$$

where p_s is the probability of finding the system in the state $|\Phi_s\rangle$. If we work in the canonical ensemble, the density matrix is

$$\hat{\rho}_c = \sum_s e^{-\beta E_s} |E_s\rangle \langle E_s| = e^{-\beta \hat{\mathcal{H}}} \tag{2.12}$$

where $|E_s\rangle$ is the an eigenstate of the total Hamiltonian. The physical properties of the system are obtained as statistical averages

$$O = \langle \hat{\mathcal{O}} \rangle = \frac{\mathrm{Tr}\left[\hat{\mathcal{O}}\hat{\rho}_c\right]}{\mathrm{Tr}\left[\hat{\rho}_c\right]} \tag{2.13}$$

over the measure given by the thermal density matrix $\hat{\rho}_c$. In the spirit of the Born-Oppenheimer approximation we assume that electrons are in their ground state, while nuclei are at finite temperature. This corresponds to writing the partition function $\mathcal{Z}$ of the system as

$$\mathcal{Z} = \mathrm{Tr}\left[\hat{\rho}_c\right] \approx \int d\mathbf{R} \langle \mathbf{R}| \langle \Psi_0| e^{-\beta \mathcal{H}} |\Psi_0\rangle |\mathbf{R}\rangle \tag{2.14}$$

The matrix element $\langle \Psi_0| e^{-\beta \mathcal{H}} |\Psi_0\rangle$ can be written in a Taylor expansion:

$$\langle \Psi_0| e^{-\beta \mathcal{H}} |\Psi_0\rangle = \sum_l \frac{(-\beta)^l}{l!} \langle \Psi_0| \left(\hat{\mathcal{K}}_p + \hat{\mathcal{H}}_e\right)^l |\Psi_0\rangle \tag{2.15}$$

The single term can be evaluated:

$$\begin{aligned}
\langle \Psi_0| \left(\hat{\mathcal{K}}_p + \hat{\mathcal{H}}_e\right)^l |\Psi_0\rangle = \langle \Psi_0| \left(\hat{\mathcal{K}}_p + \hat{\mathcal{H}}_e\right)^{l-1} \left(\hat{\mathcal{K}}_p + \hat{\mathcal{H}}_e\right) |\Psi_0\rangle = \\
\langle \Psi_0| \left(\hat{\mathcal{K}}_p + \hat{\mathcal{H}}_e\right)^{l-1} \textstyle\sum_{l'} |\Psi_{l'}\rangle \langle \Psi_{l'}| \left(\hat{\mathcal{K}}_p + \hat{\mathcal{H}}_e\right) |\Psi_0\rangle \approx \\
\approx \langle \Psi_0| \left(\hat{\mathcal{K}}_p + \hat{\mathcal{H}}_e\right)^{l-1} \textstyle\sum_{l'} |\Psi_{l'}\rangle \langle \Psi_{l'}|\Psi_0\rangle \left(\hat{\mathcal{K}}_p + E_0^e(\mathbf{R})\right) = \\
\langle \Psi_0| \left(\hat{\mathcal{K}}_p + \hat{\mathcal{H}}_e\right)^{l-1} |\Psi_0\rangle \left(\hat{\mathcal{K}}_p + E_0^e(\mathbf{R})\right)
\end{aligned} \tag{2.16}$$

We ignored the action of the nuclear kinetic operator $\hat{\mathcal{K}}_p$ on the electronic wavefunction Ψ_0, which is consistent with neglecting the terms in the r.h.s. of eq. 2.9. Iterating the process, one can easily prove that the density matrix in the Hilbert space of the nuclear degrees of freedom reduces to

$$\langle \Psi_0| e^{-\beta \mathcal{H}} |\Psi_0\rangle \approx \hat{\rho}_{BO} \propto e^{-\beta(\hat{\mathcal{K}}_p + E_0^e(\mathbf{R}))} \tag{2.17}$$

In this way the trace can be written as the sum over different nuclear configurations only, with the potential energy surface $E_0^e(\mathbf{R})$ which plays the role of the effective interaction among nuclei. Any ab-initio method based on the BO approximation needs to address the problem of calculating $E_0^e(\mathbf{R})$ while keeping the nuclear coordinates fixed. Resolving the many-body electronic Schrodinger equation for large extended systems still remains a computational challenge with the resources currently available. As already remarked, nowadays the most widespread Ab Initio method is Density Functional Theory (DFT), whose theoretical foundations were laid in 1964 by Hohenberg and Kohn [56].

2.2 Density Functional Theory

To solve eq. 2.5 for a system with N_e electrons, one must deal with the $3N_e$ electronic coordinates. Any finite element method based on a numerical discretization of the many-body wavefunction is doomed to fail for extended systems with tens, hundreds of particles due to the exponential use of memory necessary to store the variables. Density functional theory provides an alternative path: instead of considering the electronic ground state wavefunction $\Psi_0(\mathbf{r};\mathbf{R})$, the main quantity in this approach is the ground state single electron density

$$n_0(\vec{r}) = \sum_{i=1}^{N_e} \langle \Psi_0 | \delta(\vec{r}_i - \vec{r}) | \Psi_0 \rangle \tag{2.18}$$

From a theoretical point of view, knowledge of $n_0(\vec{r})$ proves to be sufficient to derive any other ground state property of the system as a functional of $n_0(\vec{r})$ itself (in particular, the ground state energy $E_0^e = E^e[n_0]$). Computationally, this resolve the issue of dealing $3N_e$ variables, reducing it to a three dimensional problem. On the other hand, an explicit, exact functional form is missing, forcing any actual implementation of DFT to make use of uncontrolled approximations.

In the next section, a proof of the Hohenberg-Kohn theorem, which establishes the formal connection between $n_0(\vec{r})$ and any other ground state quantity, will be given.

2.2.1 The Hohenberg-Kohn theorem

To give a more general scope to the theorem, the electronic Hamiltonian is rewritten as

$$\hat{\mathcal{H}}_e = \hat{\mathcal{K}}_e + \hat{\mathcal{V}} + \hat{\mathcal{W}} \tag{2.19}$$

where

$$\hat{\mathcal{K}}_e = -\frac{1}{2}\sum_{i=1}^{N_e} \vec{\nabla}^2_{\vec{r}_i} \quad , \quad \hat{\mathcal{V}} = \sum_{i=1}^{N_e} v(\vec{r}_i) \quad , \quad \hat{\mathcal{W}} = \sum_{i=1,j>i}^{N_e} \frac{1}{|\vec{r}_i - \vec{r}_j|} \tag{2.20}$$

$\hat{\mathcal{K}}_e$ is the usual kinetic energy. $\hat{\mathcal{V}}$ is the external potential, which can be written as a sum of one-particle terms. In particular, its average value over the ground state wavefunction $|\Psi_0\rangle$ can be written as

$$\begin{aligned}\langle \Psi_0 | \hat{\mathcal{V}} | \Psi_0 \rangle = \langle \Psi_0 | \sum_{i=1}^{N_e} v(\vec{r}_i) | \Psi_0 \rangle = \int d\vec{r}\, \langle \Psi_0 | \sum_{i=1}^{N_e} v(\vec{r}) \delta(\vec{r} - \vec{r}_i) | \Psi_0 \rangle = \\ \int d\vec{r} v(\vec{r}) \, \langle \Psi_0 | \sum_{i=1}^{N_e} \delta(\vec{r} - \vec{r}_i) | \Psi_0 \rangle = \int d\vec{r} v(\vec{r}) n_0(\vec{r})\end{aligned} \tag{2.21}$$

In the Born-Oppenheimer approximation, this is generally the potential generated by the nuclei but it can also include any other external field. Finally, $\hat{\mathcal{W}}$ is the coulombic repulsion among different electrons. Note that, within the class of Hamiltonians defined in eq. 2.19, the only difference is

the external potential $\hat{\mathcal{V}}$: thus, any observable $\mathcal{A}$ can be seen as $\mathcal{A}[v]$, a functional of $v(\vec{r})$, since everything else is fixed.

The theorem can be enunciated as follows [48, 57, 58]:

HK theorem:. (i) The ground state electronic density $n(\vec{r})$ uniquely determines the external potential $v(r)$, to within an additive constant, i.e. $v(r)$ is a unique functional of $n(\vec{r})$

(ii) The ground state energy E_0 is the minimum of the functional $E[n]$ for all v-representable densities $n(\vec{r})$

Not any electronic density $n(\vec{r})$ one can come up with can be thought as the ground state density of some Hamiltonian that has the form defined in eq. 2.19. A "v-representable density $n(\vec{r})$" enforces precisely this restriction.

The first statement can be proved in the following way, using reductio ad absurdum: we suppose that two potentials $\hat{\mathcal{V}}$ and $\hat{\mathcal{V}}'$ corresponding to the same $n_0(\vec{r})$ exist and $\hat{\mathcal{V}} \neq \hat{\mathcal{V}}' + const$. We then have two Hamiltonians $\hat{\mathcal{H}} = \hat{\mathcal{K}}_e + \hat{\mathcal{V}} + \hat{\mathcal{W}}$ and $\hat{\mathcal{H}}' = \hat{\mathcal{K}}_e + \hat{\mathcal{V}}' + \hat{\mathcal{W}}$ and two ground state wavefunctions $|\Psi_0\rangle$ and $|\Psi_0'\rangle$ with energies E_0^e and $E_0^{e'}$, First of all, we show that the two Hamiltonians cannot have a common ground state, i.e. $|\Psi_0\rangle \neq |\Psi_0'\rangle$. If that were the case and $|\Psi_0\rangle = |\Psi_0'\rangle$,

$$(\hat{\mathcal{H}} - \hat{\mathcal{H}}')\,|\Psi_0\rangle = (\hat{\mathcal{V}} - \hat{\mathcal{V}}')\,|\Psi_0\rangle = \sum_{i=1}^{N_e}(v(\vec{r}_i) - v'(\vec{r}_i))\Psi_0(\mathbf{r}) = (E_0^e - E_0^{e'})\Psi_0(\mathbf{r}) \tag{2.22}$$

i.e. $v(\vec{r}) - v'(\vec{r}) = const$ when the wavefunction does not vanish. It can be shown [58] that for reasonable forms of $v(\vec{r})$ this implies $v(\vec{r}) - v'(\vec{r}) = const$ everywhere, which contradicts the hypothesis: the two ground states $|\Psi_0\rangle$ and $|\Psi_0'\rangle$ must be distinct. Notice that the ground states of the two Hamiltonians can be degenerate, but that two sets of degenerate ground states cannot have a common element.

We can write

$$\begin{aligned} E_0^e &= \langle\Psi_0|\hat{\mathcal{H}}|\Psi_0\rangle < \langle\Psi_0'|\hat{\mathcal{H}}|\Psi_0'\rangle = \langle\Psi_0'|\hat{\mathcal{H}}'|\Psi_0'\rangle + \langle\Psi_0'|\hat{\mathcal{H}} - \hat{\mathcal{H}}'|\Psi_0'\rangle = E_0^{e'} + \langle\Psi_0'|\hat{\mathcal{V}} - \hat{\mathcal{V}}'|\Psi_0'\rangle \\ E_0^{e'} &= \langle\Psi_0'|\hat{\mathcal{H}}'|\Psi_0'\rangle < \langle\Psi_0|\hat{\mathcal{H}}'|\Psi_0\rangle = \langle\Psi_0|\hat{\mathcal{H}}|\Psi_0\rangle + \langle\Psi_0'|\hat{\mathcal{H}}' - \hat{\mathcal{H}}|\Psi_0\rangle = E_0^e + \langle\Psi_0|\hat{\mathcal{V}}' - \hat{\mathcal{V}}|\Psi_0\rangle \end{aligned} \tag{2.23}$$

and the two inequalities holds strictly since we know that $|\Psi_0\rangle$ and $|\Psi_0'\rangle$ cannot simultaneously be ground state for both Hamiltonians. Now, subtracting the two inequalities in eq. 2.23 and applying eq. 2.21 , we obtain

$$\begin{aligned} E_0^e - E_0^{e'} &< E_0^{e'} - E_0^e + \langle\Psi_0'|\hat{\mathcal{V}} - \hat{\mathcal{V}}'|\Psi_0'\rangle - \langle\Psi_0|\hat{\mathcal{V}}' - \hat{\mathcal{V}}|\Psi_0\rangle = \\ &= E_0^{e'} - E_0^e + \int d\vec{r}\,(v(\vec{r}) - v'(\vec{r}))\,n(\vec{r}) - \int d\vec{r}\,(v'(\vec{r}) - v(\vec{r}))\,n(\vec{r}) = \\ &= E_0^{e'} - E_0^e \end{aligned} \tag{2.24}$$

where we used the assumption that the two potentials correspond to the same ground state density $n(\vec{r})$, which leads to a contradiction.

The main accomplishment of the first statement of the theorem is that every functional dependence on v is shifted on n, thanks to the unique functional correspondence $v[n]$. This completely determines the Hamiltonian, that is $\hat{\mathcal{H}}[v] = \hat{\mathcal{H}}[v[n]]$. Similarly, once the Hamiltonian is fixed, the quantum mechanical problem can in principle be solved and every property traced back to n (even excited states). In particular, $|\Psi_0\rangle$ is a "natural" functional of the potential v and, by composition, must also be a functional of the ground state density. The ground state energy can be written as

$$\begin{aligned} E_0^e[v[n]] &= \langle\Psi_0[v[n]]|\hat{\mathcal{H}}[v[n]]|\Psi_0[v[n]]\rangle = \mathcal{F}[n] + \int d\vec{r} v[n](\vec{r}) n(\vec{r}) \\ \mathcal{F}[n] &= E_0^e[v[n]] - \int d\vec{r} v[n](\vec{r}) n(\vec{r}) \end{aligned} \tag{2.25}$$

where we isolated $\mathcal{F}[n]$, the Kohn-Sham functional. Some remarks:

- while $v[n]$ is a unique functional, $n[v]$ and $|\Psi_0[v[n]]\rangle$ are unique only if the ground state is non degenerate
- $E_0^e[v[n]]$ is unique, being the composition of two unique functionals.
- $\mathcal{F}[n]$ is unique and well defined as well (the arbitrary constant in $v(\vec{r})$ cancels out)
- in the non degenerate case, the functional $\mathcal{F}[n]$ can be defined as

  $$\langle\Psi_0[n]|\hat{\mathcal{T}} + \hat{\mathcal{W}}|\Psi_0[n]\rangle \tag{2.26}$$

  since all the mappings are unique. This corresponds to the definition given in eq. 2.25 which is, however, more general.

We can show that the variational principle holds with respect to the functional dependence on the ground state density. To prove it, the following functional, which linearly depends on the external potential, is introduced:

$$E_v[n] = \mathcal{F}[n] + \int d\vec{r} v(\vec{r}) n(\vec{r}) \tag{2.27}$$

where we treat v and n as two independent variables (i.e. the potential v is not necessarily $v_n = v[n]$). Manipulating this functional, we obtain

$$\begin{aligned} E_v[n] &= \mathcal{F}[n] + \int d\vec{r} v(\vec{r}) n(\vec{r}) = \\ &= \mathcal{F}[n] + \int d\vec{r} v_n(\vec{r}) n(\vec{r}) + \int d\vec{r} (v(\vec{r}) - v_n(\vec{r})) n(\vec{r}) = E_{v_n}[n] + \int d\vec{r} (v(\vec{r}) - v_n(\vec{r})) n(\vec{r}) = \\ &= \langle\Psi_0[v_n]|\hat{\mathcal{H}}[v_n]|\Psi_0[v_n]\rangle + \int d\vec{r} (v(\vec{r}) - v_n(\vec{r})) n(\vec{r}) = \\ &= \langle\Psi_0[v_n]|\hat{\mathcal{H}}[v_n]|\Psi_0[v_n]\rangle + \langle\Psi_0[v_n]|(\hat{\mathcal{V}} - \hat{\mathcal{V}}_n)|\Psi_0[v_n]\rangle = \\ &= \langle\Psi_0[v_n]|\hat{\mathcal{H}}[v]|\Psi_0[v_n]\rangle \end{aligned} \tag{2.28}$$

The true ground wavefunction for the Hamiltonian $\hat{\mathcal{H}}[v]$ is $\Psi_0[v] \equiv \Psi_0[v[n_0]]$, where n_0 is the ground state density obtained by solving the Schroedinger equation for $\hat{\mathcal{H}}[v]$. The standard variational

principle states that

$$E_v[n] = \langle \Psi_0[v_n]|\hat{\mathcal{H}}[v]|\Psi_0[v_n]\rangle \geq \langle \Psi_0[v[n_0]]|\hat{\mathcal{H}}[v]|\Psi_0[v[n_0]]\rangle = E_v[n_0] \tag{2.29}$$

i.e. the variational principle holds using the ground state density as the main independent variable; the equality is obtained if we plug into the expression exactly n_0.

2.2.2 The Kohn-Sham equations

While the HK theorem establishes the ground state electronic density as the main variable, it does not provide an explicit form for $E[n]$; in particular, the universal functional $\mathcal{F}[n]$, which is the non-trivial part of $E[n]$, is unknown. Moreover, $\mathcal{F}[n]$ is the same for any electronic system: a direct guess for such a complicated object is very unlikely. To make use of Density Functional Theory, practical implementations for these elements are needed: in the following paragraphs we will obtain equivalent expressions for the two functionals, which can (mostly) be evaluated in a simple manner.

We start [49, 57, 58] considering a non interacting system (i.e. $\mathcal{W} = 0$) with Hamiltonian

$$\hat{\mathcal{H}} = \hat{T} + \hat{V}_s \tag{2.30}$$

where $\hat{V}_s = \sum_i v_s(\vec{r}_i)$ is an external potential. If we assume non-degeneracy, the ground state wave-function $\Psi_s^0(\{\vec{r}_i\})$ is a Slater determinant made of orthonormal single particle orbitals $\psi_k(\vec{r}_i)$

$$\Psi_s^0(\mathbf{r}) = \frac{1}{\sqrt{N!}}\det\left[\psi_k(\vec{r}_i)\right] \tag{2.31}$$

and the individual orbitals can be obtained by resolving the following single-particle equations:

$$\left(-\frac{1}{2}\nabla^2 + v_s(\vec{r})\right)\psi_k(\vec{r}) = \varepsilon_k\psi_k(\vec{r}) \tag{2.32}$$

and then pick the N_e orbitals with the lowest energies ε_k to form $\Psi_s^0(\mathbf{r})$ The ground state density and the kinetic energy are respectively

$$\begin{aligned} n_s(\vec{r}) &= \sum_k^{\text{occ}} \psi_k^*(\vec{r})\psi_k(\vec{r}) \\ T_s &= -\frac{1}{2}\sum_{k\ \text{occ}} \int d\vec{r}\psi_k^*(\vec{r})\nabla^2\psi_k(\vec{r}) \end{aligned} \tag{2.33}$$

The demonstration in the previous section does not require any specific $\mathcal{W}$ (as long the Hamiltonian is bounded from below). If we apply our results to the non interacting system, we obtain

$$E_s[n] = \mathcal{T}_s[n] + \int d\vec{r}v_s[n](\vec{r})n(\vec{r}) \tag{2.34}$$

When there is no interaction $\mathcal{F}_s[n] = \mathcal{T}_s[n]$. The KS variational principle holds, and $E_{v_s}[n]$ will be minimum when $n_s(\vec{r})$ coincides with the first line of eq. 2.33.

The non interacting system just introduced will act as an effective system for the interacting problem we are effectively interested in. For that, we know that $E[n]$, given in eq. 2.27 will be a minimum when evaluated at $n_0(\vec{r})$, the interacting ground state density. We now assume that, given $n_0(\vec{r})$, we can build a non interacting system with an appropriate $v_s(\vec{r})$ such that $n_s(\vec{r}) = n_0(\vec{r})$. To do this, we write $E[n]$ as

$$E[n] = \mathcal{T}_s[n] + E_H[n] + E_{ext}[n] + E_{xc}[n] \tag{2.35}$$

where

$$E_H[n] = \frac{1}{2}\int d\vec{r}d\vec{r}' \frac{n(\vec{r})n(\vec{r}')}{|\vec{r}-\vec{r}'|} \tag{2.36}$$

$$E_{ext}[n] = \int d\vec{r} v_{ext}(\vec{r})n(\vec{r}) \tag{2.37}$$

$$E_{xc}[n] = \mathcal{F}[n] - \mathcal{T}_s[n] - E_H[n] \tag{2.38}$$

$E_H[n]$ is the Hartree term, accounting for the electron-electron interaction; $E_{ext}[n]$ is the energy functional coming from the external potential; finally, the definition of $E_{xc}[n]$ is a tautology. The first two functionals can be easily evaluated once the density is known. On the other hand, at this stage, we did not gain anything: the explicit form of $E_{xc}[n]$, which includes all the complicated many-body effects, is as unknown as the functional $\mathcal{F}[n]$. The hope is that this term should be small compared to the others for most systems, and that approximations could work reasonably well in this regime.

We now use the variational principle, imposing:

$$E[n_0 + \delta n] - E[n_0] = \mathcal{O}(\delta n^2) \tag{2.39}$$

Evaluating the single terms we have:

$$E_{ext}[n_0+\delta n] - E_{ext}[n_0] = \int d\vec{r} v_{ext}(\vec{r})\delta n(\vec{r}) + \mathcal{O}(\delta n^2) \tag{2.40}$$

$$E_H[n_0+\delta n] - E_H[n_0] = \int\int d\vec{r}d\vec{r}' \delta n(\vec{r}) \frac{1}{|\vec{r}-\vec{r}'|} n_0(\vec{r}') + \mathcal{O}(\delta n^2) \tag{2.41}$$

$$E_{xc}[n_0+\delta n] - E_{xc}[n_0] = \int d\vec{r} \frac{\delta E_{xc}[n]}{\delta n(\vec{r})}|_{n=n_0}\delta n(\vec{r}) + \mathcal{O}(\delta n^2) \tag{2.42}$$

$$\mathcal{T}_s[n_0+\delta n] - \mathcal{T}_s[n_0] = -\frac{1}{2}\sum_{k\ \mathrm{occ}}\int d\vec{r}\delta\psi_k^*(\vec{r})\nabla^2\psi_k(\vec{r}) + \delta\psi_k(\vec{r})\nabla^2\psi_k^*(\vec{r}) + \mathcal{O}(\delta\psi^2) \tag{2.43}$$

The last equation can be evaluated using eq. 2.32 and writing explicitly the variation δn:

$$\delta n(\vec{r}) = \sum_{k\ \mathrm{occ}} \delta\psi_k^*(\vec{r})\psi_k(\vec{r}) + \psi_k^*(\vec{r})\delta\psi_k(\vec{r}) + \mathcal{O}(\delta\psi^2) \tag{2.44}$$

$$\begin{aligned}\mathcal{T}_s[n_0+\delta n] - \mathcal{T}_s[n_0] &= \sum_{k\ \mathrm{occ}}\int d\vec{r}\left[\varepsilon_k - v_s(\vec{r})\right]\left(\delta\psi_k^*(\vec{r})\psi_k(\vec{r}) + \delta\psi_k(\vec{r})\psi_k^*(\vec{r})\right) + \mathcal{O}(\delta\psi^2) = \\ &= -\int d\vec{r} v_s(\vec{r})\delta n(\vec{r}) + \mathcal{O}(\delta n^2)\end{aligned} \tag{2.45}$$

In the last step, we used the orthonormalization of the wavefunction to get rid of the ε_k term: in fact

$$\int d\vec{r}\,(\delta\psi_k^*(\vec{r})\psi_k(\vec{r}) + \delta\psi_k(\vec{r})\psi_k^*(\vec{r})) = \delta \int d\vec{r}|\psi_k(\vec{r})|^2 = 0 \tag{2.46}$$

Putting all together and imposing eq. 2.39, we obtain

$$\int d\vec{r}\left\{v_s(\vec{r}) - \int d\vec{r}'\frac{1}{|\vec{r}-\vec{r}'|}n_0(\vec{r}') - v_{ext}(\vec{r}) - \frac{\delta E_{xc}[n]}{\delta n_0(\vec{r})}|_{n=n_0}\right\}\delta n(\vec{r}) = 0 \tag{2.47}$$

i.e.

$$v_s(\vec{r}) = v_H[n_0](\vec{r}) + v_{ext}(\vec{r}) + v_{xc}[n_0](\vec{r}) \tag{2.48}$$

$$v_H[n_0](\vec{r}) = \int d\vec{r}'\frac{1}{|\vec{r}-\vec{r}'|}n_0(\vec{r}') \tag{2.49}$$

$$v_{xc}[n_0](\vec{r}) = \frac{\delta E_{xc}[n]}{\delta n_0(\vec{r})}|_{n=n_0} \tag{2.50}$$

$$(-\frac{1}{2}\nabla^2 + \quad v_H[n_0](\vec{r}) \quad + v_{ext}(\vec{r}) + v_{xc}[n_0](\vec{r}))\psi_k(\vec{r}) = \varepsilon_k\psi_k(\vec{r}) \tag{2.51}$$

These are the Kohn-Sham equations [49]: they are non linear, since $v_H[n_0]$ and $v_{xc}[n_0]$ depend on the ground state density (and thus on the orbitals $\psi_k(\vec{r})$) and are usually solved by an iterative procedure starting from an initial guess for the orbitals. At this point we stress that as $E_{xc}[n]$ is unknown, so is $v_{xc}[n_0]$. Approximations can be built from physical intuition, but there is no systematic way to build and improve them: they are uncontrolled. There are different forms of $E_{xc}[n]$ that can be more suitable for a particular system, but most of the times this cannot be determined a priori: comparison with experiments or more rigorous theories (when available) is necessary.

2.2.3 Practical implementation

Due to computational limitations, relatively small cells (≈ 100 atoms in our case) are employed to simulate extended systems. Given a cell defined by three vectors $(\vec{L}_1, \vec{L}_2, \vec{L}_3)$, it is common practice to use periodic boundary conditions, periodically repeating the simulation cell. When dealing with crystal structures, the simulation cell is a supercell, containing several primitive cells. The translational symmetry of the system ensures that Bloch's theorem [59] holds, i.e. that KS orbitals can be written as

$$\psi_{\vec{k}}(\vec{r}) = e^{i\vec{k}\cdot\vec{r}}u_{\vec{k}}(\vec{r}) \quad , \quad u_{\vec{k}}(\vec{r}+\vec{L}_i) = u_{\vec{k}}(\vec{r}) \tag{2.52}$$

being decomposed in a periodic function modulated by the wave $e^{i\vec{k}\cdot\vec{r}}$. Introducing the reciprocal lattice vectors $\vec{G}_{\vec{m}}$, defined as

$$\vec{G}_{\vec{m}} = m_1\vec{B}_1 + m_2\vec{B}_2 + m_3\vec{B}_3 \quad , \quad \vec{m} = (m_1, m_2, m_3) \in \mathbb{N}^3 \tag{2.53}$$

$$\begin{aligned} \vec{B}_1 &= 2\pi \frac{\vec{L}_2 \times \vec{L}_3}{\vec{L}_1 \cdot (\vec{L}_2 \times \vec{L}_3)} \\ \vec{B}_2 &= 2\pi \frac{\vec{L}_3 \times \vec{L}_1}{\vec{L}_2 \cdot (\vec{L}_3 \times \vec{L}_1)} \\ \vec{B}_3 &= 2\pi \frac{\vec{L}_1 \times \vec{L}_2}{\vec{L}_3 \cdot (\vec{L}_1 \times \vec{L}_2)} \end{aligned} \tag{2.54}$$

the orbitals can be represented as

$$\psi_{\vec{k}}(\vec{r}) = e^{i\vec{k}\cdot\vec{r}} u_{\vec{k}}(\vec{r}) = e^{i\vec{k}\cdot\vec{r}} \sum_{\vec{m}} C_{\vec{k}\vec{m}} e^{i\vec{G}_m\cdot\vec{r}} \tag{2.55}$$

where the summation over integers is possible thanks to the periodicity of $u_k(\vec{r})$. Moreover, it is easy to verify that for any vector $\vec{G}_{\vec{m}}$ $\psi_{\vec{k}+\vec{G}_{\vec{m}}}(\vec{r}) = \psi_{\vec{k}}(\vec{r})$: the vector $\vec{k}$ can be confined to the primitive cell of the reciprocal lattice, conventionally the first Brillouin zone. This plane-wave expansion is used in many codes written to deal with periodic systems [60–62] and it is particularly convenient since Fourier transforms can be performed using efficient algorithms that scale as $N_{pw}\log(N_{pw})$ where N_{pw} is the number of coefficients C_{km} considered. When recast in the plane wave basis set, eq. 2.51 is

$$\sum_{\vec{m}'} \left[\frac{1}{2} \left| \vec{k} + \vec{G}_{\vec{m}} \right|^2 \delta_{\vec{m},\vec{m}'} + \tilde{v}_H(\vec{G}_{\vec{m}} - \vec{G}_{\vec{m}'}) + \tilde{v}_{ext}(\vec{G}_{\vec{m}} - \vec{G}_{\vec{m}'}) + \tilde{v}_{xc}(\vec{G}_{\vec{m}} - \vec{G}_{\vec{m}'}) \right] C^i_{km'} = \varepsilon^i_k C^i_{km} \tag{2.56}$$

with

$$\tilde{v}_l(\vec{G}) = \tfrac{1}{\Omega}\int_\Omega d\vec{r} v_l(\vec{r}) e^{i\vec{k}\cdot\vec{G}} \quad , \quad l = H, ext, xc \tag{2.57}$$

In fact, for every $\vec{k}$ we have a different Schroedinger equation: each equation has its own solutions, labelled by the i index, corresponding to a wavefunction $\psi^i_{\vec{k}}(\vec{r})$.

Since computer memory is finite, an inevitable approximation is truncating the sum in 2.55: a cutoff is usually defined as

$$\frac{1}{2}\left(\vec{G}_{\vec{m}} + \vec{k}\right)^2 \leq E_{cut} \tag{2.58}$$

The value of E_{cut} depends on the behaviour of the wavefunction in the proximity of one of the nuclei. In the sections regarding Quantum Monte Carlo it will be shown that the divergence of the Coulomb potential near the origin introduces a "cusp" in the wavefunction:

$$\frac{\partial \psi_k}{\partial r}|_{r=0} = -Z\psi^{00}_k \tag{2.59}$$

where ψ^{00} represents the spherical average of the wavefunction around the nucleus and r is the radial coordinate relative to its position. The cusp needs many terms in the planewave expansion to be accurately represented and, thus, a high value of E_{cut}. To circumvent the problem, pseudopotentials

are introduced [63]: a cut-off radius r_c is introduced and, within the sphere delimited by r_c, the full electron-nucleus Coulomb interaction is replaced by a smooth potential, generated to reproduce relevant properties of the "true" isolated atom. For heavier elements, another advantage of using pseudopotentials consists in eliminating core electrons, that are not relevant for chemical binding. Different strategies can be used: in our computations we either used a Coulomb potential when producing single particle orbitals for the Monte Carlo trial wavefunction (see following sections for details) or a PAW pseudopotential [64], which gives the most accurate results with a low value of E_{cut}.

With the introduction of the vector $\vec{k}$, many quantities (such as densities, energies) can be expressed as

$$\langle O \rangle = \frac{\Omega}{(2\pi)^3} \sum_{\text{i occ}} \int_{BZ} d\vec{k} O^i_{\vec{k}} \tag{2.60}$$

$$O^i_{\vec{k}} = \langle \psi^i_{\vec{k}} | O | \psi^i_{\vec{k}} \rangle \tag{2.61}$$

where $\int_{BZ}$ stands for an integral over the first Brillouin zone. Inevitably, integrals like this one must be reduced to sums to be evaluated computationally:

$$\langle O \rangle = \frac{1}{N_k} \sum_{k \in \text{BZ, i occ}} O^i_{\vec{k}} \tag{2.62}$$

with N_k being the number of $\vec{k}$ points sampled. A typical choice is to take a grid of vectors $\vec{k}$ defined as

$$\vec{k} = \frac{n_1 + \frac{1}{2}}{N_1} \vec{B}_1 + \frac{n_2 + \frac{1}{2}}{N_2} \vec{B}_2 + \frac{n_3 + \frac{1}{2}}{N_3} \vec{B}_3 \tag{2.63}$$

where n_i,N_i are integers and $-N_i/2 \leq n_i < N_i/2$, for a total of $N_1 \times N_2 \times N_3$ points. This is the so called Monkhorst-Pack mesh [65].

Finally, the crucial approximation: the choice of E_{xc}. In our calculations two different E_{xc} were employed: PBE [66], that is based on a parametrization of the homogeneous electron gas, and vdW-DF [67], that focuses on capturing the physics of systems where the van der Waals interaction is relevant. These choices will be justified in the appropriate sections.

2.3 Quantum Monte Carlo

As explained in the previous section, the practical implementation of DFT is plagued by the problem of approximating $E_{xc}[n]$. Nevertheless, it reduces the complexity of the many body quantum problem bypassing the evaluation of the electronic wavefunction. As mentioned at the beginning of this chapter, a discretization on a grid of the many body wavefunction is unfeasible; nevertheless, we will show how the wavefunction can be associated to a probability density that can be sampled using stochastic Monte Carlo methods. In this way there is no need to actually store the huge amount of information contained in the wavefunction and any physical observable can be computed as an average over that probability density. We will start describing the basics of Monte Carlo methods.

2.3.1 Monte Carlo methods and the Metropolis algorithm

In many applications, an important problem is how to efficiently compute quantities that can be written as

$$\langle O \rangle = \int d\mathbf{x} O(\mathbf{x}) p(\mathbf{x}) \tag{2.64}$$

where $p(\mathbf{x})$ is a correctly normalized probability density (i.e. $p(\mathbf{x}) \geq 0 \quad \forall \mathbf{x}$ and $\int d\mathbf{x} p(\mathbf{x}) = 1$) and $\mathbf{x}$ is a multidimensional array of continuous or discrete variables. When the number of dimensions of the $\mathbf{x}$-space grows, a discretization of the integral based on finite differences requires a mesh of exponential size; on the other hand, if we can sample configurations $\mathbf{x}_i$ according to $p(\mathbf{x})$, a good estimate of $\langle O \rangle$ is

$$\langle O \rangle \approx \bar{O} = \frac{1}{N_c} \sum_{i=1}^{N_c} O(\mathbf{x}_i) \tag{2.65}$$

A key feature of this approach is that the error associated to $\bar{O}$ is

$$\sigma_{\bar{O}} = \sqrt{\frac{\sigma^2_{O,p}}{N_c}} \tag{2.66}$$

$$\sigma^2_{O,p} = \frac{1}{N_c - 1} \sum_{i=1}^{N_c} \left(O(\mathbf{x}_i) - \bar{O} \right)^2 \tag{2.67}$$

$\sigma^2_{O,p}$ depends on the observable O and on the probability distribution $p(\mathbf{x})$ and it is a fixed feature of the process we are studying. This means that the error $\sigma_{\bar{O}} \propto \frac{1}{\sqrt{N_c}}$ irrespective of the dimensionality of $\mathbf{x}$; this is a huge advantage when dealing with high dimensional arrays. To compute $\bar{O}$ one must be able to efficiently sample $\mathbf{x}_i$ according to $p(\mathbf{x})$: this is accomplished using Markov chains [68].

A Markov chain is a stochastic process where configurations are generated in a sequence, and the probability of having a state $\mathbf{x}_i$ at step t_i depends only on the configuration at step t_{i-1}

$$P_C(\mathbf{x}_i, t_i | \mathbf{x}_{i-1}, t_{i-1}; \mathbf{x}_{i-2}, t_{i-2}; \ldots, \mathbf{x}_1, t_1) = P_C(\mathbf{x}_i, t_i | \mathbf{x}_{i-1}, t_{i-1}) \tag{2.68}$$

where $P_C(\mathbf{x}_i, t_i | \mathbf{x}_j, t_j)$ is the conditional probability of having $\mathbf{x}_i$ at step t_i given $\mathbf{x}_j$ at step t_j.

Given a target probability density $P_{target}(\mathbf{x}_i)$, the purpose of the Metropolis algorithm [69] is to build a Markov chain where configurations are asymptotically generated according to $P(\mathbf{x}_i)$, i.e.

$$\lim_{t_i \to \infty} P(\mathbf{x}_i, t_i) = P_{target}(\mathbf{x}_i) \tag{2.69}$$

We can think of each step of the Markov chain at time t_i as an operator π acting on the probability $P^{t_i} \equiv P(\mathbf{x}_i, t_i)$ [70]:

$$P^{(t+1)} = P^{(t)} \pi \tag{2.70}$$

We want a stationary state where $P^{(t+1)} = P^{(t)}$: for $i \to \infty$, we get

$$P_{target} = P_{target}\pi \tag{2.71}$$

i.e P_{target} must be an eigenvector of π with eigenvalue equal to 1. It can be proved [70] that all other eigenvectors have eigenvalues less than unity: thus, if the projection of the probability distribution at the first step $P^{(1)}$ on P_{target} is not zero, $P^{(1)}\pi^i$ will exponentially converge to the target distribution for large t_i. To determine π starting from P_{target}, it is easier to work with conditional probabilities, since we effectively generate one configuration starting from the previous one. In the Metropolis algorithm, they are written as

$$P_C(\mathbf{x}_A, t_i|\mathbf{x}_B, t_j) = T(\mathbf{x}_A|\mathbf{x}_B)\mathrm{A}(\mathbf{x}_A|\mathbf{x}_B) \tag{2.72}$$

This corresponds to a two-step process:

- given the state $\mathbf{x}_j$, a new configuration $\mathbf{x}'$ is proposed according to an a priori transition probability $T(\mathbf{x}'|\mathbf{x}_j)$
- a test is performed with probability of success $\mathrm{A}(\mathbf{x}_i|\mathbf{x}_j)$. If passed, $\mathbf{x}_i = \mathbf{x}'$; otherwise the move is rejected and the old configuration counted one more time.

Since $T(\mathbf{x}_i|\mathbf{x})$ must be a normalized probability, $\sum_i T(\mathbf{x}_i|\mathbf{x}) = 1$. We can rewrite eq. 2.70 using eq. 2.72:

$$\begin{aligned} P^{i+1}(\mathbf{x}_A) &= \sum_{\mathbf{x}_B} \big[T(\mathbf{x}_A|\mathbf{x}_B)\mathrm{A}(\mathbf{x}_A|\mathbf{x}_B)P^i(\mathbf{x}_B) \\ &+ T(\mathbf{x}_B|\mathbf{x}_A)\big(1 - \mathrm{A}(\mathbf{x}_B|\mathbf{x}_A)\big)P^i(\mathbf{x}_A)\big] \end{aligned} \tag{2.73}$$

i.e. the probability of being in $\mathbf{x}_A$ at step $i+1$ is the sum of the probabilities of accepting incoming moves from other configurations (first term) and of rejecting moves leaving the configuration (second term). For the target probability we have that

$$\begin{aligned} P_{target}(\mathbf{x}_A) &= \sum_{\mathbf{x}_B} \big[T(\mathbf{x}_A|\mathbf{x}_B)\mathrm{A}(\mathbf{x}_A|\mathbf{x}_B)P_{target}(\mathbf{x}_B) \\ &+ T(\mathbf{x}_B|\mathbf{x}_A)\big(1 - \mathrm{A}(\mathbf{x}_B|\mathbf{x}_A)\big)P_{target}(\mathbf{x}_A)\big] \end{aligned} \tag{2.74}$$

A sufficient (but not necessary) condition to satisfy eq. 2.74 is

$$P_C(\mathbf{x}_B|\mathbf{x}_A)P_{target}(\mathbf{x}_A) = P_C(\mathbf{x}_A|\mathbf{x}_B)P_{target}(\mathbf{x}_B) \tag{2.75}$$

also known as the detailed balance condition, or microscopic reversibility. For a system of N particles, a simple implementation of the Metropolis algorithm is the following:

- select at random one particle

- generate a random displacement vector $\boldsymbol{\Delta}$ whose components are uniformly distributed between $-\boldsymbol{\Delta}_{max}$ and $\boldsymbol{\Delta}_{max}$
- propose a new state where the position of the selected particle is moved by $\boldsymbol{\Delta}$

In this way, the a priori transition probability is symmetric: $T(\mathbf{x}_A|\mathbf{x}_B) = T(\mathbf{x}_B|\mathbf{x}_A)$. Eq. 2.75 becomes

$$\frac{\mathrm{A}(\mathbf{x}_B|\mathbf{x}_A)}{\mathrm{A}(\mathbf{x}_A|\mathbf{x}_B)} = \frac{P_{target}(\mathbf{x}_B)}{P_{target}(\mathbf{x}_A)} \tag{2.76}$$

A simple form of the acceptance probability $\mathrm{A}(\mathbf{x}_B|\mathbf{x}_A)$ that satisfies eq. 2.76 is $\mathrm{A}(\mathbf{x}_B|\mathbf{x}_A) = \min\left[1, \frac{P_{target}(\mathbf{x}_B)}{P_{target}(\mathbf{x}_A)}\right]$

2.3.2 Variational Monte Carlo

We now show how Born-Oppenheimer electronic energies can be written in a form satisfying eq. 2.64, using a method known as Variational Monte Carlo (VMC) [71–73]. Given a many body wavefunction $\Psi_T(\mathbf{r}_1, \ldots, \mathbf{r}_{N_e}; \{\mathbf{R}_\alpha\}) \equiv \Psi_T(\mathbf{r}; \mathbf{R})$ with $\int d\mathbf{r}|\Psi_T(\mathbf{r}; \mathbf{R})|^2 = 1$, the electronic energy in the Born-Oppenheimer approximation can be computed as

$$E_T(\mathbf{R}) = \langle \Psi_T(\mathbf{r}; \mathbf{R})|\hat{\mathcal{H}}|\Psi_T(\mathbf{r}; \mathbf{R})\rangle \tag{2.77}$$

In the position basis, eq. 2.77 can be rewritten as

$$E_T(\mathbf{R}) = \int d\mathbf{r}\Psi_T^*(\mathbf{r}; \mathbf{R})\hat{\mathcal{H}}(\mathbf{r}, \mathbf{R})\Psi_T(\mathbf{r}; \mathbf{R}) = \int d\mathbf{r}|\Psi_T(\mathbf{r}; \mathbf{R})|^2 E_L(\mathbf{r}; \mathbf{R}) \tag{2.78}$$

$$E_L(\mathbf{r}; \mathbf{R}) = \frac{\hat{\mathcal{H}}(\mathbf{r}, \mathbf{R})\Psi_T(\mathbf{r}; \mathbf{R})}{\Psi_T(\mathbf{r}; \mathbf{R})} \tag{2.79}$$

$|\Psi_T(\mathbf{r}; \mathbf{R})|^2 \geq 0$ in eq. 2.78 can be thought as a probability density and the integral as an average of the quantity $E_L(\mathbf{r}; \mathbf{R})$. Notice that if $\Psi_T(\mathbf{r}; \mathbf{R})$ is an eigenfunction of $\hat{\mathcal{H}}$, $E_L(\mathbf{r}; \mathbf{R}) = E_T(\mathbf{R})$ is constant over all the electronic configurational space. An interesting observable is

$$\sigma_T^2(\mathbf{R}) = \int d\mathbf{R}|\Psi_T(\mathbf{r}; \mathbf{R})|^2 \left(E_L(\mathbf{r}; \mathbf{R}) - E_T(\mathbf{R})^2\right) = \int d\mathbf{R}|\Psi_T(\mathbf{r}; \mathbf{R})|^2 E_L(\mathbf{r}; \mathbf{R})^2 - E_T(\mathbf{R})^2 \tag{2.80}$$

that quantifies the fluctuations of the integrand around the average value. Again, if $\Psi_T(\mathbf{r}; \mathbf{R})$ is an eigenfuction of $\hat{\mathcal{H}}$, $\sigma_T^2 = 0$.

In our search for the ground state, we recall the variational principle:

$$E_0(\mathbf{R}) \leq E_T(\mathbf{R}) \text{ for any } \Psi_T(\mathbf{r}; \mathbf{R}) \tag{2.81}$$

and the equality holds if $\Psi_T(\mathbf{r}; \mathbf{R})$ is the ground state wavefunction. $\Psi_T(\mathbf{r}; \mathbf{R})$ must satisfy some conditions:

- $\Psi_T(\mathbf{r}; \mathbf{R})$ and $\nabla\Psi_T(\mathbf{r}; \mathbf{R})$ must be continuous when the potential is finite
- $\int d\mathbf{r}|\Psi_T(\mathbf{r}; \mathbf{R})|^2$ and $E_T(\mathbf{R}) = \langle \Psi_T(\mathbf{r}; \mathbf{R})|\hat{\mathcal{H}}|\Psi_T(\mathbf{r}; \mathbf{R})\rangle$ must be finite

- $\int d\mathbf{R}|\Psi_T(\mathbf{r};\mathbf{R})|^2 E_L(\mathbf{r};\mathbf{R})^2$ must be finite as well, if we want a well defined σ_T^2

The practical problem is now evaluating $E_T(\mathbf{R})$. This is achieved by employing the Monte Carlo methods described in the previous section: $E_T(\mathbf{R})$ can be evaluated averaging $E_L(\mathbf{r};\mathbf{R})$ over a $3N_e$ dimensional space. We must sample N_c configurations $\mathbf{r}_i$ according to the probability density $|\Psi_T(\mathbf{r};\mathbf{R})|^2$ and then evaluate

$$E_T(\mathbf{R}) \approx \frac{1}{N_c}\sum_{i=1}^{N_c} E_L(\mathbf{r}_i;\mathbf{R}) \tag{2.82}$$

The configurations $\mathbf{r}_i$ are generated through the Metropolis Monte Carlo algorithm by building the corresponding Markov chain.

2.3.3 Our trial wavefunction

The key ingredient of the VMC calculation is the choice of the many-body trial wave function. The simplest antisymmetric wavefunction for a fermionic system with $N^\uparrow$ spin-up and $N^\downarrow$ spin-down electrons is a product of two Slater determinants of single electron orbitals:

$$\Psi_T(\vec{r}|\mathbf{R}) = S^\uparrow[\theta_k(\vec{r}_i|\mathbf{R})]S^\downarrow[\theta_k(\vec{r}_i|\mathbf{R})] \tag{2.83}$$

where

$$S^s[\theta_k(\vec{r}_i|\mathbf{R})] = \frac{1}{\sqrt{N^s!}}\det\begin{pmatrix} \theta_1(\vec{r}_1|\mathbf{R}) & \theta_1(\vec{r}_2|\mathbf{R}) & \cdots & \theta_1(\vec{r}_{N^s}|\mathbf{R}) \\ \theta_2(\vec{r}_1|\mathbf{R}) & \cdots & \cdots & \theta_2(\vec{r}_{N^s}|\mathbf{R}) \\ \vdots & \vdots & \ddots & \vdots \\ \theta_{N^s}(\vec{r}_1|\mathbf{R}) & \theta_{N^s}(\vec{r}_2|\mathbf{R}) & \cdots & \theta_{N^s}(\vec{r}_{N^s}|\mathbf{R}) \end{pmatrix} \quad s=\uparrow,\downarrow \tag{2.84}$$

For non-magnetic systems, $N^\uparrow = N^\downarrow$. The wavefunction in eq. 2.83 can account for exchange effects, which keep like-spin electrons away from each other. Nevertheless, it can be an eigenfunction of a system of non interacting electrons only, where Coulomb repulsion is neglected. Moreover, there are some analytical constraints that a many-body wavefunction must satisfy that are not reproduced by single Slater determinants.

2.3.3.1 The Kato cusp conditions

One of such constraints is the so called Kato cusp condition [73–75]. This condition arises from the divergence in the Coulomb potential when the distance between two electrons becomes very small. If we explicitly consider electrons $\vec{r}_i$ and $\vec{r}_j$ and rewrite the Hamiltonian using the variables $\vec{r} = \vec{r}_i - \vec{r}_j$ and $\vec{r}_{cm} = \frac{1}{2}(\vec{r}_i + \vec{r}_j)$, we obtain:

$$\hat{\mathcal{H}} = -\nabla^2_{\vec{r}} + \frac{1}{r} - \frac{1}{4}\nabla^2_{\vec{r}_{cm}} - \frac{1}{2}\sum_{k\neq i,j}\nabla^2_{\vec{r}_k} + V(\vec{r}_1,\ldots,\vec{r}_N) - \frac{1}{r} \tag{2.85}$$

where the first two terms are potentially divergent when $\vec{r} \to 0$ and the last term cancels the divergence present in the many body potential. If we fix the remaining electronic coordinates and expand the wavefunction in spherical harmonics, we obtain

$$\Psi(\vec{r}) \equiv \psi(\vec{r}; \vec{r}_1, \ldots, \vec{r}_{cm}, \ldots, \vec{r}_N) = \sum_l \sum_{m=-l}^{l} r^l f_{lm}(r) Y_{lm}(\theta, \phi) \tag{2.86}$$

where r,θ and ϕ are the spherical polar coordinates of $\vec{r}$, Y_{lm} the spherical harmonics and $f_{lm}(r)$ the coefficients of the expansion. The spin dependence is buried in these coefficients: if the two spins are parallel, the spatial part of the wavefunction must be odd in $\vec{r}$ and only $f_{lm}(r)$ coefficients with odd l survive; if the spins are antiparallel, the opposite is true and we only have non zero $f_{lm}(r)$ coefficients when l is even. The contribution to the local energy coming from the first two terms in eq. 2.85 for antiparallel and parallel spins for small $\vec{r}$ is

$$\begin{aligned} E_L^a &= -\frac{\nabla^2 \Psi(\vec{r})}{\Psi(\vec{r})} + \frac{1}{\vec{r}} = -\frac{\nabla^2 f_{00}(r)}{f_{00}(r)} + \mathcal{O}(r^0) + \frac{1}{r} = -\frac{\nabla^2 f_{00}(r)}{f_{00}(r)} + \mathcal{O}(r^0) + \frac{1}{r} = \\ &= -\frac{2}{r f_{00}(0)} \frac{\partial f_{00}}{\partial r}|_{r=0} + \mathcal{O}(r^0) + \frac{1}{r} \end{aligned} \tag{2.87}$$

$$\begin{aligned} E_L^s &= -\frac{\nabla^2 \Psi(\vec{r})}{\Psi(\vec{r})} + \frac{1}{\vec{r}} = -\frac{\nabla^2 \left[r \sum_{m=-1}^{1} f_{1m}(r) Y_{1m}(\theta, \phi) \right]}{r \sum_{m=-1}^{1} f_{1m}(r) Y_{1m}(\theta, \phi)} + \mathcal{O}(r^0) + \frac{1}{r} = \\ &= -4 \frac{\left[\sum_{m=-1}^{1} \frac{\partial f_{1m}}{\partial r}|_{r=0} Y_{1m}(\theta, \phi) \right]}{r \sum_{m=-1}^{1} f_{1m}(0) Y_{1m}(\theta, \phi)} + \mathcal{O}(r^0) + \frac{1}{r} \end{aligned} \tag{2.88}$$

where only divergent terms of the expansions are retained, while the regular behaving terms are absorbed in the $\mathcal{O}(r^0)$ term. If the wavefunction is an Hamiltonian eigenfunction, the local energy is a constant everywhere and the divergent terms in eq. 2.87 and 2.88 must cancel each other for every value of θ and ϕ, i.e.

$$\left. \frac{\partial f_{00}}{\partial r} \right|_{r=0} = \frac{f_{00}(0)}{2} \tag{2.89}$$

$$\left. \frac{\partial f_{1m}}{\partial r} \right|_{r=0} = \frac{f_{1m}(0)}{4} \tag{2.90}$$

Since there is no explicit correlation, Slater determinants of single particle orbitals cannot depend on interelectronic coordinates, and cannot enforce the conditions described in eq. 2.89 and 2.90.

An analogous cusp condition must be satisfied when electrons are in the proximity of a nucleus. With similar arguments, one can prove that an electron-nucleus cusp condition exists:

$$\left. \frac{\partial \Psi_{00}}{\partial r_i} \right|_{r_i=0} = -Z \Psi_{00} \tag{2.91}$$

where r_i is the distance of the i-th electron from a nucleus with charge Z and Ψ_{00} is the spherical average of the wavefunction around the nucleus. This condition can either be satisfied by the Slater determinant (if and only if each individual orbital satisfies the cusp condition) or implemented by modifying the wavefunction.

A popular form for the trial wavefunction is

$$\Psi_T(\mathbf{r}|\mathbf{R}) = e^{J(\mathbf{r}|\mathbf{R})} S^{\uparrow}[\theta_k(\vec{r}_i|\mathbf{R})] S^{\downarrow}[\theta_k(\vec{r}_i|\mathbf{R})] \tag{2.92}$$

where $J(\mathbf{r}|\mathbf{R})$ is the so called Jastrow factor [76]. Since the antisymmetric character of the wavefunction is built into the Slater determinant, the Jastrow factor must be symmetric under particle permutation. For the Jastrow-Slater wavefunction, eq. 2.89, 2.90 and 2.91 become

$$\left.\frac{\partial J}{\partial r}\right|_{r=0} = \frac{1}{2} \quad \text{antiparallel spins} \tag{2.93}$$

$$\left.\frac{\partial J}{\partial r}\right|_{r=0} = \frac{1}{4} \quad \text{parallel spins} \tag{2.94}$$

$$\left.\frac{\partial J}{\partial r}\right|_{r=0} = -Z \quad \text{nuclei} \tag{2.95}$$

The last equality is valid if we assume that the Slater determinant is smooth with respect to electronic coordinates relative to nuclei (this is the case if, for example, a non divergent pseudopotential is used to compute the single orbitals). If, on the other hand, every electronic orbital satisfies the nuclear cusp condition, the determinant satisfies the same condition as well and the Jastrow factor must be cuspless (i.e. $Z = 0$). In our case, the Jastrow factor is written as

$$J(\mathbf{r}|\mathbf{R}) = -\sum_{i=1}^{N_e} \left[\frac{1}{2} \sum_{j \neq i}^{N_e} u_{ee}(r_{ij}) - \sum_{\alpha=1}^{N_p} u_{ep}(|\vec{r}_i - \vec{R}_\alpha|) \right] \tag{2.96}$$

where $r_{ij} = |\vec{r}_i - \vec{r}_j|$, satisfying the symmetric constraint required by the global fermionic wavefunction. An important indication on the form of the u_{ee} and u_{ep} comes from the Random Phase Approximation [77]. In this approximation the Hamiltonian of the system is reduced to a sum of a short-range interactions among electrons and a long range part described by collective oscillations (plasmons). Since RPA becomes formally exact when the electron density goes to infinity, results obtained in this approximation can be useful for our high-density regime. In particular, it can be proved [77, 78] that minimizing the energy in RPA leads to

$$\begin{aligned} u_{ee}^{RPA}(k) &= -\frac{1}{2} + \sqrt{1 + a_k} \\ u_{ep}^{RPA}(k) &= -\frac{a_k}{\sqrt{1 + a_k}} \end{aligned} \tag{2.97}$$

where $u_{ee}(k)$ and $u_{ep}(k)$ are the Fourier transforms of $u_{ee}(r)$ and $u_{ep}(r)$, and $a_k = 12 r_s / k^4$, with $r_s = \left(\frac{3v}{4\pi}\right)^{(1/3)}$. The RPA forms satisfy the cusp conditions, providing the expected analytic limits both for $r \to 0$ and $r \to \infty$: still, the RPA does not provide the exact solution for intermediate values of r. Following ref. [79], we use:

$$\tilde{u}_\alpha(r) = u_\alpha^{RPA}(r) + \lambda_{2b}^\alpha \, e^{-(r/w_{2b}^\alpha)^2} \qquad \alpha = (ee, ep) \tag{2.98}$$

adding a remaining empirical part to $u_\alpha^{RPA}(r)$, which is a simple Gaussian preserving both short and long range behavior from RPA and introducing the free variational parameters λ_{2b}^α and w_{2b}^α.

2.3.3.2 Backflow transformation

The inclusion of the Jastrow factor provides a fraction of the electronic correlation missing in a simple Slater determinant. However, the form of the wavefunction can still be improved. A formal expression of the exact ground state wavefunction in terms of a trial wavefunction is the Feynman-Kac formula [55]:

$$\Psi_0(\mathbf{r}|\mathbf{R}) = \frac{\Psi_T(\mathbf{r}|\mathbf{R})}{\langle\Psi_T|\Psi_0\rangle}\langle\exp\left(-\int_0^\infty dt\,(E_L(\mathbf{r}_t) - E_0(\mathbf{R}))\right)\rangle_{\psi_T^2} \tag{2.99}$$

where $\Psi_0(\mathbf{r}|\mathbf{R})$ is the exact many-body wavefunction; $\Psi_T(\mathbf{r}|\mathbf{R})$ is the (real, non negative) trial wavefunction; E_0 is the exact ground energy; $\langle\dots\rangle_{\Psi_T^2}$ stands for an average over different trajectories all starting from $\mathbf{r}$ and evolving for a time t according to

$$\frac{d\mathbf{r}_t}{dt} = \eta(t) - \nabla\ln\psi_T(\mathbf{r}_t|R) \tag{2.100}$$

$\eta(t)$ is a Weiner process [68], i.e. the electrons perform a Brownian motion, being at the same time under the effect of the drift $-\nabla\ln\psi_T(\mathbf{r}_t|R)$. The above expression can be approximated [80]: if the trial wavefunction is good enough, the exponent will be small and the cumulant approximation can be invoked, i.e.

$$\begin{aligned}\Psi_0(\mathbf{r}|\mathbf{R}) \propto \Psi_T(\mathbf{r}|\mathbf{R})\langle\exp\big(-\int_0^\infty dt(E_L(\mathbf{r}_t) - E_0(\mathbf{R}))\big)\rangle_{\Psi_T^2} \approx \\ \approx \Psi_T(\mathbf{r}|\mathbf{R})\exp\left(-\langle\bar{E} - E_0(\mathbf{R})\rangle_{\Psi_T^2} + \frac{1}{2}\langle\delta\bar{E}^2\rangle_{\Psi_T^2}\right)\end{aligned} \tag{2.101}$$

where $\bar{E} = \int_0^\infty dt E_L(\mathbf{r}_t)$. If the expansion is truncated at the first term and some simplifying ansatzs are assumed, one finds that the electronic coordinates in the Slater determinant part of the wavefunction are replaced by the backflow coordinates $\mathbf{x}_i$,

$$\vec{x}_i = \vec{r}_i + \sum_{j\neq i}^{N_e}\left[\tilde{y}_{ee}^{RPA}(r_{ij})\right](\vec{r}_i - \vec{r}_j) + \sum_{\alpha=1}^{N_p}\left[\tilde{y}_{ep}^{RPA}(|\vec{r}_i - \vec{R}_\alpha|)\right](\vec{r}_i - \vec{R}_\alpha) \tag{2.102}$$

where the analytical form of $\tilde{y}_{ee}$ and $\tilde{y}_{ep}$ can be found in ref. [80]. Empirical variational parameters can be added on top of these analytical expressions to make the trial wavefunction more flexible. Gaussians were first introduced by Kwon et al. [81] for the homogeneous electron gas; they were later used for high-pressure hydrogen [82], improving both the variational energy and the associated variance. The $\tilde{y}_{ee}^{RPA}$ and $\tilde{y}_{ep}^{RPA}$ are replaced by

$$\begin{aligned}\tilde{y}_\alpha &= y_\alpha^{RPA}(r_\alpha) + \eta_{ep}(r_\alpha) \\ \eta_\alpha(r) &= \lambda_b^\alpha\, e^{-((r-r_b^\alpha)/w_b^\alpha)^2} \qquad\qquad \alpha = (ee, ep)\end{aligned} \tag{2.103}$$

with free variational parameters $\lambda_b^\alpha, r_b^\alpha$ and w_b^α.

The final explicit form of the trial wave function is

$$\Psi_T(\mathbf{r}|\mathbf{R}) = S^\uparrow[\theta_k(\vec{x}_i|\mathbf{R})]S^\downarrow[\theta_k(\vec{x}_i|\mathbf{R})]\exp\left(-\sum_{i=1}^{N_e}\left[\frac{1}{2}\sum_{j\neq i}^{N_e}\tilde{u}_{ee}(r_{ij}) - \sum_{\alpha=1}^{N_p}\tilde{u}_{ep}(|\vec{r}_i - \vec{R}_\alpha|)\right]\right) \tag{2.104}$$

2.3.4 Twist averaged boundary conditions

As for Density Functional theory, the evaluation of the Ab Initio electronic energy is rather demanding: the computational time needed for the evaluation of a trial wavefunction with embedded backflow terms scales as N_e^{3-4} [83]: this limits the size of the studied systems (up to 96 electrons, in our case). Periodic boundary conditions are enforced: given a supercell defined by three cell vectors $\vec{L}_1$, $\vec{L}_2$, $\vec{L}_3$, the original set of particles is replicated periodically along the three cell vectors. In this way, the potential energy displays the following symmetry:

$$V(\vec{r}_1, \ldots, \vec{r}_i + L_m, \ldots, \vec{r}_N) = V(\vec{r}_1, \ldots, \vec{r}_i, \ldots, \vec{r}_{N_e}) \tag{2.105}$$

for any particle i ($m = 1, 2, 3$). From this property, one can derive a many-body generalization of the Bloch's theorem [84]: a many-body eigenfunction $\Psi(\vec{r}_1, \ldots, \vec{r}_{N_e})$ of an Hamiltonian retaining the translational symmetry of eq. 2.105 satisfies the condition

$$\Psi_{\vec{k}}(\vec{r}_1, \ldots, \vec{r}_i + \vec{L}_m, \ldots, \vec{r}_{N_e}) = \Psi_{\vec{k}}(\vec{r}_1, \ldots, \vec{r}_i, \ldots, \vec{r}_{N_e}) e^{i\vec{k}\cdot\vec{L}_m} \tag{2.106}$$

and the momentum $\vec{k}$ can be used to classify the wavefunction $\Psi_{\vec{k}}$, which "gains" a twist $\theta = \vec{k} \cdot \vec{L}_m$ when a particle is translated out of the simulation box. It can be showed [85, 86] that physical observables are periodic in θ (i.e. $A(\theta) = A(\theta + 2\pi)$, limiting the relevant interval to $-\pi \leq \theta < \pi$, in a manner equivalent to limiting $\vec{k}$ to the Brillouin zone. One can set $\vec{k} = 0$, choosing a wavefunction that is fully periodic across the replica of the supercell. However, this procedure leads to an enhancement of finite size errors, which is well exemplified by the non-interacting homogeneous electron gas in a cubic box of side L [86]. This is a standard textbook example solved with fully periodic boundary conditions: in this case, the eigenfunctions are plane waves with momentum $\vec{p} = \frac{2\pi\vec{n}}{L}$ ($\vec{n}$ being a 3 dimensional vector of integers). If the number of electrons N_e is of the order of the Avogadro's number, the region covered by the filled quantum p states is an excellent approximation of the Fermi sphere, which is the expected result in the thermodynamic limit. On the other hand, if we only have tens or hundreds of electrons, the occupied volume is a poor approximation of expected result. This is a serious issue, especially for metals, where discontinuous jumps in the occupation number near the Fermi surface can drastically alter the properties of the system. A way to solve this problem is to choose to work with twist-averaged boundary conditions (TABC) [86] and compute

$$\langle O \rangle_{TABC} = \frac{\Omega}{(2\pi)^3} \int_{BZ} d\vec{k} \, \langle \Psi_{\vec{k}} | \hat{\mathcal{O}} | \Psi_{\vec{k}} \rangle \tag{2.107}$$

where $\langle \ldots \rangle$ is the standard scalar product in the $3N_e$ dimensional space of the electronic coordinates. This is an average over the different twists: in our simple example we get different momenta $\vec{p}_{\vec{k}} = \frac{2\pi\vec{n}}{L} + \vec{k}$ that can form a much finer grid, resulting in a better approximation of the Fermi sphere. A better convergence to the thermodynamic limit using TABC rather that PBC was demonstrated in ref. [87] for the electron gas with different trial wavefunctions.

2.4 Path integrals

In the previous two sections the Ab Initio computation of the Born-Oppenheimer electronic energy was addressed. However, we want to compute thermodynamic averages at finite temperature, including nuclear quantum effects. As stated at the beginning of this chapter, under the assumption of the Born-Oppenheimer approximation, macroscopic quantities of a system in the canonical ensemble can be computed as

$$\begin{aligned} \langle O \rangle &= \frac{1}{Z} \int d\mathbf{R} d\mathbf{R}' \, \langle \mathbf{R}' | \, \hat{O} \, | \mathbf{R} \rangle \, \rho(\mathbf{R}, \mathbf{R}'; \beta) \\ Z &= \int d\mathbf{R} \rho(\mathbf{R}, \mathbf{R}; \beta) \\ \rho(\mathbf{R}, \mathbf{R}'; \beta) &= \langle \mathbf{R} | \, e^{-\beta(\hat{\mathcal{K}}_p + \hat{E}_0^e(\mathbf{R}))} \, | \mathbf{R}' \rangle \end{aligned} \tag{2.108}$$

where $E_0^e(\mathbf{R})$ may be computed using VMC or any other Ab Initio method. In the path integral approach [55, 88] the propagator $e^{-\beta(\hat{\mathcal{K}}_p + \hat{E}_0^e)}$ is broken into P parts:

$$e^{-\beta(\hat{\mathcal{K}}_p + \hat{E}_0^e)} = \left(e^{-\tau(\hat{\mathcal{K}}_p + \hat{E}_0^e)} \right)^P, \quad \tau = \beta / P \tag{2.109}$$

$$\rho(\mathbf{R}, \mathbf{R}'; \beta) = \int d\mathbf{R}_1 ... d\mathbf{R}_{P-1} \rho(\mathbf{R}, \mathbf{R}_1; \tau) ... \rho(\mathbf{R}_{P-1}, \mathbf{R}'; \tau) \tag{2.110}$$

In the above expression we have assumed that the identity operator could be written as $I = \int d\mathbf{R} \, |\mathbf{R}\rangle \, \langle \mathbf{R}|$, ignoring the quantum effects of the Fermi-Dirac distribution on the protons, which are treated as distinguishable particles. For bosonic/fermionic systems the basis is the subset $|\mathbf{R}\rangle_\pm$, with

$$|\mathbf{R}\rangle_\pm = \frac{1}{\sqrt{N!}} \sum_{\mathcal{P}} (\pm)^{\mathcal{P}} \mathcal{P} \, |\mathbf{R}\rangle \tag{2.111}$$

and $\mathcal{P}$ being a permutation of the particle indices of $\mathbf{R}$. In the present treatment, we assume that the only relevant permutation is the identity. By introducing the action

$$S(\mathbf{R}, \mathbf{R}'; \tau) = -\ln(\rho(\mathbf{R}, \mathbf{R}'; \tau)) \tag{2.112}$$

the mean value of O can be expressed as

$$\langle O \rangle = \frac{1}{Z} \int d\mathbf{R}_0 \dots d\mathbf{R}_P \, \langle \mathbf{R}_0 | \, \hat{O} \, | \mathbf{R}_P \rangle \, e^{-\sum_{p=0}^{P-1} S(\mathbf{R}_p, \mathbf{R}_{p+1}; \tau)} \tag{2.113}$$

$$Z = \int d\mathbf{R}_0 \dots d\mathbf{R}_{P-1} e^{-\sum_{p=0}^{P-1} S(\mathbf{R}_p, \mathbf{R}_{p+1}; \tau)}, \quad \mathbf{R}_P = \mathbf{R}_0 \tag{2.114}$$

If $\hat{O} \equiv O(\hat{\mathbf{R}})$, this average can be evaluated with a Monte Carlo procedure by sampling the positive function $\Pi(\mathbf{R}_0, \dots, \mathbf{R}_{P-1}) = \frac{1}{Z} e^{-\sum_{p=0}^{P-1} S(\mathbf{R}_p, \mathbf{R}_{p+1}; \tau)}$ in a $3N_pP$ dimensional configuration space with the condition $\mathbf{R}_0 = \mathbf{R}_P$. The above expression is exact, no matter what the value of P is; in practical applications, however, $S(\mathbf{R}, \mathbf{R}'; \tau)$ must be approximated and the choice of P depends on the goodness of this approximation. Following ref. [88], we now define two (arbitrary) parts of the

action, the kinetic action A_K and the interpotential action A_U:

$$A_K(\mathbf{R},\mathbf{R}',\tau) = \frac{3N_p}{2}\ln\left(2\pi\tau/M_p\right) + \frac{M_p(\mathbf{R}-\mathbf{R}')^2}{2\tau} \quad (2.115)$$

$$A_U(\mathbf{R},\mathbf{R}',\tau) = S(\mathbf{R},\mathbf{R}';\tau) - A_K(\mathbf{R},\mathbf{R}',\tau) \quad (2.116)$$

Why it is convenient to split the action in this way and why these names are used for these two quantities will be explained in the next section, when the primitive approximation is introduced.

2.4.1 The primitive approximation

A simple choice to compute the action is the so called primitive approximation [88]:

$$\begin{aligned}\rho(\mathbf{R},\mathbf{R}';\tau) &= \langle\mathbf{R}|\, e^{-\frac{\tau}{2}\hat{E}_0^e} e^{-\tau\hat{\mathcal{K}}_p} e^{-\frac{\tau}{2}\hat{E}_0^e)}\, |\mathbf{R}'\rangle + \mathcal{O}(\tau^2) = \\ &= e^{-\frac{\tau}{2}E_0^e(\mathbf{R})}\, \langle\mathbf{R}|\, e^{-\tau\hat{\mathcal{K}}_p}\, |\mathbf{R}'\rangle\, e^{-\frac{\tau}{2}E_0^e(\mathbf{R}')} + \mathcal{O}(\tau^2)\end{aligned} \quad (2.117)$$

The matrix element involving the kinetic energy $\mathcal{K}_p$ in eq. 2.117 can be evaluated with a resolution of the identity [1]

$$\begin{aligned}\langle\mathbf{R}|\, e^{-\tau\hat{\mathcal{K}}_p}\, |\mathbf{R}'\rangle &= \int d\mathbf{P}\, \langle\mathbf{R}|\, e^{-\tau\hat{\mathcal{K}}_p}\, |\mathbf{P}\rangle\, \langle\mathbf{P}|\mathbf{R}'\rangle = \\ &= \frac{1}{(2\pi)^{3N_p}} \int d\mathbf{P} e^{-\frac{\tau}{2M_p}\mathbf{P}^2} e^{i\mathbf{P}\cdot(\mathbf{R}'-\mathbf{R})} = \left(\frac{M_p}{2\pi\tau}\right)^{\frac{3N_p}{2}} e^{-\frac{M_p}{2\tau}(\mathbf{R}-\mathbf{R}')^2}\end{aligned} \quad (2.118)$$

It is now clear that in the primitive approximation $S(\mathbf{R},\mathbf{R}',\tau) = A_K(\mathbf{R},\mathbf{R}',\tau) + \frac{\tau}{2}(E_0^e(\mathbf{R}) + E_0^e(\mathbf{R}'))$: the kinetic action is indeed the contribution of the kinetic operator and the interpotential action $A_U = \frac{\tau}{2}(V(\mathbf{R}) + V(\mathbf{R}'))$ stems entirely from the potential energy. While it is appealing to rigidly separate the two contributions, this is valid only within the primitive approximation: the exact A_U contains kinetic terms of higher order in τ.

The density matrix can thus be approximated as

$$\begin{aligned}\rho(\mathbf{R}_0,\mathbf{R}_P;\beta) &= \int d\mathbf{R}_0 \ldots d\mathbf{R}_{P-1} e^{-\sum_{p=0}^{P-1}(A_K(\mathbf{R}_p,\mathbf{R}_{p+1};\tau)+A_U(\mathbf{R}_p,\mathbf{R}_{p+1};\tau))} \approx \\ &\approx \left(\frac{M_p}{2\pi\tau}\right)^{\frac{3PN_p}{2}} \int d\mathbf{R}_0 \ldots d\mathbf{R}_{P-1} e^{-\sum_{p=0}^{P-1}\left(\frac{M_p}{2\tau}(\mathbf{R}_p-\mathbf{R}_{p+1})^2 - \tau E_0^e(\mathbf{R}_p)\right)}\end{aligned} \quad (2.119)$$

At this point, the partition function in the primitive approximation Z_{pa} can be written as

$$\begin{aligned}Z_{pa} &= \int d\mathbf{R}_0 \rho(\mathbf{R}_0,\mathbf{R}_0;\beta) \approx \\ &\approx \left(\frac{M_p}{2\pi\tau}\right)^{\frac{3PN_p}{2}} \int d\mathbf{R}_0 \ldots d\mathbf{R}_{P-1} e^{-\sum_{p=0}^{P-1}\left(\frac{M_p}{2\tau}(\mathbf{R}_p-\mathbf{R}_{p+1})^2 - \tau E_0^e(\mathbf{R}_p)\right)}, \quad \mathbf{R}_P = \mathbf{R}_0\end{aligned} \quad (2.120)$$

Eq. 2.120 can be interpreted as the partition function of a system made of $P \times N_p$ "beads", organized in N_p closed polymers: every bead interacts with the two neighbours (in imaginary time) of the same polymer through an harmonic term $(\mathbf{R}_p - \mathbf{R}_{p+1})^2$. Moreover, it interacts with beads of other

[1] This expression is rigorously valid for an infinite system but becomes very accurate when $L >> \sqrt{\tau/M_p}$, L being the length of the box

polymers that have the same index (same imaginary time) through the Born-Oppenheimer energy surface $E_0^e(\mathbf{R}_p)$. This expression establishes an isomorphism between a quantum system with N_p particles and a classical system of N_p polymers with harmonic beads. Operators that are diagonal in the position representation (such as the potential energy $E_0^e(\mathbf{R})$) can be evaluated as

$$\begin{aligned}
\langle V \rangle &= \frac{1}{Z}\int d\mathbf{R}_0 \dots d\mathbf{R}_P E_0^e(\mathbf{R}_0)\delta_{\mathbf{R}_0,\mathbf{R}_P} e^{-\sum_{p=0}^{P-1}\left(\frac{M_p}{2\tau}(\mathbf{R}_p-\mathbf{R}_{p+1})^2-\tau E_0^e(\mathbf{R}_p)\right)} \\
&= \frac{1}{Z}\int d\mathbf{R}_0 \dots d\mathbf{R}_{P-1}\left(\frac{1}{P}\sum_{p=0}^{P-1} E_0^e(\mathbf{R}_p)\right) e^{-\sum_{p=0}^{P-1}\left(\frac{M_p}{2\tau}(\mathbf{R}_p-\mathbf{R}_{p+1})^2-\tau E_0^e(\mathbf{R}_p)\right)} \\
&= \langle\left(\frac{1}{P}\sum_{p=0}^{P-1} E_0^e(\mathbf{R}_p)\right)\rangle_{\mathcal{P}_{poly}} \qquad (2.121) \\
\mathcal{P}_{poly} &= \frac{1}{Z} e^{-\sum_{p=0}^{P-1}\left(\frac{P_p}{2\tau}(\mathbf{R}_p-\mathbf{R}_{p+1})^2-\tau E_0^e(\mathbf{R}_p)\right)}, \quad \mathbf{R}_P = \mathbf{R}_0 \qquad (2.122)
\end{aligned}$$

i.e. as an average over the classical system of closed polymers. In eq. 2.121 the permutation symmetry of $\mathcal{P}_{poly}$ with respect to $\mathbf{R}_p$ was used. If an observable is not diagonal in the position representation, the evaluation is not so straightforward: the condition $\mathbf{R}_0 = \mathbf{R}_P$ does not hold, leading to open polymers. One fundamental observable that is not diagonal in the position representation is the total energy. However, in this case, the following thermodynamic equality can be exploited:

$$\langle E \rangle = -\frac{1}{Z}\frac{\partial Z}{\partial \beta} \qquad (2.123)$$

Using the primitive form of the partition function, we get

$$\langle E \rangle \approx \langle \frac{3N_p}{2\tau} - \sum_{p=0}^{P-1}\frac{M_p}{2\beta^2}(\mathbf{R}_p - \mathbf{R}_{p+1})^2 + \frac{1}{P}\sum_{p=0}^{P-1} E_0^e(\mathbf{R}_p)\rangle_{\mathcal{P}_{poly}} \qquad (2.124)$$

As a consequence, the kinetic energy is easily computed as

$$\langle K \rangle = \langle E \rangle - \langle V \rangle = \langle \frac{3N_p}{2\tau} - \sum_{p=0}^{P-1}\frac{M_p}{2\beta^2}(\mathbf{R}_p - \mathbf{R}_{p+1})^2\rangle_{\mathcal{P}_{poly}} \qquad (2.125)$$

The development of the primitive approximation is relatively straightforward and is the foundation of the quantum-classical isomorphism. Moreover, formally exact expressions can be obtained from eq. 2.119 when $M \to \infty, \tau \to 0$. In this regime,

$$\begin{aligned}
\left(\frac{M_p}{2\pi\tau}\right)^{\frac{3PN_p}{2}} \int d\mathbf{R}_0 \dots d\mathbf{R}_{P-1} &\to \int_{\mathbf{R}(0)=\mathbf{R},\mathbf{R}(\beta)=\mathbf{R}'} \mathcal{D}[\mathbf{R}] \\
\sum_{p=0}^{P-1} \tau \frac{M_p}{2\tau^2}(\mathbf{R}_p - \mathbf{R}_{p+1})^2 &\to \int_0^\beta d\tau \frac{M_p}{2}\left|\frac{d\mathbf{R}(\tau)}{d\tau}\right|^2 \qquad (2.126) \\
\sum_{p=0}^{P-1} \tau E_0^e(\mathbf{R}_p) &\to \int_0^\beta d\tau E_0^e(\mathbf{R}(\tau))
\end{aligned}$$

where $\int_{\mathbf{R}(0)=\mathbf{R},\mathbf{R}(\beta)=\mathbf{R}'} \mathcal{D}[\mathbf{R}]$ stands for a functional integral over al possible trajectories $\mathbf{R}(\tau)$ with the assigned endpoints. Eq. 2.119 thus becomes

$$\rho(\mathbf{R},\mathbf{R}';\beta) = \int_{\mathbf{R}(0)=\mathbf{R},\mathbf{R}(\beta)=\mathbf{R}'} \mathcal{D}[\mathbf{R}] \exp\left[-\int_0^\beta d\tau \frac{M_p}{2}\left|\frac{d\mathbf{R}(\tau)}{d\tau}\right|^2 + E_0^e(\mathbf{R}(\tau))\right] \tag{2.127}$$

While being exact, eq. 2.127 is of little practical use: the implementation of path integrals goes through eq. 2.120. Nevertheless, one can use it as the basis to develop better approaches that give results comparable to the primitive approximation with a smaller number of beads. An approximation relevant for our work is the pair product action

2.4.2 The pair product action

Eq. 2.127 can be rewritten as

$$\rho(\mathbf{R},\mathbf{R}';\beta) = \rho_0(\mathbf{R},\mathbf{R}';\beta)\frac{\int_{\mathbf{R}(0)=\mathbf{R}}^{\mathbf{R}(\beta)=\mathbf{R}'} \mathcal{D}[\mathbf{R}] \exp\left[-\int_0^\beta d\tau \frac{M_p}{2}\left|\frac{d\mathbf{R}(\tau)}{d\tau}\right|^2 + E_0^e(\mathbf{R}(\tau))\right]}{\rho_0(\mathbf{R},\mathbf{R}';\beta)} \tag{2.128}$$

$$\rho_0(\mathbf{R},\mathbf{R}';\beta) = \int_{\mathbf{R}(0)=\mathbf{R}}^{\mathbf{R}(\beta)=\mathbf{R}'} \mathcal{D}[\mathbf{R}] \exp\left[-\int_0^\beta d\tau \frac{M_p}{2}\left|\frac{d\mathbf{R}(\tau)}{d\tau}\right|^2\right] \tag{2.129}$$

where $\rho_0(\mathbf{R},\mathbf{R}';\beta)$ is the density matrix associated to free particles. On the other hand, given our definitions of kinetic and interpotential action and their limits when $M \to \infty$, the original density matrix can be written as

$$\rho(\mathbf{R},\mathbf{R}';\beta) = \rho_0(\mathbf{R},\mathbf{R}';\beta)e^{-A_U(\mathbf{R},\mathbf{R}';\beta)} \tag{2.130}$$

Putting together eq. 2.128 and 2.130, we obtain

$$\begin{aligned} e^{-A_U(\mathbf{R},\mathbf{R}';\beta)} &= \frac{\int_{\mathbf{R}(0)=\mathbf{R}}^{\mathbf{R}(\beta)=\mathbf{R}'} \mathcal{D}[\mathbf{R}]\rho_0(\mathbf{R},\mathbf{R}';\beta)\exp\left[-\int_0^\beta d\tau E_0^e(\mathbf{R}(\tau))\right]}{\rho_0(\mathbf{R},\mathbf{R}';\beta)} = \\ &= \langle \exp\left[-\int_0^\beta d\tau E_0^e(\mathbf{R}(\tau))\right]\rangle_{RW} \end{aligned} \tag{2.131}$$

with $\langle\cdots\rangle_{RW}$ stands for an averaging process over Gaussian randow walks from $\mathbf{R}$ to $\mathbf{R}'$.

If instead of the Born-Oppenheimer energy surface $E_0^e(\mathbf{R})$ we have a pair potential $V_{pair}(\mathbf{R})$

$$V_{pair}(\mathbf{R}) = \sum_{\alpha<\beta} v(\mathbf{R}_\alpha,\mathbf{R}_\beta) \tag{2.132}$$

eq. 2.131 can be written as

$$\begin{aligned} e^{-A_{U-pair}(\mathbf{R},\mathbf{R}';\beta)} &= \langle \exp\left[-\int_0^\beta d\tau \sum_{\alpha<\beta} v(\mathbf{R}_\alpha,\mathbf{R}_\beta)\right]\rangle_{RW} = \langle \prod_{\alpha<\beta} x_{\alpha\beta}\rangle \\ x_{\alpha\beta} &= \exp\left[-\int_0^\beta d\tau v(\mathbf{R}_\alpha,\mathbf{R}_\beta)\right] \end{aligned} \tag{2.133}$$

It is reasonable to assume that the main correlation effect among different particles is given by two-body terms, which exhibit a wild divergent behaviour when two particles approach; higher order terms, instead, are relatively smooth. If one assumes that the $x_{\alpha\beta}$ variables are almost independent, one obtains

$$e^{-A_{U-pair}(\mathbf{R},\mathbf{R}';\beta)} \approx \prod_{\alpha<\beta}\langle x_{\alpha\beta}\rangle = \prod_{\alpha<\beta} e^{-u_2(\mathbf{R}_{\alpha\beta},\mathbf{R}'_{\alpha\beta})} = e^{-\sum_{\alpha<\beta} u_2(\mathbf{R}_{\alpha\beta},\mathbf{R}'_{\alpha\beta})} \tag{2.134}$$

i.e.

$$A_{U-pair}(\mathbf{R},\mathbf{R}';\beta) \approx \sum_{\alpha<\beta} u_2(\mathbf{R}_{\alpha\beta},\mathbf{R}'_{\alpha\beta}) \tag{2.135}$$

where $u_2(\mathbf{R}_{\alpha\beta},\mathbf{R}'_{\alpha\beta})$ is the interpotential action for a single pair of particles. Given the form of the pair potential, this action can be computed numerically in an iterative way using the matrix-squaring method [88, 89].

2.5 Path Integral Molecular Dynamics

As explained in the previous section, relevant nuclear operators can be computed as

$$\langle O\rangle = \frac{1}{Z}\int d\mathbf{R}\tilde{O}(\mathbf{R})\rho(\mathbf{R},\mathbf{R}';\beta) \qquad \rho(\mathbf{R},\mathbf{R};\beta) = \langle \mathbf{R}|e^{-\beta(\mathcal{K}_p+E_0^e(\mathbf{R}))}|\mathbf{R}\rangle \tag{2.136}$$

where $\tilde{O}(\mathbf{R})$ is an estimator that can be more or less straightforward to obtain. As we saw, the primitive approximation gives a practical way of computing Z and the associated probability density, establishing an isomorphism between the quantum system and a classical polymer system through eq. 2.120: the isomorphism can be carried on [90] introducing $P \times N_p$ momenta $\vec{P}$ and writing

$$Z_{pa} = \left(\frac{1}{2\pi}\right)^{3PN_p}\int d\mathbf{P}d\mathbf{R}e^{-\tau H_\tau(\mathbf{P},\mathbf{R})} \tag{2.137}$$

$$H_\tau(\mathbf{P},\mathbf{R}) = \sum_{p=0}^{P-1}\frac{\mathbf{P}_p^2}{2M_p} + \frac{M_p}{2\tau^2}(\mathbf{R}_p-\mathbf{R}_{p+1})^2 + \sum_{p=0}^{P-1} E_0^e(\mathbf{R}_p) \tag{2.138}$$

The (fictitious) dynamics of such a system can be simulated implementing Hamilton's equations

$$\frac{d\mathbf{P}}{dt} = -\frac{\partial H_\tau}{\partial \mathbf{R}} \quad , \quad \frac{d\mathbf{R}}{dt} = \frac{\partial H_\tau}{\partial \mathbf{P}} \tag{2.139}$$

in a molecular dynamics scheme. A convenient theoretical tool to discuss the time evolution is the Liouville operator $\mathcal{L}$:

$$i\mathcal{L} = \sum_{\alpha=1}^{N_p} \sum_{m=0}^{P-1} \left(\frac{d\vec{R}_{\alpha,m}}{dt} \frac{\partial}{\partial \vec{R}_{\alpha,m}} + \frac{d\vec{P}_{\alpha,m}}{dt} \frac{\partial}{\partial \vec{P}_{\alpha,m}} \right) \tag{2.140}$$

In this way the evolving phase space point $(\mathbf{R}_m^t, \mathbf{P}_m^t)$ can be written as

$$\begin{pmatrix} \mathbf{R}_m^t \\ \mathbf{P}_m^t \end{pmatrix} = e^{i\mathcal{L}t} \begin{pmatrix} \mathbf{R}_m \\ \mathbf{P}_m \end{pmatrix} \tag{2.141}$$

and a good approximation of the operator $e^{i\mathcal{L}t}$ can lead to devise an efficient molecular dynamics algorithm. In our case, we can write the Hamiltonian $H_\tau(\mathbf{P}, \mathbf{R})$ as

$$H_\tau(\mathbf{P}, \mathbf{R}) = H_\tau^0(\mathbf{P}, \mathbf{R}) + \sum_{p=0}^{P-1} E_0^e(\mathbf{R}_p) \tag{2.142}$$

$$H_\tau^0(\mathbf{P}, \mathbf{R}) = \sum_{p=0}^{P-1} \frac{\mathbf{P}_p^2}{2M_p} + \sum_{p=0}^{P-1} \frac{M_p}{2\tau^2} (\mathbf{R}_p - \mathbf{R}_{p+1})^2 \tag{2.143}$$

where $H_\tau^0(\mathbf{P}, \mathbf{R})$ is the Hamiltonian of non-interacting harmonic ring polymers. The internal modes of the ring polymers present different time scales: in principle, the timestep Δt should be chosen small enough to properly integrate the fastest mode: however, H_τ^0 can be exactly solved. This suggests to approximate the time evolution operator as [91]

$$e^{i\mathcal{L}_{H_\tau}\Delta t} \approx e^{i\mathcal{L}_V \Delta t/2} e^{i\mathcal{L}_{H_\tau^0}\Delta t} e^{i\mathcal{L}_V \Delta t/2} \tag{2.144}$$

$$i\mathcal{L}_V = -\sum_{\alpha=1}^{N_p} \sum_{m=0}^{P-1} \left(\frac{dE_0^e}{d\vec{R}_{\alpha,m}} \frac{\partial}{\partial \vec{P}_{\alpha,m}} \right) \tag{2.145}$$

$$i\mathcal{L}_{H_{\tau^0}} = \sum_{\alpha=1}^{N_p} \sum_{m=0}^{P-1} \left(\frac{\vec{P}_{\alpha,m}}{M_p} \frac{\partial}{\partial \vec{R}_{\alpha,m}} - \frac{\partial H_{\tau^0}}{\partial \vec{R}_{\alpha,m}} \frac{\partial}{\partial \vec{P}_{\alpha,m}} \right) \tag{2.146}$$

It is natural to introduce normal modes, that diagonalize H_τ^0:

$$\vec{S}_{\alpha,k} = \sum_{m=0}^{P-1} C_{km} \vec{R}_{\alpha,p} \quad , \quad \vec{Q}_{\alpha,k} = \sum_{p=0}^{P-1} C_{kp} \vec{P}_{\alpha,p} \tag{2.147}$$

with

$$C_{kp} = \begin{cases} \sqrt{\frac{1}{P}} & p = 0 \\ \sqrt{\frac{2}{P}} \cos\left(\frac{2\pi kp}{P}\right) & 1 \le p \le \frac{P}{2} - 1 \\ \sqrt{\frac{1}{P}} (-1)^k & p = P/2 \\ \sqrt{\frac{2}{P}} \sin\left(\frac{2\pi kp}{P}\right) & \frac{P}{2} + 1 \le p \le P - 1 \end{cases} \tag{2.148}$$

and H^0_τ is

$$H^0_\tau(\mathbf{Q},\mathbf{S}) = \sum_{\alpha=1}^{N_p}\sum_{k=0}^{P-1}\frac{Q^2_{\alpha,k}}{2M_p} + \sum_{m=0}^{P-1}\frac{M_p}{2}\omega_k^2|\vec{S}_{\alpha,k}|^2 \quad (2.149)$$

$$\omega_k = \frac{2}{\tau}\sin(k\pi/P) \quad (2.150)$$

The single molecular dynamics step is then performed in the following way:

- propagation using $e^{i\mathcal{L}_V\Delta t/2}$:

$$\vec{P}^1_{\alpha,p} = \vec{P}_{\alpha,p} - \frac{\Delta t}{2}\frac{\partial E^e_0}{\partial \vec{R}_{\alpha,p}} \quad (2.151)$$

$$\vec{R}^1_{\alpha,p} = \vec{R}_{\alpha,p} \quad (2.152)$$

- change of basis from $\vec{p}^1_{\alpha,p}$ and $\vec{R}^1_{\alpha,p}$ to $\vec{Q}^1_{\alpha,k}$ and $\vec{S}^1_{\alpha,k}$ using eq. 2.147 and eq. 2.148 and then propagated as

$$\begin{pmatrix}\vec{S}^2_{\alpha,k}\\ \vec{Q}^2_{\alpha,k}\end{pmatrix} = \begin{pmatrix}\cos(\omega_k\Delta t) & -M_p\omega_k\sin(\omega_k\Delta t)\\ \frac{1}{\omega_k M_p}\sin(\omega_k\Delta t) & \cos(\omega_k\Delta t)\end{pmatrix}\begin{pmatrix}\vec{S}^1_{\alpha,k}\\ \vec{Q}^1_{\alpha,k}\end{pmatrix} \quad (2.153)$$

  that is the exact propagation for independent harmonic oscillators.

- change of basis back to Cartesian coordinates $\vec{P}^2_{\alpha,p}$ and $\vec{R}^2_{\alpha,p}$ and final propagation using again $e^{i\mathcal{L}_V\Delta t/2}$:

$$\vec{P}_{\alpha,p}(t+\Delta t) = \vec{P}^2_{\alpha,p} - \frac{\Delta t}{2}\frac{\partial E^e_0}{\partial \vec{R}^2_{\alpha,p}} \quad (2.154)$$

$$\vec{R}_{\alpha,p}(t+\Delta t) = \vec{R}^2_{\alpha,p} \quad (2.155)$$

While Δt should be small enough to accurately integrate the whole trajectory, it can be larger than the corresponding timestep used for a standard Verlet algorithm, since the internal degrees of freedom of the polymers are propagated according to the exact harmonic Hamiltonian.

The above scheme produces an energy-conserving trajectory, sampling the microcanonical ensemble, which is not what is required by the isomorphism.

2.5.1 Path Integral and Langevin Equations

The canonical ensemble can be sampled through the Langevin dynamics [68, 91]

$$d\vec{P}_{\alpha,p}(t) = -\frac{\partial H}{\partial \vec{Q}_{\alpha,p}} - \gamma\vec{P}_{\alpha,p}(t) + \sqrt{\frac{2M_p\gamma}{\tau}}\vec{\xi}_\alpha(t) \quad (2.156)$$

$$d\vec{Q}_{\alpha,p}(t) = \frac{\vec{P}_{\alpha,p}(t)}{M_p}dt \quad (2.157)$$

(Itoh convention) where γ is a friction coefficient, $\vec{\xi_\alpha}(t)$ is a Gaussian random noise with zero average and such that $\langle\vec{\xi}_\alpha(t)\vec{\xi}_\alpha(t')\rangle = \delta(t-t')$. $\vec{Q}_{\alpha,p}$ and $\vec{P}_{\alpha,p}$ represent the degrees of freedom of the system

and their canonical conjugated momenta in any representation (Cartesian coordinates or normal modes, for example). It can be proved [91, 92] that such a stochastic process can be efficiently sampled if the system goes through a time evolution governed by the following Liouvillian:

$$i\mathcal{L}_{FP} = \frac{d\vec{P}_{\alpha,p}}{dt}\frac{\partial}{\partial\vec{P}_{\alpha,p}} + \frac{d\vec{Q}_{\alpha,p}}{dt}\frac{\partial}{\partial\vec{Q}_{\alpha,p}} + i\mathcal{L}_{\gamma} \tag{2.158}$$

$$i\mathcal{L}_{\gamma} = -\gamma\left(\frac{\partial}{\partial\vec{P}_{\alpha,p}}\vec{P}_{\alpha,p} + \frac{M_p}{\tau}\frac{\partial^2}{\partial\vec{P}^2_{\alpha,p}}\right) \tag{2.159}$$

The time evolution can be approximated as

$$\begin{aligned} e^{i\mathcal{L}_{FP}\Delta t} &\approx e^{i\mathcal{L}_{\gamma}\Delta t/2}e^{i\mathcal{L}_{H^{\tau}}\Delta t}e^{i\mathcal{L}_{\gamma}\Delta t/2} \approx \\ &\approx e^{i\mathcal{L}_{\gamma}\Delta t/2}e^{i\mathcal{L}_{V}\Delta t/2}e^{i\mathcal{L}_{H^{\tau^0}}\Delta t}e^{i\mathcal{L}_{V}\Delta t/2}e^{i\mathcal{L}_{\gamma}\Delta t/2} \end{aligned} \tag{2.160}$$

This scheme reproduces the microcanonical step (eq. 2.146) introducing friction and noise at the beginning and at the end of the step with the action of the operator $e^{i\mathcal{L}_{\gamma}\Delta t/2}$, that can be represented as

$$\vec{Q}'_{\alpha,k} = c_{1,k}\vec{Q}_{\alpha,k} + \sqrt{\frac{M_p}{\tau}c_{2,k}\xi_{\alpha,k}} \tag{2.161}$$

$$c_{1,k} = e^{-\gamma_k\Delta t/2} \tag{2.162}$$

$$c_{2,k} = \sqrt{1-c^2_{1,k}} \tag{2.163}$$

As we mentioned above, friction can operate on Cartesian coordinates or normal modes equally: choosing the latter, we can specify for each normal mode the optimal friction parameter γ_k. It turns out that, for free harmonic ring polymers, the γ_k that gives the smallest autocorrelation time is

$$\gamma_k = \begin{cases} 1/\tau_0 & , \quad k=0 \\ 2\omega_k & , \quad k>0 \end{cases} \tag{2.164}$$

where τ_0 is the damping coefficient of the autocorrelation function of the centroid ($k = 0$) and can be tuned depending on the system. While the optimal choices for interacting polymers may differ, at least the high frequency internal modes should be similar, being mostly decoupled by the low frequency, physical modes. This framework is called PILE (Path Integral Langevin Equation). PILE can be used at higher temperatures, where the primitive approximation does not require a big number of slices to converge to the infinite limit. At lower temperatures, this may be an issue: in this case the PILE method can be modified, using generalized Langevin equations (PI+GLE, Path Integral Generalized Langevin Equation). The methodology is rather involved and it is discussed in several papers [93–96]. The idea behind the method is that the generalized Langevin equations can be tuned to sample a target distribution which provides exact structural properties of quantum harmonic systems for any arbitrary number of beads employed. The procedure must then only account for anharmonic and higher order effects, leading to a significant decrease of the number of beads needed to obtain fully converged results [94]

2.6 Coupled electron-ion Monte Carlo

As we have stated several times, accurate electronic energies and nuclear quantum effects must taken into account to capture the real physics of the systems we intend to investigate. The Variational Monte Carlo method was introduced to evaluate the electronic Born-Oppenheimer energy while the path integral formalism was developed to deal with quantum nuclei, introducing different approximations for the density matrix. Unfortunately, at the present time the evaluation of forces through VMC is still plagued by big relative errors, making molecular dynamics difficult to perform. The Path Integral formalism, however, can still work if used with a Monte Carlo procedure, that deals with finite energy differences.

The Coupled Electron-Ion Monte Carlo (CEIMC) method [78, 97] takes all these elements and build an algorithm whose purpose is to sample the probability density $\frac{\rho(\mathbf{R},\mathbf{R};\beta)}{\mathrm{Tr}\,\rho(\mathbf{R},\mathbf{R};\beta)}$. As we saw, the first step is to write the density matrix at an inverse temperature β as a chain of P density matrices at $\tau = \beta/P$ and then properly approximate these density matrices. While the primitive approximation is the most basic solution to this problem, in the CEIMC algorithm the expression is manipulated in the following way:

$$\rho(\mathbf{R},\mathbf{R}';\tau) = \langle \mathbf{R}|e^{-\tau(\mathcal{K}_p + E_0^e(\mathbf{R}))}|\mathbf{R}'\rangle = \langle \mathbf{R}|e^{-\tau(\mathcal{K}_p + V_{pair}(\mathbf{R}) + E_0^e(\mathbf{R}) - V_{pair}(\mathbf{R}))}|\mathbf{R}'\rangle \tag{2.165}$$

introducing an effective potential $V_{pair}(\mathbf{R})$ that has the form shown in eq. 2.132. A good effective potential, should be close to the Born Oppenheimer electronic energy $E_0^e(\mathbf{R})$, allowing us to use the primitive approximation for the terms involving the difference $E_0^e - V_{pair}$:

$$\rho(\mathbf{R},\mathbf{R}';\tau) \approx \langle \mathbf{R}|e^{-\tau(\mathcal{K}_p + V_{pair}(\mathbf{R}))}|\mathbf{R}'\rangle\, e^{-\frac{\tau}{2}(E_0^e(\mathbf{R}) - V_{pair}(\mathbf{R}) + E_0^e(\mathbf{R}') - V_{pair}(\mathbf{R}'))} \tag{2.166}$$

The first matrix element on the RHS can be approximated using the pair potential approximation developed in the previous section. In this way, the probability density $\mathcal{P} = \frac{1}{Z}\rho(\mathbf{R},\mathbf{R},\beta)$ to be sampled becomes

$$\begin{aligned}
\mathcal{P} &= \frac{1}{Z}\prod_{p=1}^{P} exp\left\{-\frac{M_p(\mathbf{R}_p - \mathbf{R}'_{p+1})^2}{2\tau} - \sum_{ij} u_2(\mathbf{R}_{ij}^m, \mathbf{R}_{ij}^{m+1})\right\} e^{-\tau\sum_{p=1}^{P}(E_0^e(\mathbf{R}_p) - V_{pair}(\mathbf{R}_p))} = \\
&= P_{pair}(\mathbf{R}_p) e^{-\tau\sum_{p=1}^{P}(E_0^e(\mathbf{R}_p) - V_{pair}(\mathbf{R}_p))} \qquad (2.167) \\
P_{pair}(\mathbf{R}_p) &= \prod_{p=1}^{P} exp\left\{-\frac{M_p(\mathbf{R}_p - \mathbf{R}'_{p+1})^2}{2\tau} - \sum_{ij} u_2(\mathbf{R}_{ij}^m, \mathbf{R}_{ij}^{m+1})\right\} \qquad (2.168)
\end{aligned}$$

where $u_2(\mathbf{R}'_{ij}, \mathbf{R}'_{ij})$ is the interpotential action for a single pair of particles. The introduction of the potential V_{pair} served two purposes:

- providing a better approximation for $\mathcal{P}$, allowing us to use a smaller number of beads to converge to the infinite limit

- $\mathcal{P}$ is written as a product of two rather different terms: one, $P_{pair}(\mathbf{R}_m)$, involving $u_2(\mathbf{R}'_{ij}, \mathbf{R}'_{ij})$, that is cheap; the other one, where the computationally expensive electronic Born Oppenheimer energy must be computed.

The second point suggest to use a multilevel Metropolis algorithm to sample the distribution [78]:

- a move in the $P \times 3N_p$ configurational space from point $\{\mathbf{R}_p\}$ to $\{\mathbf{R}'_p\}$ is proposed according to some a priori transition probability $T(\{\mathbf{R}_p\}, \{\mathbf{R}'_p\})$
- the move is accepted with probability

$$A_1 = \min\left[1, \frac{T(\{\mathbf{R}_p\}, \{\mathbf{R}_p\}')}{T(\{\mathbf{R}_p\}', \{\mathbf{R}_p\})} \frac{P_{pair}(\{\mathbf{R}_p\}')}{P_{pair}(\{\mathbf{R}_p\})}\right] \tag{2.169}$$

- if the move is accepted, a second test is performed and passed with acceptance

$$A_2 = \min\left[1, e^{-\Delta(\{\mathbf{R}_p\},\{\mathbf{R}_p\}')} e^{\tau \sum_{p=1}^{P}(V_{pair}(\{\mathbf{R}_p\}') - V_{pair}(\{\mathbf{R}_p\}))}\right] \tag{2.170}$$

$$\Delta(\{\mathbf{R}_p\}, \{\mathbf{R}'_p\}) = \tau \sum_{p=1}^{P} \left(E_0^e(\mathbf{R}'_p) - E_0^e(\mathbf{R}_p)\right) \tag{2.171}$$

The advantage of splitting the acceptance test into two phases is that the first step (also called the pre-rejection step) is not computationally demanding, not involving the computation of $E_o^e(\mathbf{R})$: it prevents the expensive evaluation of the electronic energy for moves that are not likely to be accepted. Of course, an important role is played by the effective potential V_{pair}: the more it resembles the true energy landscape, the more efficient this process becomes. In defining the scheme of the algorithm, we passed over a relevant issue: in fact, in the CEIMC method, VMC is used to compute the electronic energy difference Δ. This means that Δ itself is a statistical average and, as such, it has an associated statistical error that can bias the outcome of the acceptance test. The simplest solution would be to make this error negligible with respect to Δ and ignore this fact; but this would require sampling a lot of configurations and would be highly inefficient. Instead, we used a different approach: the penalty method.

2.6.1 The Penalty method

Given $\Delta(\{\mathbf{R}_p\}, \{\mathbf{R}'_p\})$, let $\bar{\Delta}$ and σ^2_Δ be its average value and variance respectively, computed over the noise probability distribution $P_{noise}(\Delta(\mathbf{R}_m, \mathbf{R}'_m))$. Since $\Delta(\{\mathbf{R}_p\}, \{\mathbf{R}'_p\})$ is a random variable, then the acceptance $a(\Delta)$ is a random variable as well, whose average value is

$$A(\{\mathbf{R}_m\}, \{\mathbf{R}'_m\}) = \int_{-\infty}^{\infty} d\Delta \quad a(\Delta) P_{noise}(\Delta | \{\mathbf{R}_m\}, \{\mathbf{R}_m\}') \tag{2.172}$$

On average, we want to satisfy the detailed balance condition:

$$A(\{\mathbf{R}_p\}, \{\mathbf{R}_p\}') = e^{-\bar{\Delta}} A(\{\mathbf{R}_p\}', \{\mathbf{R}_p\}) \frac{T(\{\mathbf{R}_p\}', \{\mathbf{R}_p\})}{T(\{\mathbf{R}_p\}, \{\mathbf{R}_p\}')} \tag{2.173}$$

While $P_{noise}(\Delta|\{\mathbf{R}_p\},\{\mathbf{R}_p\}')$ is unknown, we can make the simple hypothesis that

$$P_{noise}(\Delta|\{\mathbf{R}_p\},\{\mathbf{R}_p\}') = P_{noise}(\Delta) = \frac{1}{\sqrt{2\pi\sigma^2}} e^{-\frac{(\Delta-\bar{\Delta})^2}{2\sigma^2}} \tag{2.174}$$

that can be justified by invoking the central limit theorem if the energy difference Δ is averaged over many samples and has a finite variance. One can verify that if one chooses

$$\begin{aligned} a(\Delta) &= \min\left[1, \frac{T(\{\mathbf{R}_p\}',\{\mathbf{R}_p\})}{T(\{\mathbf{R}_p\},\{\mathbf{R}_p\}')} e^{\left(-\Delta-\frac{\sigma^2}{2}\right)}\right] = \\ &= \min\left[1, e^{\left(-\Delta-\frac{\sigma^2}{2}\right)} e^{-\Gamma(\{\mathbf{R}_p\}',\{\mathbf{R}_p\})}\right] \qquad (2.175) \\ \Gamma(\{\mathbf{R}_p\},\{\mathbf{R}_p\}') &= -\ln\left(\frac{T(\{\mathbf{R}_p\}',\{\mathbf{R}_p\})}{T(\{\mathbf{R}_p\},\{\mathbf{R}_p\}')}\right) \qquad (2.176) \end{aligned}$$

the average acceptance A has the form

$$\begin{aligned} A(\{\mathbf{R}_p\},\{\mathbf{R}_p\}') = \tfrac{1}{2}\mathrm{erfc}\left\{\tfrac{1}{\sqrt{2}\sigma}\left[\tfrac{\sigma^2}{2} + \bar{\Delta}(\{\mathbf{R}_p\},\{\mathbf{R}_p\}') + \Gamma(\{\mathbf{R}_p\},\{\mathbf{R}_p\}')\right]\right\} \qquad (2.177) \\ +\tfrac{1}{2}\mathrm{erfc}\left\{\tfrac{1}{\sqrt{2}\sigma}\left[\tfrac{\sigma^2}{2} - \bar{\Delta}(\{\mathbf{R}_p\},\{\mathbf{R}_p\}') - \Gamma(\{\mathbf{R}_p\},\{\mathbf{R}_p\}')\right]\right\} e^{-\bar{\Delta}(\{\mathbf{R}_p\},\{\mathbf{R}_p\}')-\Gamma(\{\mathbf{R}_p\},\{\mathbf{R}_p\}')} \end{aligned}$$

which solves the averaged detailed balance condition, since $\bar{\Delta}(\{\mathbf{R}_p\},\{\mathbf{R}_p\}') = -\bar{\Delta}(\{\mathbf{R}_p\}',\{\mathbf{R}_p\})$ and $\Gamma(\{\mathbf{R}_p\},\{\mathbf{R}_p\}') = -\Gamma(\{\mathbf{R}_p\}',\{\mathbf{R}_p\})$. The effect of the statistical noise is thus to enhance the rejection by a factor $e^{-\frac{\sigma^2}{2}}$ when compared to a first naive approach, as we can see from eq. 2.175. However, one more issue is that the variance σ is not known a priori, but it must be estimated during the run to compute the energy as well. Given n independent samples y_i, one has

$$\begin{aligned} \Delta &= \frac{1}{n}\sum_{i=1}^{n} y_i \qquad (2.178) \\ \chi^2 &= \frac{1}{n(n-1)}\sum_{i=1}^{n}(y_i-\Delta)^2 \qquad (2.179) \end{aligned}$$

which provide unbiased estimators for $\bar{\Delta}$ and σ^2. In this case, the average acceptance defined in eq. 2.172 becomes

$$A(\{\mathbf{R}_p\},\{\mathbf{R}_p\}') = \int_{-\infty}^{\infty} d\Delta \int_{0}^{\infty} d\chi^2 \quad a(\Delta,\chi^2) P_{noise}(\Delta,\chi^2|\{\mathbf{R}_p\},\{\mathbf{R}_p\}') \tag{2.180}$$

One can prove then that the new acceptance formula is

$$\begin{aligned} a(\Delta,\chi^2) &= \min\left[1, \frac{T(\{\mathbf{R}_p\}',\{\mathbf{R}_p\})}{T(\{\mathbf{R}_p\},\{\mathbf{R}_p\}')} e^{(-\Delta-u_b)}\right] \qquad (2.181) \\ u_b &= \frac{\chi^2}{2} + \frac{\chi^4}{4(n+1)} + \frac{\chi^6}{3(n+1)(n+3)}\ldots \qquad (2.182) \end{aligned}$$

where u_b is the penalty term obtained using an asymptotic expansion that converges as long as $\chi^2/n < 1/4$. This procedure is known as the penalty method [98]. For large n the first term is dominating, since χ^2 is a good enough estimator of σ^2. On the other hand the purpose of the penalty method is to get consistent results even when n is not too large: in this case the additional terms in eq. 2.182 provides an extra rejection factor motivated by our ignorance of σ.

2.6.2 Technical details

The previous section was dedicated to provide a picture of the method without indulging too much in some technical aspects, which will be addressed here.

2.6.2.1 Trial wavefunction: the orbitals

To build the trial wavefunction showed in eq. 2.104, we must supply some single particle orbitals $\theta_i(\vec{r})$ for the Slater determinant; moreover, the wavefunction should satisfy eq. 2.106 if we want to use the TABC. One can choose a wide variety of functions: in our case, we chose $\theta_i(\vec{r})$ produced by DFT calculations. If we want to average over N_θ different twists, a DFT calculation using a k-point grid made of N_θ points is performed; then, for every single $\vec{k}$ point, the solution involves the computation of $N_e/2$ filled orbitals $\theta^i_{\vec{k}}(\vec{r})$, $i = 1, N_e/2$ (the system is assumed to be not magnetic) that satisfy Bloch's theorem and thus have the form

$$\theta^i_{\vec{k}}(\vec{r}) = e^{i\vec{k}\cdot\vec{r}} u^i_{\vec{k}}(\vec{r}) \tag{2.183}$$

where $u^i_{\vec{k}}(\vec{r})$ is a function periodic in the simulation cell. As such, it can be written as

$$u^i_{\vec{k}}(\vec{r}) = \sum_{\vec{G}} C_{\vec{G}\vec{k}} e^{i\vec{G}\cdot\vec{r}} \tag{2.184}$$

If we compose a Slater determinant $S_{\vec{k}}(\vec{r}_1, \ldots, \vec{r}_{N_e/2})$ with these orbitals, it's straightforward to see that

$$S_k(\vec{r}_1, \ldots, \vec{r}_i + \vec{L}_m, \ldots, \vec{r}_{N_e/2}) = e^{i\vec{k}\cdot\vec{L}_m} S_k(\vec{r}_1, \ldots, \vec{r}_i \ldots, \vec{r}_{N_e/2}) \tag{2.185}$$

Given the (imposed) periodicity of the system, the terms $\vec{r}_i - \vec{r}_j$ or $\vec{r}_i - \vec{R}_\alpha$ of the Jastrow factor are unaffected by the displacement of an electron by a cell vector, making the whole trial wavefunction satisfy eq. 2.106. In plane-wave DFT calculation a pseudopotential is used to remove the electron-proton cusp condition. In fact, this makes the orbital smoother near the origin, leading to a fast decay of the coefficients $C_{\vec{G}\vec{k}}$ in eq. 2.184: only the G vectors satisfying the condition in eq. 2.58 are considered in the computation. In our case, a bare Coulomb interaction is used, requiring in principle a high value of E_{cut}. Instead, we implement a cusp removal method [82] by considering

$$\tilde{\theta}_{ik}(\vec{r}) = \frac{\theta_{ik}(\vec{r})}{e^{-\sum_\alpha u^{RPA}_{ep}(\vec{r}-\vec{R}_\alpha)}} \tag{2.186}$$

where u^{RPA}_{ep} is the RPA e-p Jastrow function introduced earlier. By dividing the orbitals by the analytical Jastrow factor, we remove the singularity associated to the cusp, allowing a much better convergence with respect to the orbital plane-wave basis cutoff E_{cut}. The plane waves coefficients are then Fourier transformed to real space and mapped on a local spline basis-set, which guarantees a better scaling the computation with the size of the system. Different functionals were tested: the best results in terms of minimization of the ground state energy were achieved by the PBE exchange-correlation functional [83, 99].

2.6.2.2 Trial wavefunction: the optimization of the coefficients

Our trial wavefunction has a set of 10 parameters $\{\alpha\}$ to optimize: 4 from the Jastrow factor (see eq. 2.98) and 6 from the backflow transformation (see eq. 2.103). The variational principle, as defined in VMC, consists in minimizing the energy E_0^e as function of the parameters $\{\alpha\}$: $E_0^e(\mathbf{R}) \equiv E_0^e(\mathbf{R}, \{\alpha\})$. However, for an exact eigenfunction, the associated variance σ^2 is zero: not only do we know that there is a minimum for the variance, but we know its value as well. In practice, mismatches between minimization procedures based only on energy or variance can be found, since the wavefunction is not an exact eigenfunction: it is common practice [78] to minimize a function

$$f(\{\alpha\}) = E_0^e(\mathbf{R}, \{\alpha\}) + \gamma\sigma^2(\mathbf{R}, \{\alpha\}) \tag{2.187}$$

γ is a positive coefficient, introduced to tune the relative weight of the two key quantities. A simple scheme is the following:

- given an initial set of parameters $\{\alpha_0\}$, N_c electronic configurations are generated. Then, the electronic energy and variance are estimated as

$$E(\{\alpha_0\}) = \frac{1}{N_c}\sum_{i=1}^{N_c} E_L(\mathbf{r}_i|\{\alpha_0\}) \tag{2.188}$$

$$\sigma_E^2(\{\alpha_0\}) = \frac{1}{N_c}\sum_{i=1}^{N_c} E_L^2(\mathbf{r}_i|\{\alpha_0\}) - E(\{\alpha_0\})^2 \tag{2.189}$$

- the function $f_0 = f(\{\alpha_0\}$ is evaluated and a new set of parameters $\{\alpha_1\}$ is chosen according to a Newtonian algorithm
- iterative until some convergence criterion is satisfied (e.g. $|f_{n+1} - f_n| < \epsilon$)

The problem with this scheme is that when we are in proximity of a local minima, f_n and f_{n+1} will be quite similar: since they are statistical averages, their noise can hinder the evaluation of the difference of two similar quantities. Moreover, for every step, N_c electronic configurations must be sampled. A way to make the procedure more efficient is using a correlated sampling method, known as reweighting [72]. Given two different probability distributions p_i and p_i', one can exploit the following identity

$$\langle O\rangle_{p'} = \frac{\sum_i p_i' O_i}{\sum_i p_i'} = \frac{\sum_i \frac{p_i'}{p_i} p_i O_i}{\sum_i \frac{p_i'}{p_i} p_i} = \frac{\langle O\frac{p'}{p}\rangle_p}{\langle \frac{p'}{p}\rangle_p} \tag{2.190}$$

i.e. an average over a probability distribution p_i' can be computed performing averages over a different distribution p_i. In our case we start from the initial set of parameters $\{\alpha_0\}$ and sample N_c electronic configurations, evaluating energy and variance Then, when a new set of parameters $\{\alpha'\}$ is chosen according to the minimization scheme, the averages for the new distribution are evaluated

as

$$E_0^e(\mathbf{R},\{\alpha'\}) = \frac{\sum_i^{N_c} w(\mathbf{r}_i;\mathbf{R},\{\alpha'\})E_L(\mathbf{r}_i;\mathbf{R},,\{\alpha'\})}{\sum_i w(\mathbf{r}_i;\mathbf{R},\{\alpha'\})} \tag{2.191}$$

$$\sigma_E^2(\mathbf{R},\{\alpha'\}) = \frac{\sum_i^{N_c} w(\mathbf{r}_i;\mathbf{R},\{\alpha'\})(E_L(\mathbf{r}_i;\mathbf{R},,\{\alpha'\}) - E_0^e(\mathbf{R},\{\alpha'\}))^2}{\sum_i w(\mathbf{r}_i;\mathbf{R},\{\alpha'\})} \tag{2.192}$$

$$w(\mathbf{r}_i;\mathbf{R},\{\alpha'\}) = \frac{|\psi_T(\mathbf{r}_i;\mathbf{R},\{\alpha'\})|^2}{|\psi_T(\mathbf{r}_i;\mathbf{R},\{\alpha_0\})|^2} \tag{2.193}$$

Since the same set of electronic configurations is used, these quantities are statistically correlated to the original ones: if their covariance is positive, they fluctuates in the same directions and the noise affecting the difference $\approx \sqrt{\sigma^2_{E(\{\alpha'\})} + \sigma^2_{E(\{\alpha_0\})} - 2cov(E(\{\alpha'\}), E(\{\alpha_0\}))}$ can be greatly reduced. When using eq. 2.190, there is one caveat: if the overlap between p_i and p_i' is small, the ratios $\frac{p_i'}{p_i}$ can vary a lot (p_i may be zero when p_i is finite or vice versa), leading to averages affected by big error bars and defeating the original purpose of reducing the noise; on the other hand, if the two distributions are similar, as we expect near the minimum, all the weights should be close to one. We can check which case we are in by monitoring the observable

$$N_w = \frac{\left(\sum_i^{N_c} w_i\right)^2}{\sum_i^{N_c} w_i^2} \tag{2.194}$$

If all the weights are 1, $N_w = N_c$; if they oscillate, N_w starts decreasing, since $\left(\sum_i^{N_c} w_i\right)^2 \leq N_c \sum_i^{N_c} w_i^2$. If N_w is reduced to a fraction of N_c, a new set of N_c configurations is generated, replacing the old ones.

2.6.2.3 Path integrals: proposing the protonic move

To sample the distribution in eq. 2.168 and build the appropriate Markov chain, a new protonic configuration must be proposed at every step. The efficiency of the sampling critically depends on how the new configuration is generated, i.e. on the form of the transition matrix $T(\{\mathbf{R}_p\},\{\mathbf{R}_p\}')$. In our algorithm, we use the Smart Monte Carlo approach [100], where the new configuration is

$$\{\mathbf{R}_p\}' = \{\mathbf{R}_p\} + \lambda\mathbf{F} + \mathbf{G} \tag{2.195}$$

with $\mathbf{F}$ being a $3P \times N_p$-dimensional generalized force, obtained as

$$\mathbf{F} = \frac{\partial}{\partial\{\mathbf{R}_p\}} \ln\left(P_{pair}(\{\mathbf{R}_p\})\right) \tag{2.196}$$

while $\mathbf{G}$ is $3P \times N_p$ array of independent random numbers G_i that are distributed according to

$$W(G_i) = \frac{e^{-G_i^2/(4\lambda)}}{(4\pi\lambda)^{3/2}} \tag{2.197}$$

Finally, λ is a parameter akin to a "time step" that can be tuned to optimize the portion of visited configurational space against spent computational time. From this, it follows that the transition

matrix can be written as

$$\begin{aligned} T(\{\mathbf{R}_p\},\{\mathbf{R}_p\}') &= C\int d\mathbf{G}W(\mathbf{G})\delta(\{\mathbf{R}_p\}'-\{\mathbf{R}_p\}-\lambda\mathbf{F}-\mathbf{G}) = \\ &= C'e^{-\left(\{\mathbf{R}_p\}'-\{\mathbf{R}_p\}-\lambda\mathbf{F}\right)^2/4\lambda} \end{aligned} \tag{2.198}$$

where C and C' are normalization factors, not relevant to the present discussion; this expression then can be used in eq. 2.169 to evaluate the acceptance of the first step. In the SMC method we drive the system towards configurations which are the most relevant to the probability distribution, thanks to the knowledge of the distribution itself: the time spent equilibrating the system (i.e. disregarding configurations where the Markov chain has yet to reach the target probability distribution) is greatly reduced and the efficiency of the sampling is improved at fixed computational effort.

However, when dealing with path integrals, there is still room for improvement: harmonic ring polymers have internal modes that may move at very different frequencies. Treating their motion using one single timestep ($\approx\lambda$) has consequences on the efficiency of the sampling: a small timestep should be used to capture the fastest vibrations, but then many steps are needed to properly sample slower modes. This issue is essentially the same we tackled when dealing with Langevin equations in PIMD. Here λ is akin to γ may : the problem be addressed by replacing the scalar λ defined in eq. 2.195 with a tensor, providing different drifts for different degrees of freedom. As in that case, we switch from Cartesian coordinates $\vec{R}_p$ of a single polymer to the corresponding normal modes ($\vec{S}_k$, $k=1,\ldots,P$), obtained through the unitary transformation in eq. 2.148. In this basis the harmonic action can be written as

$$A_K = \frac{1}{2}\sum_{k=0}^{P-1}\frac{\mathbf{S}_k^2}{\sigma_k^2} \quad , \quad \sigma_k^2 = \frac{\tau}{4M_p\sin^2\left(k\pi/P\right)} \tag{2.199}$$

For free particles, eq 2.195 becomes

$$\{\mathbf{S}_k\}' = \mathbf{Q}_k - \lambda\frac{\{\mathbf{S}_k\}}{\sigma_k^2} + \mathbf{G} \tag{2.200}$$

It's easy to see that if we choose $\lambda_k \equiv \tilde{\lambda}\sigma_k^2$, then

$$e^{-(A'_K-A_K)}\frac{T(\{\mathbf{Q}_k\},\{\mathbf{Q}_k\}')}{T(\{\mathbf{Q}_k\},\{\mathbf{Q}_k)\}} = 1 \tag{2.201}$$

and the move is always accepted. While this is not true for interacting system, using this kind of λ_k greatly enhances the acceptance. The reason is the same as in PIMD: high frequency terms should be uncoupled from the low frequency, physical modes and thus be sampled exactly. As in PIMD, the centroid (k=0 mode) does not move in this scheme since $\lambda_{k=0}=0$; a different, tunable λ_0 is used, depending on the system and on the thermodynamic conditions.

2.6.2.4 Evaluating the electronic energy differences

When computing electronic energy differences $E_0^e(\mathbf{R}')-E_0^e(\mathbf{R})$, we want an estimator with an associated error as small as possible, since it is used to evaluate the acceptance in the penalty method. To obtain this, a sampling procedure based on reweighting is employed, similar in spirit

to what happens during the optimization procedure [78]. In this case, we sample N_c electronic configurations according to the probability distribution

$$P(\mathbf{r}|\mathbf{R},\mathbf{R}') \propto |\Psi_T(\mathbf{r}|\mathbf{R})|^2 + |\Psi_T(\mathbf{r}|\mathbf{R}')|^2 \tag{2.202}$$

and the two energies $E_0^e(\mathbf{R}')$ and $E_0^e(\mathbf{R})$ are obtained as

$$E_0^e(\mathbf{R}) = \frac{\sum_{i=1}^{N_c} E_L(\mathbf{r}_i|\mathbf{R})p_i}{\sum_{i=1}^{N_c} p_i} \quad , \quad p_i = \frac{|\Psi_T(\mathbf{r}_i|\mathbf{R})|^2}{P(\mathbf{r}_i|\mathbf{R},\mathbf{R}')} \tag{2.203}$$

$$E_0^e(\mathbf{R}') = \frac{\sum_{i=1}^{N_c} E_L(\mathbf{r}_i|\mathbf{R}')p_i'}{\sum_{i=1}^{N_c} p_i'} \quad , \quad p_i' = \frac{|\Psi_T(\mathbf{r}_i|\mathbf{R}')|^2}{P(\mathbf{r}_i|\mathbf{R},\mathbf{R}')} \tag{2.204}$$

$$\Delta E_0^e = \sum_{i=1}^{N_c} E_L(\mathbf{r}_i|\mathbf{R}')\frac{p_i'}{\sum_{i=1}^{N_c} p_i'} - E_L(\mathbf{r}_i|\mathbf{R})\frac{p_i}{\sum_{i=1}^{N_c} p_i} \tag{2.205}$$

As a result of the correlation induced by using the same set of electronic configurations, the variance of ΔE_0^e from eq. 2.205 is smaller than the variance of the two statistically independent energy averages. Moreover, with $P(\mathbf{r}|\mathbf{R},\mathbf{R}')$ the sampling of the electronic phase space is not limited to configurations that are relevant only for $\mathbf{R}'$ or only for $\mathbf{R}$. If, for instance, we sample according to $|\Psi_T(\mathbf{r}_i|\mathbf{R})|^2$, electronic configurations near the nodal surfaces of $\Psi_T(\mathbf{r}_i|\mathbf{R})$ are rarely selected; the same configurations, however, may be relevant for $\mathbf{R}'$, since the nodal structure of the wavefunction depends on the nuclear positions. In this case, the reweighting procedure would break since the weights $|\Psi_T(\mathbf{r}_i|\mathbf{R})|^2 / |\Psi_T(\mathbf{r}_i|\mathbf{R}')|^2$ would be wildly oscillating, as discussed for the optimization. The problem is avoided with $P(\mathbf{r}|\mathbf{R},\mathbf{R}')$.

Chapter 3

High pressure solid hydrogen

In this chapter we will present the results obtained by DFT-PIMD and CEIMC simulations for high pressure solid hydrogen at low temperatures. In particular, the succession of phase transitions at T=200 K with the recent proposal of yet another solid phase which may be semi-metallic [18] makes this region of the phase diagram a natural choice for our computations at finite temperature. Another interesting region involves the boundaries of phase IV at higher temperatures ($\approx$ 400 K), close to the melting line.

In order to assess the stability of one crystal structure with respect to another at finite temperature, one should compute the respective free energies and compare them. Unfortunately, at the moment, the accuracy required to perform a meaningful calculation of the free energies for several candidate structures at finite temperature is beyond our computational resources. However, we will use DFT-PIMD and CEIMC simulations to characterize at a dynamical level relevant crystal structures. Our main aim is to properly include nuclear quantum effects in our simulations, so that we can directly compare DFT and VMC energetics at finite temperature. In fact, CEIMC simulations will act as a benchmark for the goodness of the exchange-correlation functional employed.

When simulating solids at constant volume, it is crucial to start with the "right" crystal symmetry, since the constraints imposed by the geometry of the cell may not be compatible with the true stable structure: a metastable structure could become de facto stable. Moreover, even if this is not the case, high energy barriers may prevent the transition to the stable phase to occur within the time limit imposed by the simulation. Unfortunately, as explained in chapter 1, experiments cannot provide rigid constraints for the crystal structures.

We will proceed as follows: we will introduce the crystal lattices relevant in the aforementioned regions of the phase diagram, which will be selected as starting configurations in our simulations. The selection of these lattices will be motivated through a brief overview of past theoretical works performed in similar thermodynamics conditions, with different degrees of approximations. Then, the simulation protocol adopted for both DFT-PIMD and CEIMC simulations will be stated and, finally, our results will be presented and discussed.

3.1 Crystal structures

Crystal structures are classified according to their space group, i.e. to the set of symmetry operations which leave the crystal lattice unchanged. In three dimensions, 230 space groups exist and they will be referred using the Hermann-Mauguin notation [101]. As will be explained in the following section, the candidate structures for the different solid phases of hydrogen are based on Pickard and Needs's works [43, 102]. Several different competitive lattices were found in this search for stable structures for high pressure solid hydrogen: most of them are formed by bidimensional layers stacked in various ways.

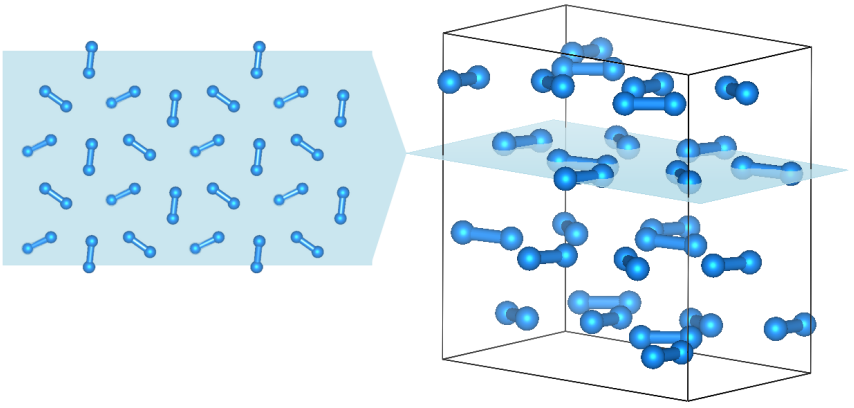

FIGURE 3.1: The C2c structure, based on the lattice proposed at P=300 GPa in the supplementary material of ref. [102]. Right panel: a 3D view, depicting the four layers stacked in an ABCD fashion. The layers are made of molecules nearly parallel to the respective planes. Left panel: a top view of one layer. The molecular centers form a distorted hexagonal lattice. The primitive cell contains 24 atoms.

For example, a strong candidate for phase III is the C2c structure, depicted in fig. 3.1: four layers, alternating in an ABCDA fashion. The arrangement of the molecules within the layers (see fig. 3.1) creates a non vanishing electric dipole moment, leading to a relatively strong infrared signal [102], compatible at least qualitatively with experimental results [41]. A structure that is competitive at higher pressures (P>250 GPa) is the Cmca12 lattice (fig. 3.2). In this case the molecular layers are arranged in an ABAB fashion: the molecules are completely parallel to the planes.

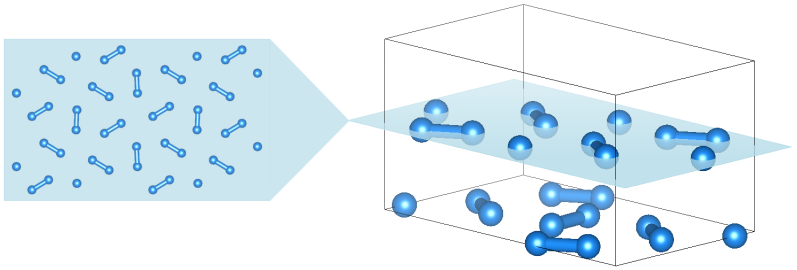

FIGURE 3.2: The Cmca12 structure, based on the lattice proposed at P=300 GPa in the supplementary material of ref. [102]. Right panel: a 3D view, depicting the two layers stacked in an AB fashion. The layers are made of molecules that lie parallel to the respective planes. Left panel: a top view of one layer. The arrangement of the molecular centers is similar to the C2c layers, but in this case the distortion from the hexagonal symmetry is larger. The primitive cell contains 12 atoms.

Another competitive structure is Cmca4 (fig. 3.3): the symmetry group is the same as Cmca12, but in this case the primitive cell contains 4 atoms. It would be more appropriate to talk about this structure in terms of orthorombic symmetry, since distances among in-plane and out-of-plane molecules are comparable; nevertheless, it is still useful when comparing with the other structures.

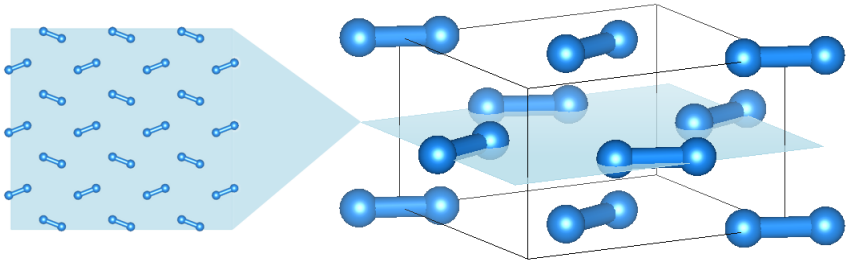

FIGURE 3.3: The Cmca4 structure, based on the lattice proposed at P=300 GPa in the supplementary material of ref. [102]. Right panel: a 3D view, depicting the layers stacked in an ABAB fashion.Left panel: a top view of one layer. Given the geometry of the cell, talking about layers is quite arbitrary. The primitive cell contains 4 atoms.

3.1.1 Mixed structures

C2c, Cmca12 and Cmca4 are all molecular layered structures. In the search for the most stable lattices, a different class of structures emerged: they still have layers, but the hydrogen atoms within the planes can be arranged in different ways, not necessarily forming molecules. An example is the Ibam structure, pictured in fig. 3.4. There are layers stacked in an ABAB fashion but, while the A layers are still formed by molecules, the hydrogen atoms in the B layers form a hexagonal network: in this sense, they are referred as mixed structures. Similar structures are Pbcn (fig. 3.5) and Pc48 (fig. 3.6). They are conceptually similar to the Ibam structure, mostly differing because the networks in the B layers depart from the perfect hexagonal symmetry present in the Ibam structure. For Pbcn, the distortion is relatively small, as we can see from the left panel of fig. 3.5; instead, for Pc48, the distortion is so big that one can reintroduce weakly bonded molecules even in the B layers (left panel of fig. 3.6).

3.2 Previous works

The lattices described in the previous section were obtained by Pickard et al. [43,102] using Ab Initio Random Structure Searching (AIRSS) to find candidate structures without hardly any experimental input. They employed DFT with the PBE functional to compute static energies and then account for quantum nuclei and temperature effects within the harmonic approximation. Their results, with the consequent phase diagram, are represented in figs. 3.7 and 3.8, where C2c is the candidate for phase III, transitioning to another phase, represented by Cmca4. The transition pressure (around 220 GPa) is almost temperature-independent in a large portion of the phase diagram; moreover, from DOS calculations Cmca4 results to be a weak metal already at P=250 GPa [105]. These two claims do not seem to be supported by recent experimental data [5].

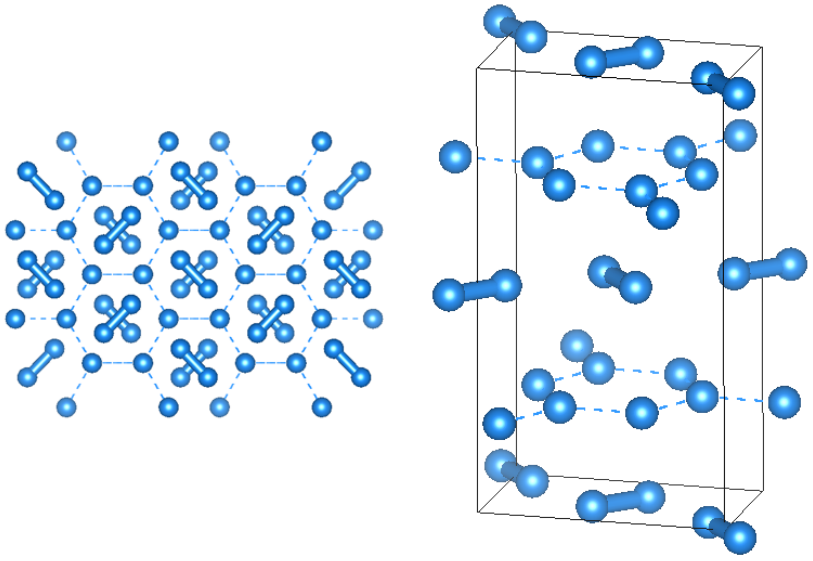

FIGURE 3.4: The Ibam structure, based on the lattice proposed at P=300 GPa in the supplementary material of ref. [102]. Right panel: a 3D view, depicting the four layers stacked in an ABAB fashion. The A layers are made of molecules, while the B layers are formed by an atomic hexagonal network. Left panel: a top view of the whole structure on the right (four layers). The dashed lines connect the atoms in the B layers. The primitive cell contains 8 atoms.

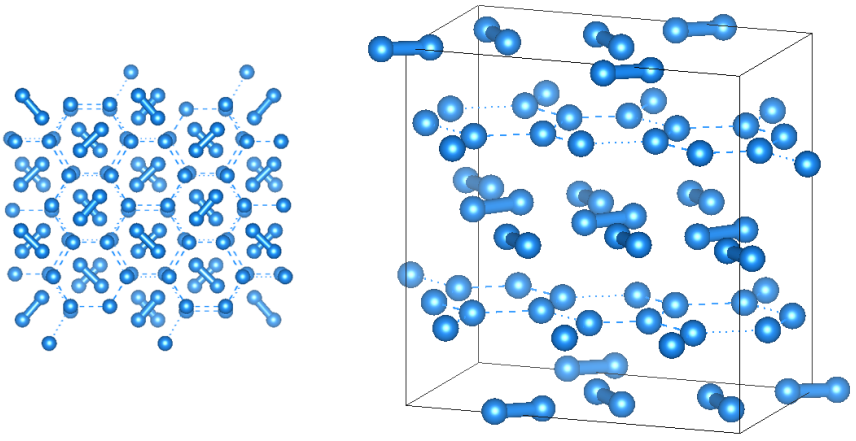

FIGURE 3.5: The Pbcn structure, based on the lattice proposed at P=300 GPa in the supplementary material of ref. [102]. Right panel: a 3D view, depicting the four layers stacked in an ABAB fashion. The A layers are made of molecules, while the B layers are formed by a nearly hexagonal network of atoms. Left panel: a top view of the whole structure on the right (four layers). The dashed lines connect the atoms in the B layers. The primitive cell contains 48 atoms.

Such results are affected by the approximations used for the calculation of the electronic energy and for neglecting anharmonic terms at finite temperatures. Fig. 3.7, in particular, shows how tiny are the free energy differences among different structures ($\approx$ meV/atom): the approximations used could easily introduce errors of the same order of magnitude. This consideration motivated different kinds of works:

- dynamical simulations (MD and PIMD) at finite temperature performed with DFT (either employing PBE or other exchange correlation functionals). These calculations could investigate

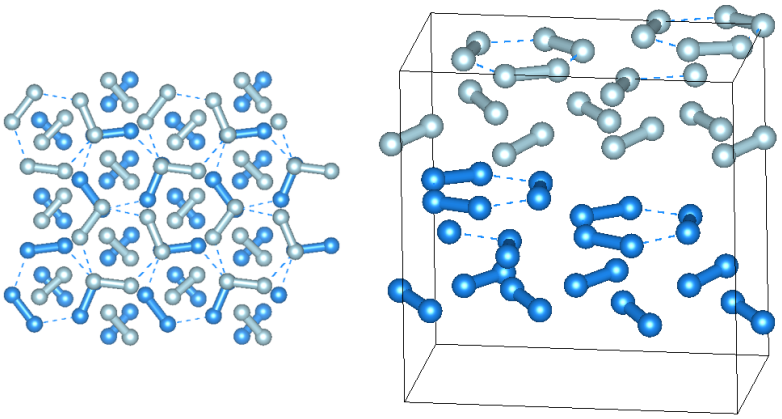

FIGURE 3.6: The Pc48 structure, based on the lattice proposed at P=250 GPa in the supplementary material of ref. [43]. Right panel: a 3D view, depicting the four layers stacked in an ABAB fashion. The A layers are made of molecules, while the B layers are formed by a distorted hexagonal network of atoms. The top two layers have a different color from the bottom ones to distinguish them in the left panel. Left panel: a top view of the whole structure on the right (four layers). The distortion of the hexagonal lattice introduces different distances among first neighbours: solid cylinders and dashed lines account for that. The primitive cell contains 48 atoms.

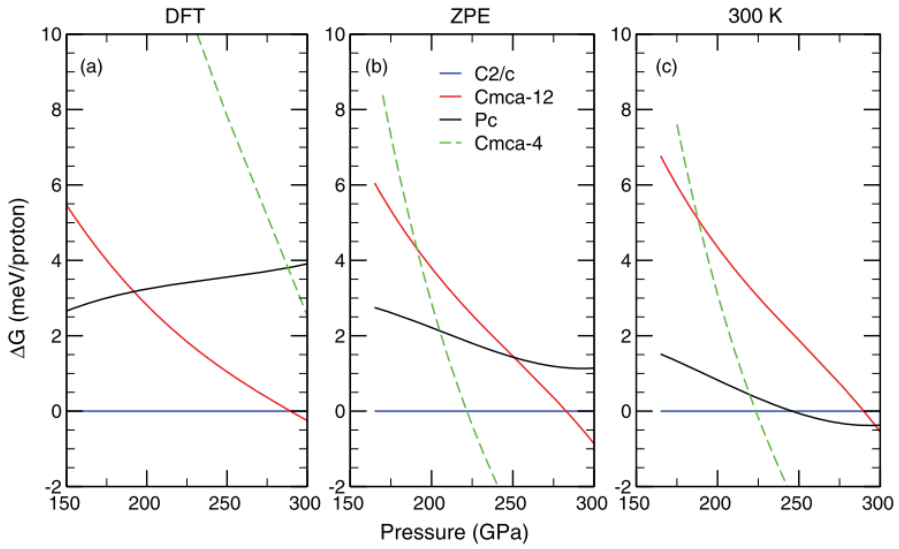

FIGURE 3.7: Free energies for different candidate structures. a) Static lattices b) Static lattices + harmonic zero point motion c) Harmonic approximation at T=300 K. Figure from ref. [103]

both the influence of the choice of the exchange-correlation functional and classical and quantum nuclear effects on the stability of the different structures.

- static calculations performed using Quantum Monte Carlo methods to obtain better electronic energies. However, the treatment of finite temperature effects, still relies on harmonic/anharmonic approximations. These approximations are still based on DFT calculations. which may be affected by the very same problem.

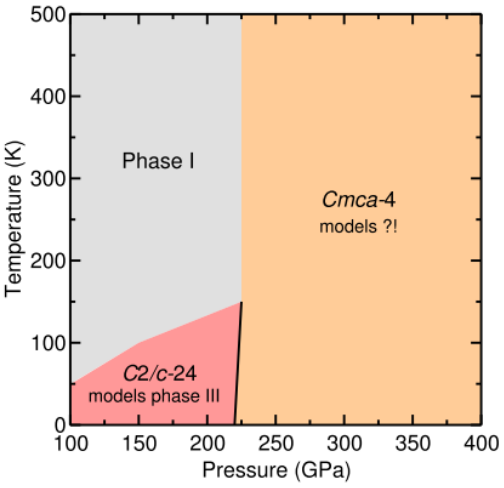

FIGURE 3.8: Phase diagram obtained from PBE-DFT static calculations within the harmonic approximation, from the supplementary material of ref. [104]. The transition pressure from C2c to Cmca4 at 0 K is compatible with the pressure found in ref. [103]

3.2.1 Dynamical simulations

3.2.1.1 Classical protons with the PBE functional

Simulations at constant temperature and pressure (NPT) with classical protons and PBE-DFT were performed by Goncharov et al. [106] , starting from the Pbcn structure around 300 K. They find that, at P=250 GPa and T=250 K, the average position of the nuclei in the atomic layers form the hexagonal pattern, peculiar of the Ibam structure; on the other hand, the molecules in the other layers have an intense rotational activity. Increasing pressure and temperature, all the layers become equivalent, and at T=300 K and P=370 GPa there is a transition to a Cmca4 structure. GW calculations were performed on static structures to compute the band gap, finding that it vanishes around the transition pressure.

NPT simulations with classical protons and PBE DFT were also performed by Liu et al. [107], starting from the C2c structure in the pressure range 250-350 GPa at temperatures of 300-500 K. At P=250 GPa between 240 and 270 K, a transition to a mixed structure takes place, which has the same features pointed out by Goncharov: rotating molecules in the molecular layers and hexagonal symmetry in the atomic layers. Moreover, protons in the hexagonal layers are found to occasionally "hop" from one site of the lattice to another: in the long run, an atom can diffuse through the layer by multiples hops.

Magdau et al. [108] performed NPT simulations starting from C2c or Pc48. The most interesting results are obtained from the simulations starting from Pc48, which seems to evolve to a structure with different inequivalent layers: a layer of free rotating molecules (B); a layer where molecules form static hexagonal trimers (G'); and a layer of rotating hexagonal trimers (G''). They are stacked in a $BG'BG''$ fashion (see fig. 3.9).

Since only rotating layers are observed, they reject the diffusion phenomenon proposed by Liu et al., dismissing it as a finite size effect. However, another work by Liu [109] claims to observe diffusion

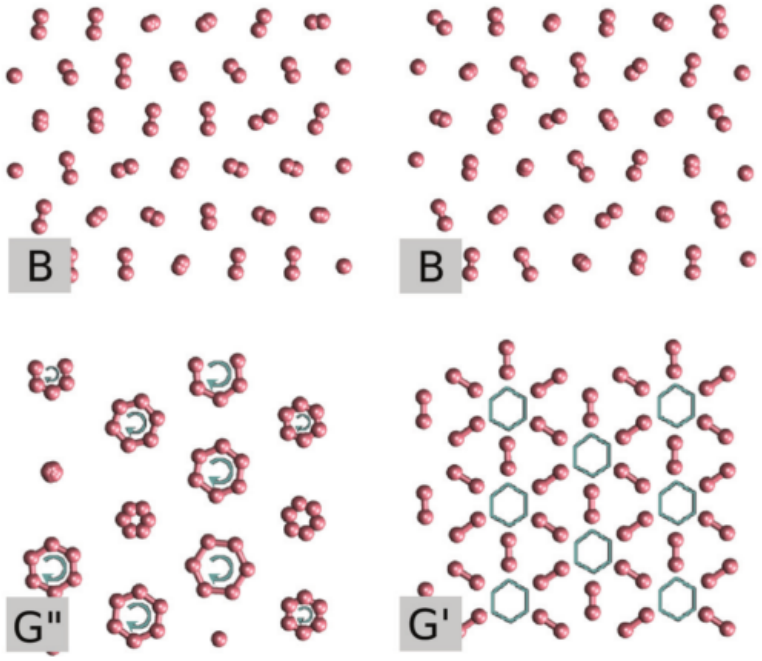

FIGURE 3.9: The different layers found by Magdau et al. [108]: B layers, made of rotating molecules; G' layers, made of static hexagonal trimers; G" layers, made of rotating hexagons.

in bigger systems and that the different kinds of hexagonal layers reported by Magdau were an artefact caused by the lack of ergodicity due to relatively short runs (1-3 ps) as opposed to the 7-90 ps simulations in Liu's works.

3.2.1.2 Introducing nuclear quantum effects and comparing PBE with other functionals

While displaying an interesting (and conflicting) phenomenology, the works mentioned in the previous paragraphs do not include nuclear quantum effects nor question the choice of the PBE functional. The use of different exchange correlation functionals in conjunction with nuclear quantum effects for hydrogen was first considered by Morales et al. [110] in the liquid phase and then extended to solid hydrogen in ref. [111], where path integral molecular dynamics was employed along with the vdW-DF2 E_{xc} to study structural properties of different crystal structures (C2c, Cmca12, Pbcn) at T=200 K. Evident nuclear quantum effects were detected in structural properties, such as the pair distribution functions: the quantum delocalization of the protons cause a broadening of the peaks and a general smoothing. The rotational activity of the molecules is also affected and found to increase when quantum nuclear effects are included. The choice of the E_{xc} functional has its effects as well: using vdW-DF2 instead of PBE results in more pronounced molecular features, opposing in some way the delocalization of the quantum nuclei. The combination of nuclear quantum effects and different functionals results in pronounced differences in the magnitude of the band gap: PIMD + PBE leads to band gap closures at P=200 GPa, in open contrast with experiments; on the other hand, PIMD+ vdW-DF2 gets better results. Another deficiency of PBE used in conjunction with nuclear quantum effects is the position of the melting line: PIMD + PBE simulations produce dynamical melting at 500 K and $150 < P < 200$ GPa, a region where hydrogen is solid according to

experiments [5]. The work also estimated the error on the enthalpy differences among structures introduced by the harmonic approximation as being of about 10 meV per proton.

A similar study was performed by Chen et al. [112], who studied Pc and Cc structures at T=300 K, using both MD and PIMD, PBE and opt88-vdW functionals. They found the same layered structure of rotating molecules and hexagonal, graphene-like layers already mentioned before. The main effect of the quantum nuclear effects is to suppress the molecular character of the graphene layers, making them more atomic, hence re-establishing a less distorted structure. A comparison of energetics with Diffusion Monte Carlo calculations reveals that energy differences between configurations with molecular layers and configurations with atomic layers are severely underestimated by PBE ($\approx$ 20 meV), making dissociation easier. On the other hand, this effect is partly mitigated by the opt88-vdW functional. They suggest the same compensation mechanism proposed by Morales between the lack of nuclear quantum effects and the use of PBE leading to results in qualitatively agreement with experiments.

3.2.2 Static simulations

Dynamical simulations need an Ab Initio computation at each step: expensive state of the art techniques cannot be used to evaluate the electronic energies at finite temperature or during a random search for the minimum. However, they can be used to evaluate the energies of an handful of candidates, such as the ones found through DFT.

To determine stability ranges of different candidate structures at T=0 K, Azadi et al. [113] computed static energies and pressures using Diffusion Monte Carlo. Quantum zero point energy must then be accounted for: the harmonic approximation was implemented using phonon frequencies obtained by DFT calculations. An estimate of the anharmonic corrections for enthalpies gave results in the range of 8-20 meV per proton [113], depending on the structure. Given the quantitative limitations imposed by the approximations, they expect the following stability ranges: C2c (220-360 GPa); Cmca12 (360-430 GPa); Cmca4 (P>430 GPa). This approach was then refined in a subsequent paper [114], introducing ahnarmonic corrections with a self-consistent method [115]: this has the effect to greatly reduce the stability range of Cmca4 to the point of making this structure unstable when compared to Cmca12 (stable up to 374 GPa) and to a candidate lattice for a purely atomic phase, $I4_1/amd$.

McMinis et al. [116] performed a similar calculation employing Diffusion Monte Carlo for static energies and vdW-DF DFT for harmonic zero point energies, finding the same chain of transitions (C2c->Cmca12->$I4_1/amd$) but with very different transition pressures (the first transition occurs at 424 GPa and the second one at 447 GPa); given the small range of stability of Cmca12 ($\approx$ 20 GPa) and the errors involved in the calculations, even the existence of a stable Cmca12 is questioned. They suggested that the different results obtained by Azadi could possibly depend on using structures optimized with PBE and on the procedure to correct finite size errors; on the other hand no anharmonic corrections were explicitly take into account. This study also shows how the phase diagram at zero temperature quantitatively depends on the functional employed for the calculation of the total enthalpy(fig. 3.10): the sequence of transitions is the same, but the transition pressures and the stability ranges wildly vary (even hundred of GPas).

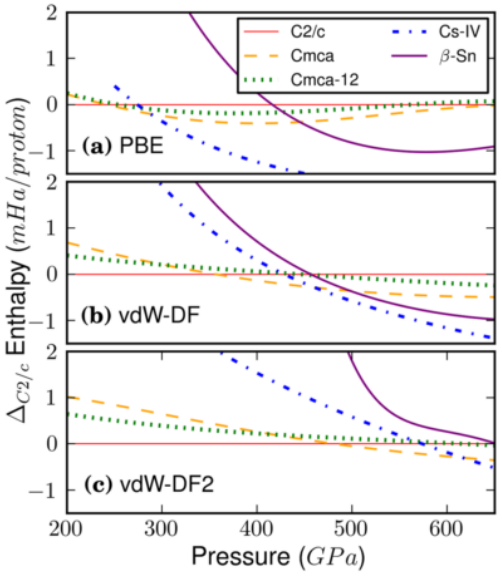

FIGURE 3.10: DFT Enthalpy (with harmonic zero point energy) computed for several structures using different functionals. In this case CsIV is equivalent to $I4_1/amd$ in the text. Picture from ref. [116]

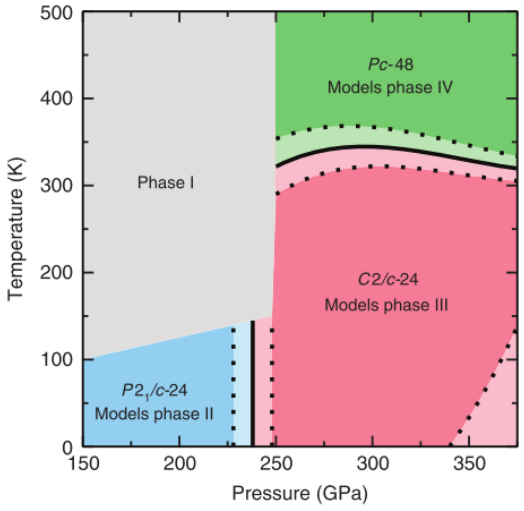

FIGURE 3.11: Phase diagram obtained in ref. [104]. Shaded regions within dotted lines show where the free energy difference between two phases is zero within one error bar.

Drummond et al. [104] extended this type of studies to finite temperature: again, Diffusion Monte Carlo is the basis for the energies and DFT is used to compute anharmonic corrections (BLYP and PBE functionals are considered). Anharmonic corrections to relative enthalpy *differences* are found to be of about 10 meV, which is the same order of magnitude of the harmonic ones; this implies that a correct determination of the phase diagram must take anharmonic effects into account. The results are that harmonic corrections stabilize Cmca12,Cmca4 and Pc48 with respect to C2c; on the other hand, anharmonic corrections have the opposite effect, destabilizing them. The resulting phase diagram is reported in fig. 3.11: Cmca12 and Cmca4 are nowhere to be found within the pressure ranges considered and Pc48 emerges as the natural candidate for phase IV at

higher temperatures. Almost ironically, this was first suggested by Pickard [43] using PBE-DFT; the calculations, however, were affected by an error that overestimated the Cmca4 enthalpy [103].

3.3 Setup of the simulations

As stated at the beginning of this chapter we will focus on the T=200 K isotherm and P>200 GPa. An interesting question is the number of transitions occurring. We saw that PBE-DFT simulations predict a stable C2c phase at relatively lower pressures: then, static calculations predict a stable Cmca4, while different kinds of finite temperature simulations predict an intermediate mixed phase. On the other hand, similar static calculations employing Quantum Monte Carlo methods "replace" Cmca4 with Cmca12 within a stability range that varies considerably between the different studies before entering in an atomic stable phase. At higher temperatures, close to the melting line, a mixed phase (Pc48) remain. We performed both DFT-PIMD and CEIMC simulations. DFT-PIMD simulations were performed using the vdW-DF exchange-correlation functional [67], which provides the best energetics for high pressure hydrogen among different affordable functionals when compared against Quantum Monte Carlo results [117]; the data obtained complete the work by Morales et al. [111], where different exchange-correlation functionals are used in conjunction with PIMD for different crystal structures at T=200 K. CEIMC simulations are used as a benchmark of DFT results: the two Ab Initio methods can be directly compared since nuclear quantum effects are fully accounted for at finite temperature using path integrals.

Because of the computational cost of the CEIMC method, we investigated a limited number of thermodynamic points and structures: however, we do not want to assess the stability ranges of the different structures but, as already mentioned, provide a benchmark for DFT and use CEIMC as an exploratory tool.

At T=200 K, in a pressure range of 250-500 GPa, we considered: C2c, Cmca12 and Cmca4 for DFT-PIMD, since they are structures found at zero temperature using different exchange correlation functionals; C2c and Cmca12 for CEIMC, given that the presence of a stable Cmca4 is only seen using DFT. At T=414 K we considered only Pc48 in a range of 250-350 GPa, since both DFT and QMC find stable mixed structures at higher temperatures. The supercells used in the simulations contain 96 hydrogen atoms: this size guarantees four layers for the structures mentioned above.

Both DFT-PIMD and CEIMC were used to perform simulations at constant temperature T and volume Ω: consequently, each thermodynamic point is conveniently identified by the temperature and the parameter r_s, defined as $\frac{4}{3}\pi r_s^3 a_0^3 = \frac{\Omega}{N}$[1]. For each considered pressure, the structures mentioned above were optimized at constant pressure using vdW-DF DFT with the algorithms for geometry optimization implemented in Quantum Espresso [62]; the resulting supercells were then used as a starting point for the simulations. In principle, different structures optimized at the same pressure would have a different equilibrium volume and, therefore, a different r_s; these structures, however, are so similar that at the same pressure the respective r_s values differ by less than 1%. A convenient one-to-one correspondence between r_s and optimization pressure can be established, regardless of the structure (see tab. 3.1)

[1] a_0 is the atomic unit of length. Using this definition, r_s is a dimensionless parameter.

TABLE 3.1: Table summarizing the correspondence between optimization pressure P and the parameter r_s

Pressure (GPa)	r_s
200	1.42
250	1.38
300	1.34
350	1.31
400	1.29
450	1.27
500	1.25
550	1.23

3.3.1 DFT-PIMD

PIMD simulations were performed using a modified version of VASP [60], which incorporated the PI+GLE method to generate the suitable NVT ensemble: 16 beads were used at T=200 K, with a Trotter time step $\tau = 0.0003125\ K^{-1}$, the same value that was used in ref. [111]; 8 beads at T=414 K, with $\tau \approx 0.0003019\ K^{-1}$. As already mentioned, we used the vdW-DF functional [67], which gives the most consistent results with Quantum Monte Carlo calculations [117]. A PAW pseudopotential [64] was employed, with an energy cutoff of 350 eV and a 2x2x2 Monkhorst-Pack grid of $\vec{k}$ points; a time-step of 0.2 fs was used.

3.3.2 CEIMC

3.3.2.1 Variational Monte Carlo setup

TABC were enforced, using a grid of 4x4x4 twists. The single particle orbitals were obtained through a PBE-DFT self consistent calculation, with $E_{cut} = 540$ eV with the same 4x4x4 grid of $\vec{k}$ points. In principle, the electronic wavefunction should be optimized at every CEIMC step. This is quite expensive, even with the reweighting procedure described in the previous chapter. In this case, we optimized the wavefunction on the initial protonic configuration (i.e. the perfect crystal). While TABC and twist averaging are used during the actual run, the minimization is performed only on one twist: previous calculations showed that no appreciable difference is present [99]. The function $f(\{\alpha\})$ introduced in eq. 2.187 is evaluated on ≈ 2000 electronic configurations; we set $\gamma = 0.25$.[2] An example is reported in fig. 3.12: as expected, the minimum of the energy and of the variance is not the same, since the wavefunction is not an exact eigenstate. Nevertheless, the energy oscillations are of about $2 \cdot 10^{-5}$Ha/proton ≈ 0.5 meV.

Without phase transitions, atoms oscillate around the equilibrium positions: assuming a smooth continuity of the parameters, the introduced bias should be minimum. We check that this is indeed the case monitoring the variance σ_E^2 during the whole trajectory (fig. 3.13): a stationary value of the variance with small fluctuations means that the quality of the wavefunction remains the same for the sampled protonic configurations.

[2] In this way the electronic energy weights more than the variance in the optimization procedure. Generally speaking, the variance is zero for every eigenfunction, not only for the ground state one.

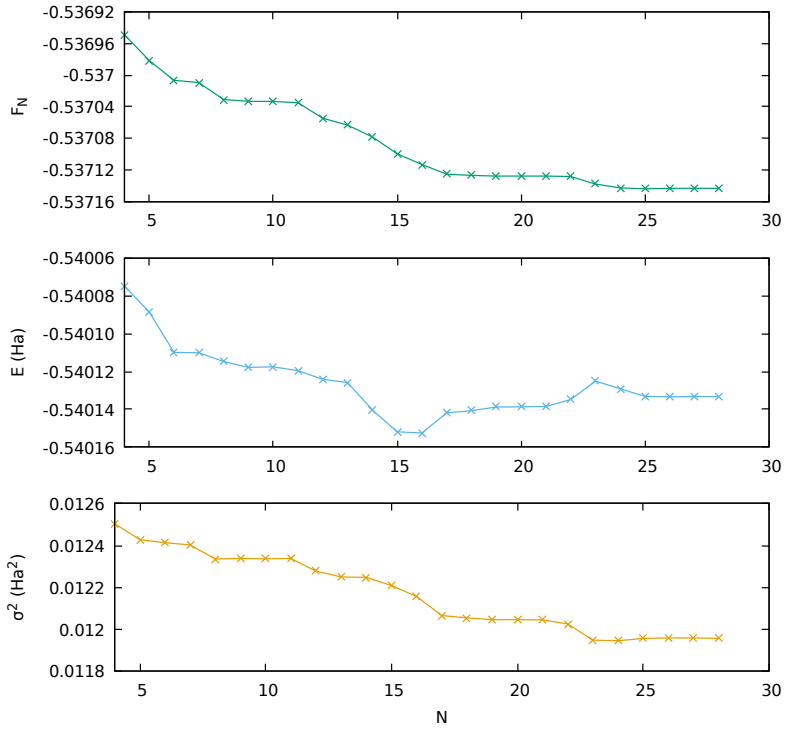

FIGURE 3.12: Example of optimization of a trial wavefunction for the C2c structure at P=250 GPa. Top panel: function $F = E + \gamma\sigma^2$ vs number of optimization steps. Middle panel: electronic energy E. Bottom panel: variance σ_E^2. All quantities are intensive (per proton)

3.3.2.2 Path Integrals setup

We used 32 beads at T=200 K, with a Trotter timestep $\tau = 0.00015625\ K^{-1}$; at T=414 K, we chose 14 beads, with $\tau = 0.00017253\ K^{-1}$. As mentioned in section 2.6, we employ an effective pair potential in order to optimize the number of nuclear beads used in the calculation; the contribution of this effective potential is implemented through the pair action approximation, while the primitive approximation is used for the many-body Born-Oppenheimer potential. The effective pair potential needed during the sampling was obtained by fitting the pair distribution function of liquid high pressure hydrogen through an iterative procedure called Boltzmann inversion [118]. The most relevant part of the pair potential is the divergent hardcore part, which should be quite independent of external thermodynamic conditions. We stress that this does not introduce any additional bias; in the worst scenario, the required imaginary timestep would possibly be smaller than in the optimal case.

To enhance the sampling, the algorithm presented in the previous chapter was slightly modified. While the DFT energy is not accurate enough, the DFT forces can still be used in the Smart Monte Carlo procedure as good guesses to propose the move with a higher final acceptance than the forces coming from the pair action. However, the first prerejection step could hinder the global acceptance, since the first-step acceptance is only linked to the pair action itself and does not "know" about the full many body Born-Oppenheimer energy. To bypass the situation, the probability density $\mathcal{P}$ in eq.

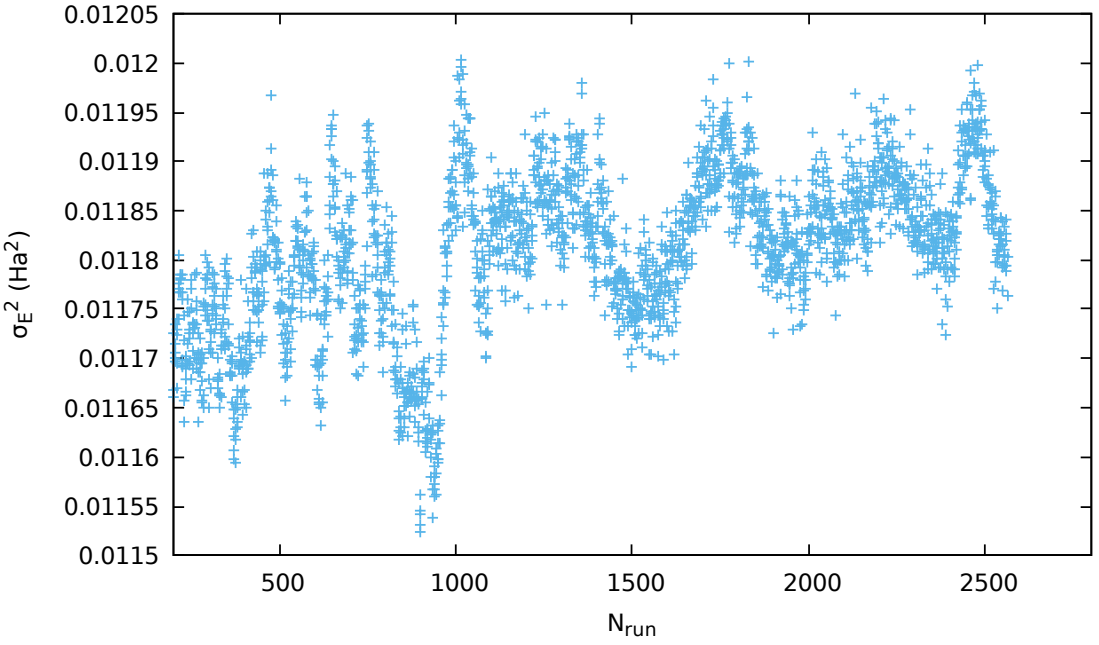

FIGURE 3.13: Evolution of the variance σ_E^2 vs the number of steps N_{run} during a CEIMC run at finite temperature. The maximum amplitude of the fluctuations is of about $2 \cdot 10^{-4}$ $Ha^2/proton$

2.168 is rewritten as

$$\mathcal{P} = P_{pre}(\mathbf{R}_p) e^{-\tau \sum_{p=1}^{P} (E_0^e(\mathbf{R}_p) - E_{DFT}(\mathbf{R}_p))} \tag{3.1}$$

$$P_{pre}(\mathbf{R}_p) = \prod_{p=1}^{P} \exp\left\{ -\frac{M_p(\mathbf{R}_p - \mathbf{R}'_{p+1})^2}{2\tau} \right\} e^{-U_{pair}} e^{-\tau \sum_{p=1}^{P} (E_{DFT}^e(\mathbf{R}_p) - V_{pair}(\mathbf{R}_p))} \tag{3.2}$$

$$U_{pair} = \sum_{p=1}^{P} \sum_{ij} u_2(\mathbf{R}_{ij}^p, \mathbf{R}_{ij}^{p+1}) \tag{3.3}$$

The total probability $\mathcal{P}$ is still the same; if τ is small enough $\sum_{ij} u_2(\mathbf{R}_{ij}^p, \mathbf{R}_{ij}^{p+1}) \approx \tau V_{pair}(\mathbf{R}_p)$ and the prerejection probability is basically the primitive approximation for the DFT energy but including already a reasonably correct quantum behaviour of the action when two particle approach, suitable for the DFT forces. One drawback is that in this way the DFT calculation must be performed at every step, even if later the step will be rejected because of the QMC BO energy difference or because of the noise; however, the computational time required for the DFT calculation is roughly 10% of the total time needed. On the other hand this procedure samples the phase space more efficiently and this leads to smaller autocorrelation times when averaging over the trajectory.

3.4 Results

Dealing with molecular crystals, we are interested in studying the stability of the structure and the orientational order of the molecules. Following [111], we introduce the orientational order parameter (OOP):

$$\hat{O} = \Big[\frac{1}{N}\sum_{i=1}^{N} P_2(\hat{\Omega}_i \cdot \hat{e}_i)\Big]^2 \tag{3.4}$$

where P_2 is the Legendre polynomial of second order, $\hat{\Omega}_i$ is the orientation of molecule i during the simulation while $\hat{e}_i$ is its initial orientation in the static lattice (N is the number of molecules). The OOP is 1 if the molecules stay aligned to their initial orientation while goes to 0 if they re-orient or freely rotate. Another observable of interest is the molecular Lindemann ratio (MLR):

$$\hat{L} = \frac{\sqrt{\Delta^2}}{d}, \Delta^2 = \frac{1}{N}\sum_{i=1}^{N}(\mathbf{r}_i - \mathbf{r}_{i0})^2 \tag{3.5}$$

where d is the nearest neighbour distance in the static lattice, $\mathbf{r}_i$ is the position of the center of mass of molecule i during the simulation and $\mathbf{r}_{i0}$ the position of its center of mass in the static lattice.

Moreover, since we are interested in mixed structures, these observables can be computed for every single layer to better characterize the structures. In the same way, we can define a layer-by-layer pair correlation function $g_{pp}(r)$, when only atoms belonging to the same layer are taken into account, as done in [112]. These layer-by layer $g_{pp}(r)$, being normalized as in the bulk case, do not go to 1 for large r; however, they are significant for distance shorter than the interlayer distance, roughly 2-3 a.u..

3.4.1 C2c, T=200 K

We start our analysis considering the DFT-PIMD simulations starting from the C2c structure, which is the main candidate for phase III. We can qualitatively detect different structural rearrangements in the considered pressure range using the layer-by-layer pair correlation functions reported in fig. 3.14. We recall that each simulation cell has four layers. At the lowest pressure considered, they all exhibit the same radial distribution function; with increasing pressure, a structure with alternating, non-equivalent layers emerge. At the highest pressure, the layers become equivalent again.

A qualitative understanding of what it is going on can be achieved by looking at the nuclear configurations sampled at equilibrium (insets in fig. 3.14). At $r_s = 1.38$, we have four equivalent layers of well defined molecules: they librate around their initial orientation, displaying C2c symmetry. At $r_s = 1.34$ we observe a mixed structure: in blue layers, molecules rotate in-plane, resulting in circular "clouds"; in red layers, molecules form closed rings. Computing the average atomic positions show a slight departure from the hexagonal symmetry, similarly to Pbcn. At $r_s = 1.31$ this mixed structure changes: rotating molecules (blue layer) and a graphenelike, atomic layer (red layer), pointing to an Ibam symmetry. Finally, at $r_s = 1.27$, the system displays a Cmca4 symmetry.

An interesting phenomenon takes place at $r_s = 1.38$ and $r_s = 1.42$, where the system keeps its original symmetry: the orientational order parameter (OOP), which is used to detect changes in the alignment of the molecules with respect to their initial orientation, displays sudden "jumps" along the trajectory. This is reported in the top left panel of fig. 3.15), where the OOP of a single

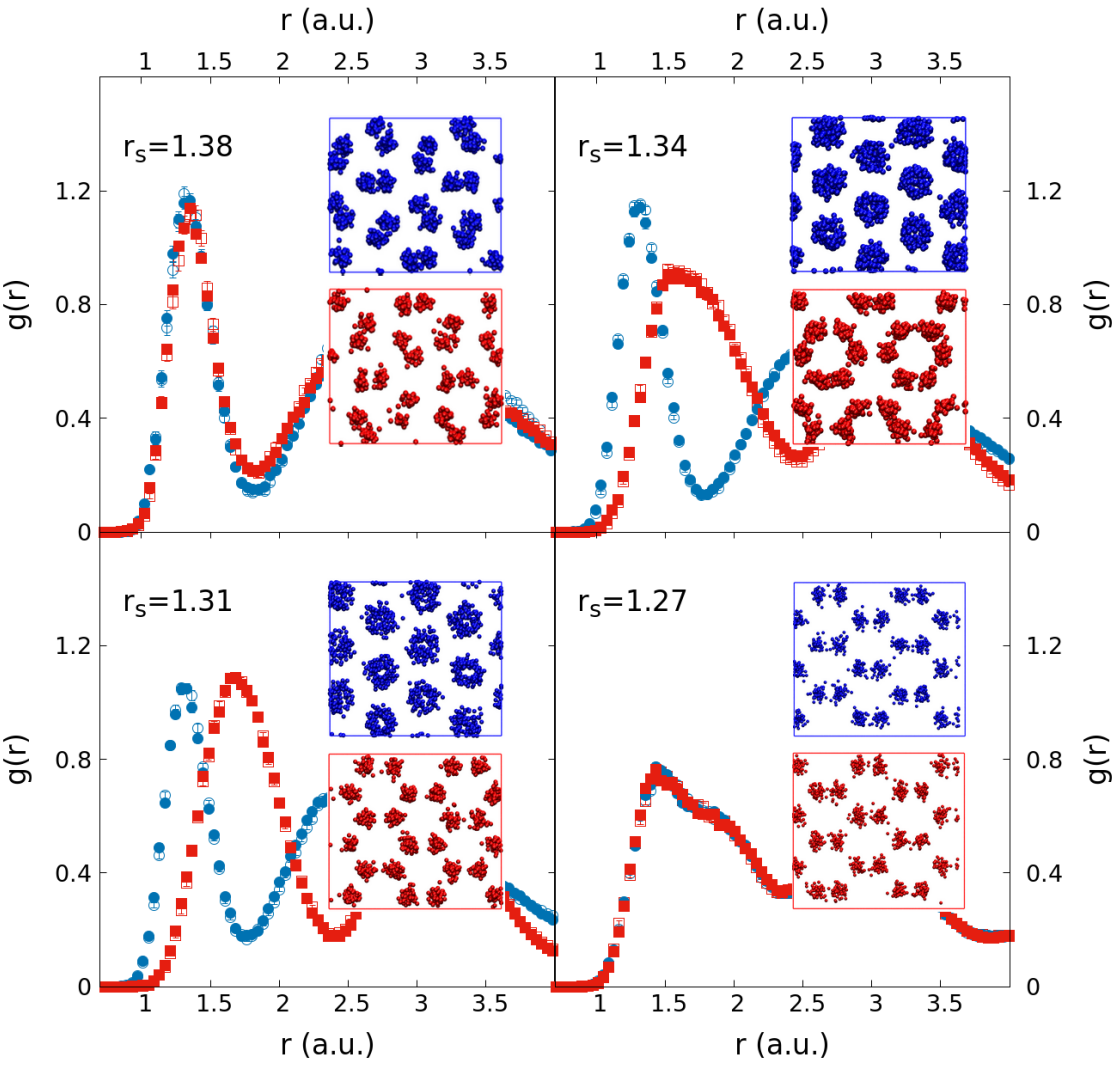

FIGURE 3.14: C2c, DFT-PIMD simulations: Layer by layer pair correlation functions for the four different values of r_s reported in the figure. Each simulation cell contains four different layers: their radial distribution functions are reported with different symbols (open and closed squares and circles). Layers behaving in the same way have the same colour. Insets: several nuclear positions sampled at equilibrium in two consecutive layers

layer at $r_s = 1.38$ is pictured. At the beginning of the trajectory, all the molecules are aligned and the OOP is 1; in ≈ 1000 time steps, the orientational parameter goes to zero, revealing a rearrangement of the molecular axes; after 3000 steps, there is a sudden increase of the parameter, which remains stationary for 4000 steps; finally, the OOP goes back to 0 with another sudden jump. We can separate the trajectory into two parts, according to the values assumed by the OOP, and take the average atomic positions for each distinct segment. The "jumps" of the parameter correspond to a collective rotation of the molecules; in particular, we can identify rings of three molecules (trimers) rotated by the same angle (top right panel of fig. 3.15). These events can be classified as rare, at least on the time scale of our simulations, occurring once or twice per run. It is interesting to notice that these collective rotations can occur independently for the different layers,

as reported in the bottom panel of fig. 3.15: the orientational parameters of layer 1 and 3 follow the same trend, decaying to zero after 5000 time steps; layer 4 goes to zero after the first 1000 steps; layer 2 was described above. Layers with significantly different OOP can cohexist at the same time, showing that the system as a whole can go through configurations where the C2c symmetry may not be preserved. Notice that the layer by layer pair correlation functions are invariant under these rotations, since they preserve the distance among atoms in the same layer.

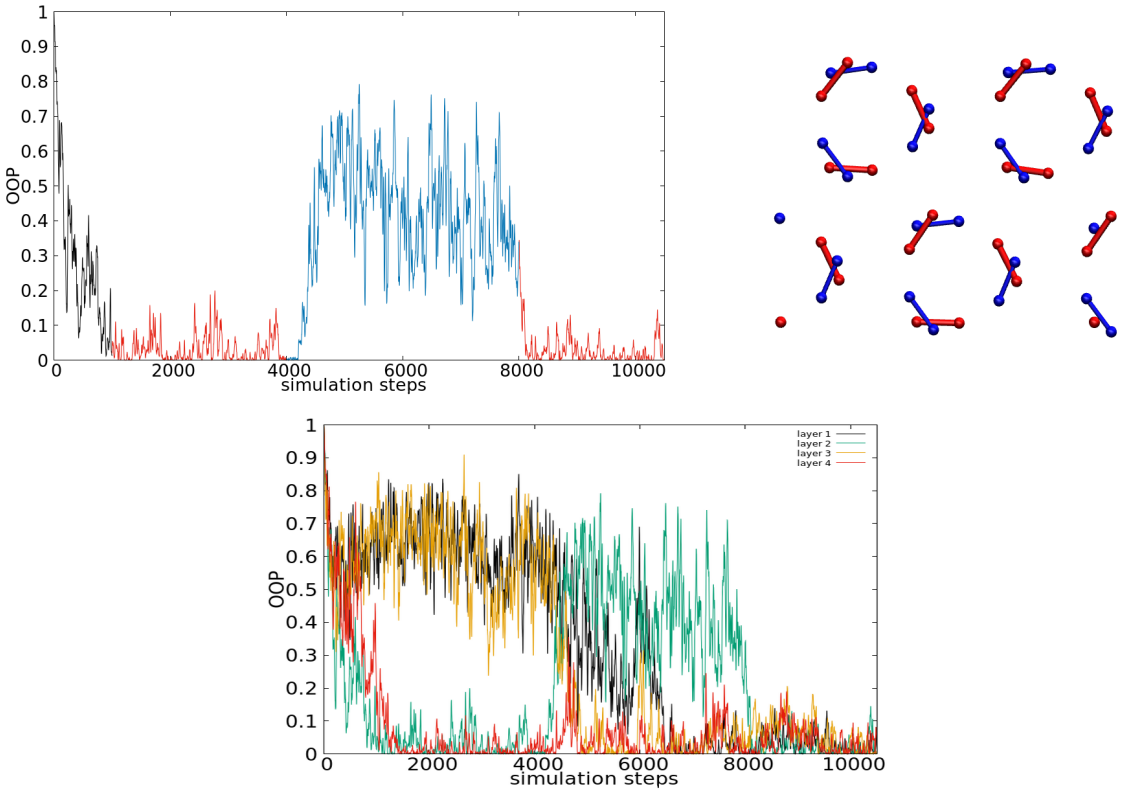

FIGURE 3.15: Top left panel: orientational order parameter (OOP) along the whole PIMD-DFT trajectory for a single layer of the system starting from C2c symmetry at $r_s = 1.38$ and T=200 K. Segments of the trajectory which display a similar value of the OOP are coloured in red ($OOP \approx 0$) or blue ($OOP \approx 0.5$). Top right panel: average positions of the atoms in the layer, obtained considering separated segments of the trajectory with different colours in the left panel. Blue (red) atoms are the results of averaging over the corresponding blue (red) portion of the trajectory. Sticks are pictured for the sake of clarity. Bottom panel: orientational order parameter (OOP) along the whole PIMD-DFT trajectory for all the layers of the system starting from C2c symmetry at $r_s = 1.38$ and T=200 K.

When density is increased, hexagonal layers appear: a natural question is whether atoms in these layers bond into molecules or not. To discuss the molecular nature of the hexagonal layers at $r_s = 1.31$, we computed the electronic charge density, assuming that the existence of a molecular bond is deeply connected to a local maximum of the charge density between two protons. As we can see in fig. 3.16, the charge density for one protonic configuration suggests the existence of both molecules and isolated atoms: during the simulation, the atomic motion results in a fast bonding and rebonding activity among different atoms. This leads to the averaged charge density in the right panel, which display the hexagonal symmetry already seen when considering several snapshots of the protonic positions.

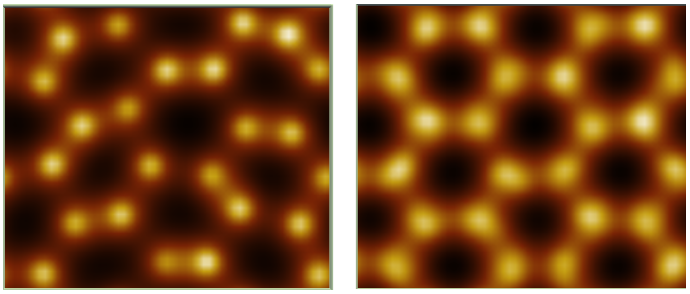

FIGURE 3.16: Electronic charge densities for an hexagonal layer at $r_s = 1.31$. Left panel: charge density of a single nuclear configuration. Right panel: charge density averaged over 16 different nuclear configurations

Since DFT calculations are relatively affordable, we could run other simulations starting from the Pbcn and the Cmca4 structure at different pressures; the results are summarized in table 3.2. The stability ranges of the different phases depend on the initial structure: this was to be expected, since our simulations are performed at constant volume and the system is constrained by the initial geometry of the supercell. Nevertheless, we can find a common chain of transitions while the volume decreases: C2c → Pbcn → Ibam → Cmca4.

TABLE 3.2: Table summarizing the final structures reached depending on the initial conditions (initial structures and r_s).

Starting Structure \ r_s	1.42	1.38	1.34	1.31	1.29	1.27	1.25
C2c	C2c	C2c	Pbcn	Ibam	Ibam	Cmca4	Cmca4
Cmca4	C2c	Pbcn	Ibam	Ibam	Cmca4	Cmca4	
Pbcn	C2c	Pbcn	Pbcn	Ibam	Ibam	Ibam	

We performed CEIMC runs starting from the C2c structure at $r_s = 1.38, 1.31, 1.27, 1.23$ ($200 < P < 550$ GPa); the results of the same analysis performed for DFT-PIMD are reported in fig. 3.17.

We see again different behaviours for different layers at $r_s = 1.31$ and $r_s = 1.23$. In the first case we can distinguish stronger and softer molecular layers, according to the depth of minimum between the molecular peak and the rest of the radial distribution function. At $r_s = 1.23$, instead, some layers have a single broad peak around 1.6 a.u. while the others retain two different peaks. A visual inspection of the average charge density shows that every layer is molecular; a direct inspection at the atomic configurations does not show a clear hexagonal pattern, but a better understanding of the symmetries is difficult to achieve, at variance with the DFT case.

Nevertheless, we can extract some useful information even from the insets of fig. 3.17: clouds associated to individual atoms can be spotted. This means that, when molecules exists, they have a reduced rotational activity, similar to what happens in the DFT simulations at low density ($r_s = 1.38$ and $r_s = 1.42$). During the CEIMC simulations, we do not observe the abrupt jumps in the orientational order parameter, which were present in the DFT case. In fact, the OOP in the CEIMC simulations reach stationary values consistent with the high OOP values found during the PIMD DFT trajectories (compare the CEIMC OOP reported in the top right panel of fig. 3.18 with

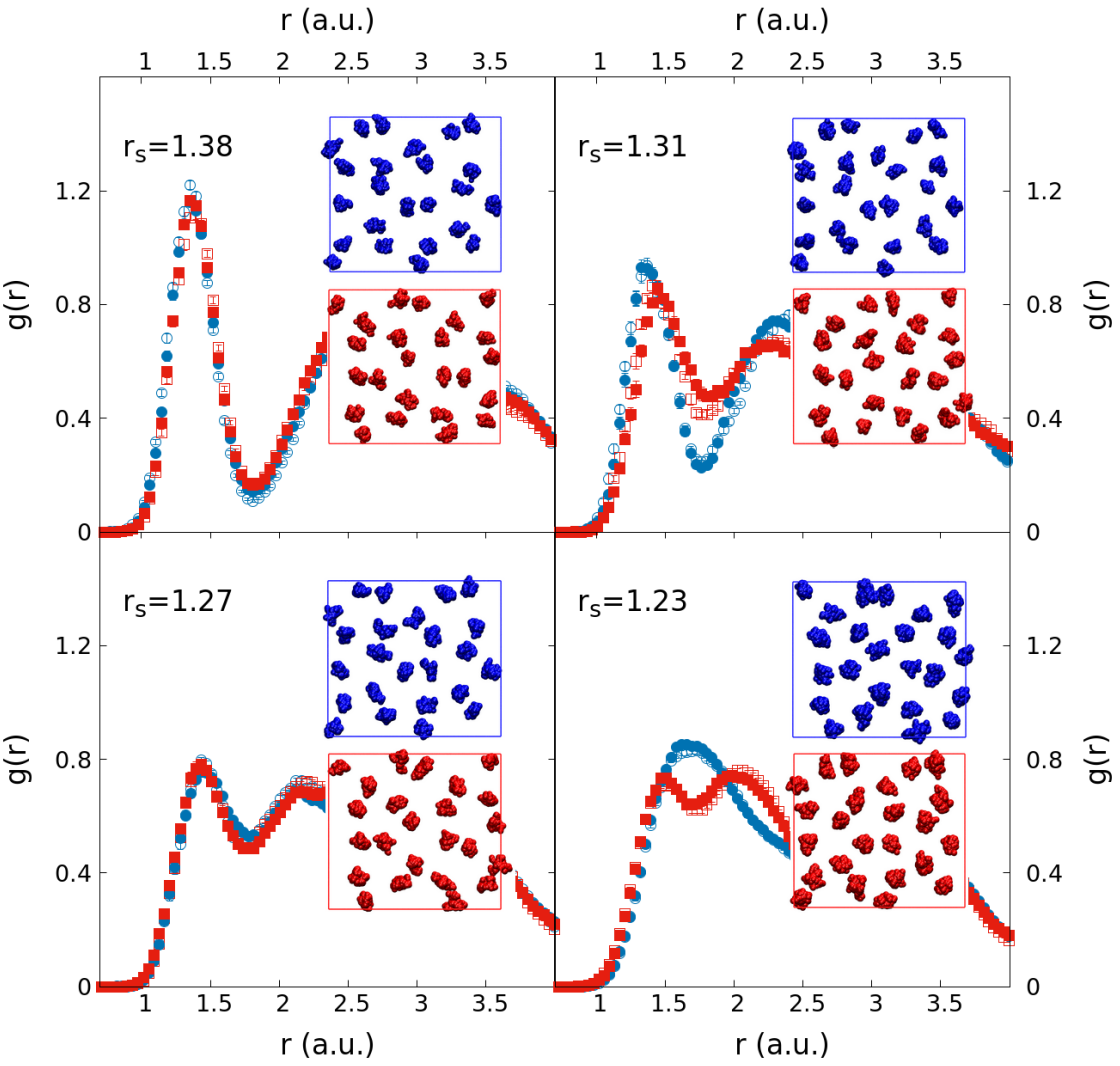

FIGURE 3.17: C2c,CEIMC simulations: Layer by layer pair correlation functions, for four different values of r_s, reported in the figure. Insets: selected nuclear positions sampled at equilibrium in two consecutive layers

the OOPs in fig. 3.15). The absence of these rotations is also reflected in the different MLR: the DFT MLR at $r_s = 1.38$ and $r_s = 1.42$ is bigger than the CEIMC one, since the molecular centers move when the trimers rotate. On the other hand, the two pair distribution functions match each other rather well (fig. 3.19). A direct comparison at higher pressures is biased by the structural transitions: for example, the bond length is very sensitive to the changes of phase (see fig. 3.18). In fact, we can see a first discontinuity between $r_s = 1.38$ and $r_s = 1.34$, when the the first transition happens: molecules in the mixed phases have a smaller bond length. Than, a second jump happens between $r_s = 1.29$ and $r_s = 1.27$, where Cmca4 becomes the stable phase with a considerably larger bond length.

The CEIMC results seem to confirm the evolution of the structure towards phases with non-equivalent layers at high pressures, even if we cannot discern proper structural transitions and

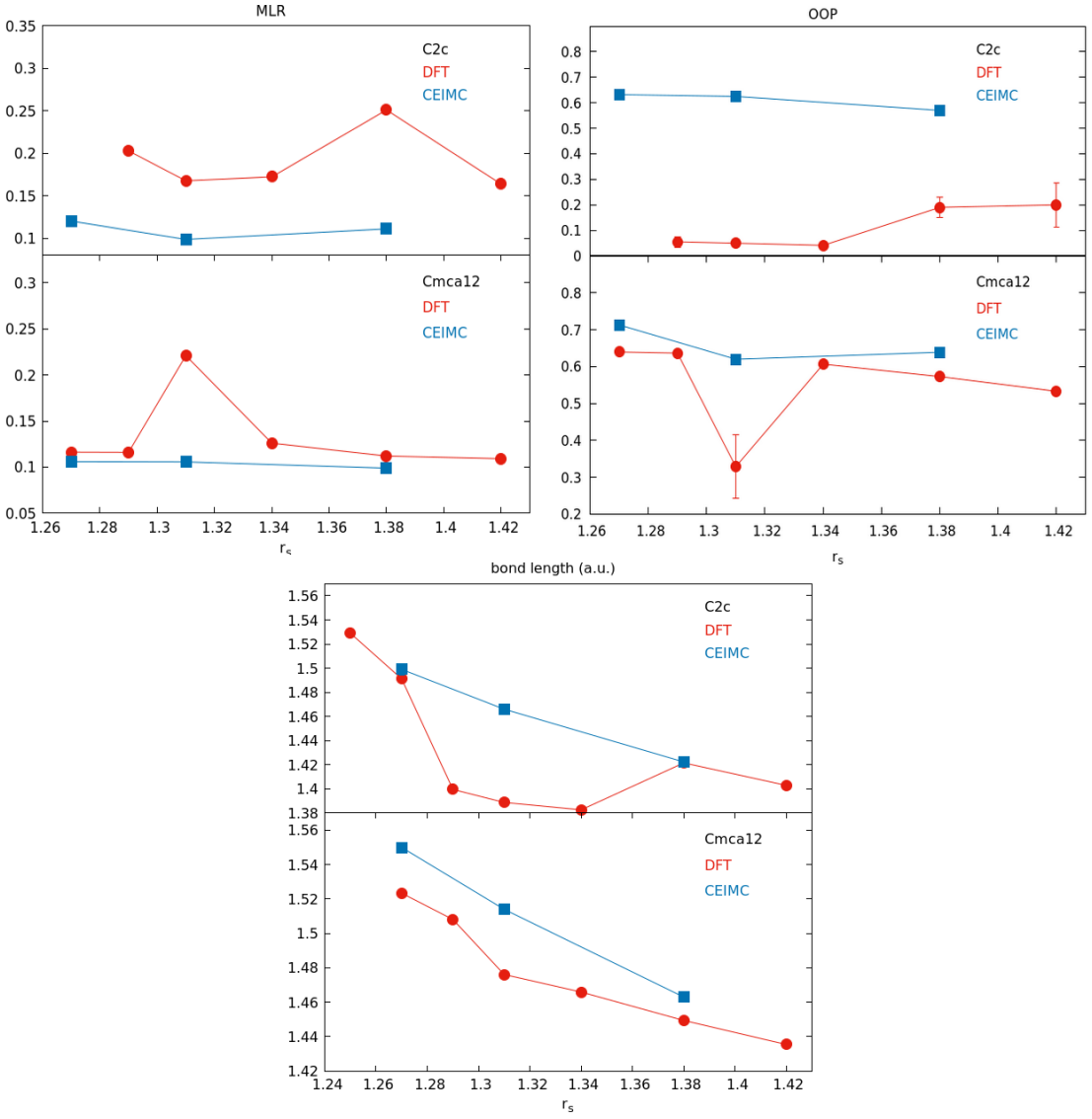

FIGURE 3.18: Several structural, molecule-related observables for simulations starting from the C2c and the Cmca12 structures. Top left panel: molecular Lindemann ratio (MLR). Top right panel: orientational order parameter (OOP). Bottom panel: length of the molecular bond (bond length). Since for C2c there are transitions to mixed structures with atomic planes, these quantities are computed only in the molecular layers.

all the layers have a molecular nature. Since we are working at constant volume and the CEIMC simulations are computationally demanding, we cannot rule out the possibility that the phases considered are metastable; even so, the difference between the pair distribution functions of the layers at $r_s = 1.31$ and $r_s = 1.23$ is itself an indication of departing from the C2c symmetry.

The differences in the OOP and in the MLR between the DFT-PIMD and the CEIMC simulations at low densities can be attributed to the rare events involving the rotation of trimers; at higher densities, mixed structures with rotating molecules make their appearance in DFT-PIMD while CEIMC simulations do not display rotations at all. These considerations suggest that the actual energy

barriers preventing molecular rotations and movements of the molecular center is underestimated by PIMD-DFT for C2c.

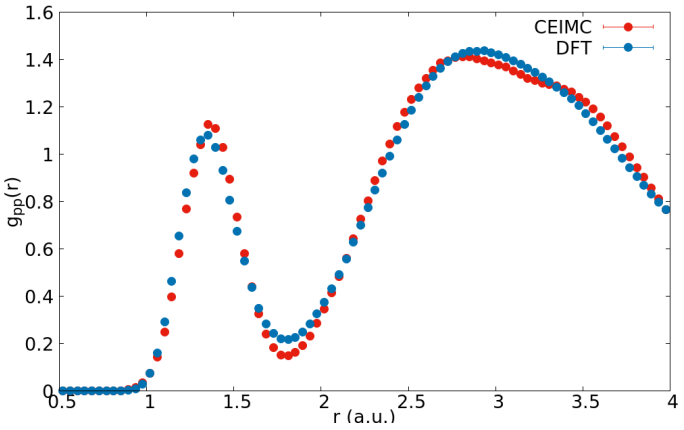

FIGURE 3.19: Comparison of the CEIMC and DFT pair correlation functions for systems starting from the C2c structure at $r_s = 1.38$

3.4.2 Cmca12 at T=200 K

Systems starting from the Cmca12 structure do not display transitions to structures with different layers; in this case we can readily compare the PIMD and CEIMC results (fig. 3.20). While $r_s = 1.38$ and $r_s = 1.27$ are in good agreement, at $r_s = 1.31$ the two pair distribution functions show a noticeable difference in the first minimum and the second maximum. This discrepancy is the result of a structural rearrangement in the DFT system, not observed with QMC, as can be appreciated by looking at the MLR and the OOP parameters (see figs. 3.18), respectively higher and lower than the values at the other pressures. The transition happens after a long period of metastability of the Cmca12: it is possible that such a transition would happen also at higher pressures, but we did not see it due to the limited length of the PIMD simulations. Conversely, CEIMC runs do not show any sign of structural rearrangement. Whether this is a true stability condition or just the result of a too short sampling remains to be proved. As a matter of fact, the observation of such dynamical stability indicates that the energy barriers separating Cmca12 from other structures are rather large. Curiously, in this phase, layers remain equivalent but in the same layer we have both molecules forming rings and molecules rotating in the plane (see fig. 3.21).

Focusing on the remaining r_s (1.38 and 1.27), where the Cmca12 symmetry persists, we see that the MLR, OOP and bond length (figs. 3.18) are comparable both for PIMD and CEIMC; in particular, the OOP is fairly high, indicating a reduced rotational activity. The exception is, as reported above, $r_s = 1.31$ where some of the molecules rotates in the plane. These considerations may suggest that DFT (at least, using the vdW-DF functional) reproduces well the properties of the Cmca12 symmetry while it lowers the rotational barriers of the molecules in the C2c phase, making transitions to mixed structures more likely.

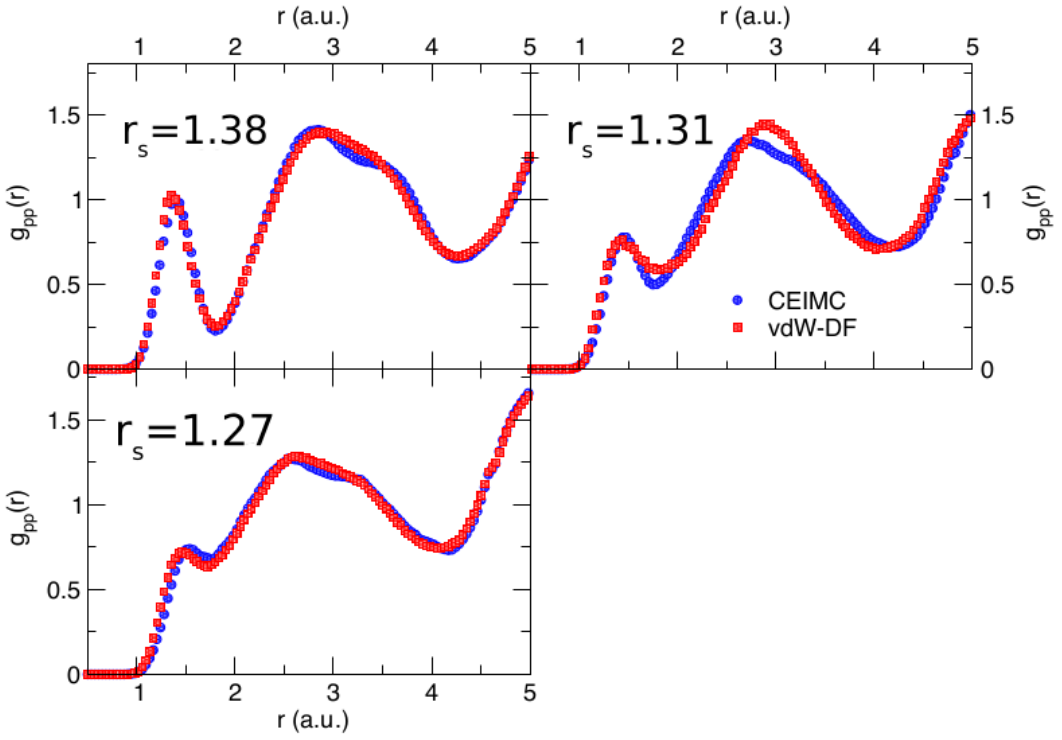

FIGURE 3.20: PIMD and CEIMC radial distribution functions for systems starting from the Cmca12 structure at four different values of r_s

3.4.3 Electronic properties

One longstanding issue is whether solid molecular hydrogen undergoes metallization when pressure is increased or whether metallization requires a transition to an atomic phase. We can see how C2c and Cmca12 behave in this regard by studying their conductivity. For PIMD, conductivities can be computed within DFT through the Kubo-Greenwood formula reported in eq. A.62: in our case we select 16 protonic configurations sampled during the simulation and compute an average conductivity using the HSE functional, which generally provides better band gaps. A detailed discussion on how to extrapolate the dc value $\omega = 0$ of the conductivity is presented in section 4.4.1, where optical properties are treated in greater detail. Rigorous calculations of the conductivity involve excited states: there is no affordable and easy scheme to compute conductivities using Quantum Monte Carlo methods. Therefore, for CEIMC, we use the sampled protonic configurations and perform the same DFT-conductivity computation on top of them. For layered crystals, we report both longitudinal and transverse components of the conductivity tensor, with respect to the lattice layers. An example of longitudinal conductivity for a single nuclear configuration sampled during the CEIMC runs starting from the C2c structure is showed in fig. 3.22 (right panel), with the corresponding electronic density of states obtained through DFT. At $r_s = 1.31$ the band gap is closed and the system is formally metallic; however, a "depression" remains at the Fermi level, corresponding to a small value of the dc conductivity. Increasing the density, the Fermi level is filled, and the dc conductivity increases. Qualitatively, the behaviour of the system is similar both for PIMD and CEIMC, C2c and Cmca12: the systems become metallic for $r_s \leq 1.31$, corresponding to a pressure P=337 GPa (see fig. 3.23). The relatively small values of the conductivity suggests that

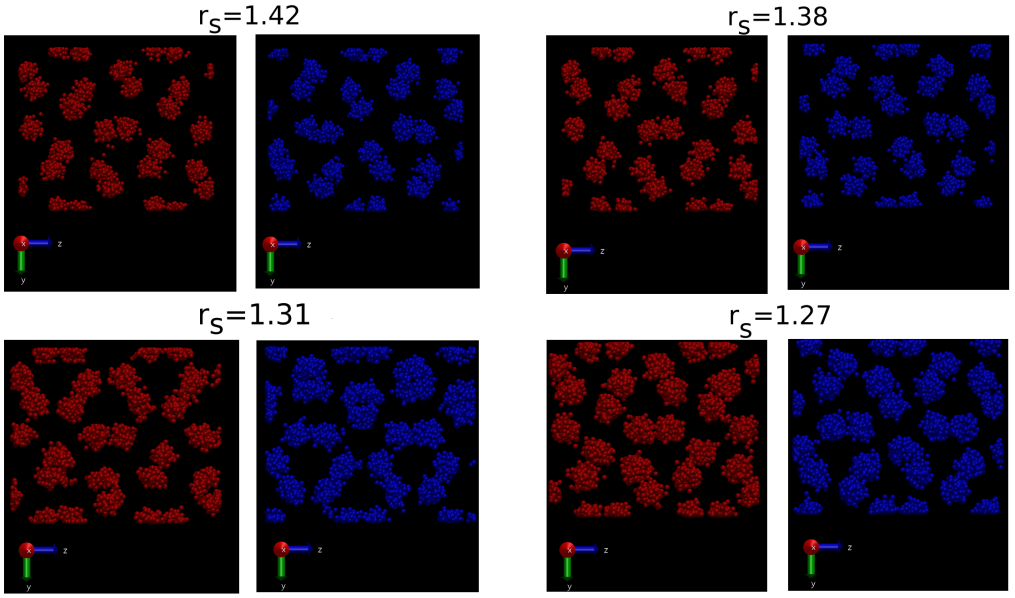

FIGURE 3.21: PIMD sampled atomic configuration for systems starting from the Cmca12 structure at the same values of r_s reported in fig.3.20

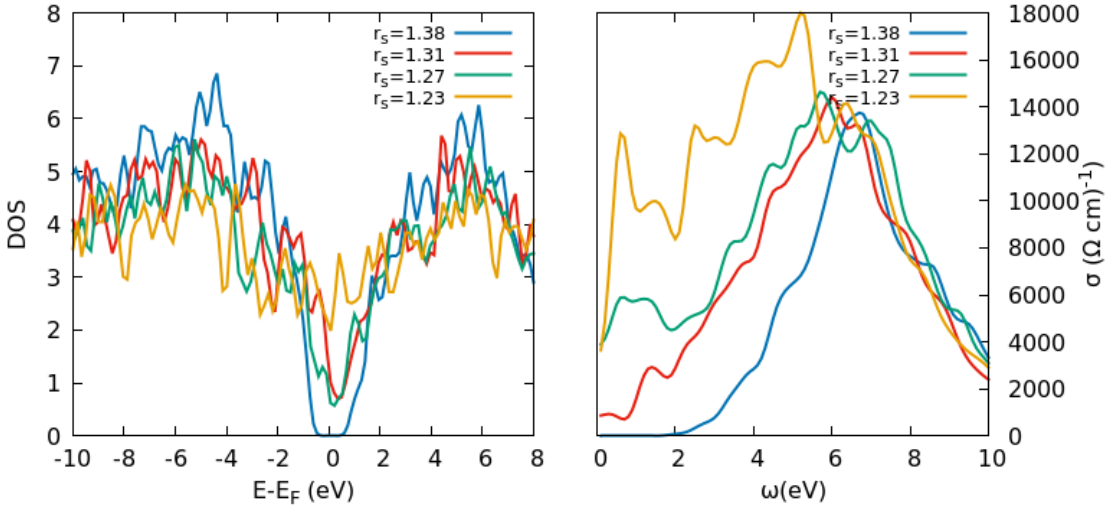

FIGURE 3.22: Left panel: electronic density of states averaged over 16 different nuclear configuration sampled during CEIMC simulations starting from the C2c structure. The zero of the x-axis corresponds to the Fermi energy. Right panel: the corresponding longitudinal conductivity $\sigma(\omega)$

these structures are semimetallic in this range of densities. For CEIMC simulations the conductivity of the Cmca12 structure seems systematically higher than the C2c one; at the same time, the CEIMC conductivity of C2c is lower than the corresponding PIMD values. It should be noticed that a recent work by Eremets [18] claims to observe experimentally the onset of metallic behaviour around 350 GPa, close to the value of the pressure obtained by the simulations at $r_s = 1.31$ (337 GPa).

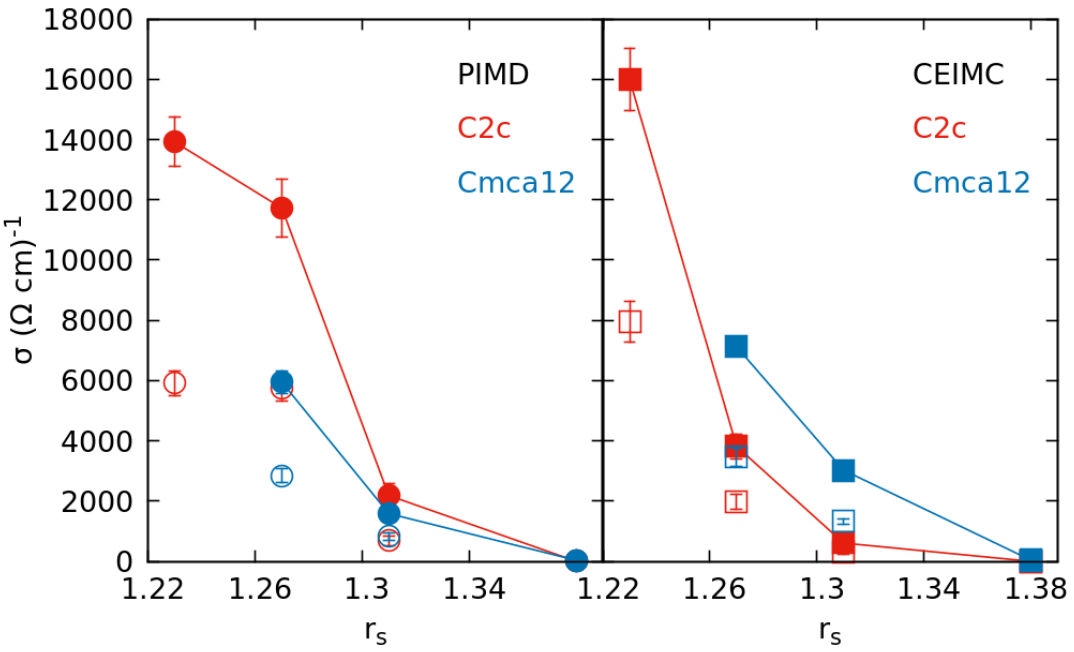

FIGURE 3.23: Electrical conductivities for C2c and Cmca12 structures obtained from PIMD (left panel) and CEIMC (right panel) simulations. For crystals, we resolved the conductivities into a longitudinal part, parallel to the layers (full symbols), and a transverse one (empty symbols). The symbols corresponding to the longitudinal conductivities are connected by a solid line to guide the eye.

3.4.4 Pc48 at T=414 K

We ran some PIMD and CEIMC simulations of the most accredited candidate for phase IV, Pc48, at T=414 K and $r_s = 1.38, 1.34, 1.31$ ($250 \leq P \leq 350$ GPa).

Pc48 is yet another mixed structure: layer by layer pair correlation functions can be used to resolve differences among layers, as in the C2c case. In fig. 3.24 we directly compare the PIMD and CEIMC pair correlation functions: they show a good agreement, even if some of the CEIMC data are evidently affected by noise. In both cases, the presence of a well defined molecular peak determines the strong molecular character of the layer; in weak molecular layers, on the hand, the molecular peak appears broad and cannot be easily isolated from the rest of the radial distribution function. While the strong molecular layers do not qualitatively change when increasing density, the molecular peak in the other layers gradually moves to higher distances. The blue insets of the DFT simulations show a strong rotational activity of the molecules in the strongly bonded layers; this is not so evident in the blue CEIMC insets, which seem to display a significant rotational activity only at higher densities. In both cases, the orientational order parameter is small (see fig. 3.6). However, this is only an indication of the alignment of the molecules with respect to their initial orientation; their axes could also rearrange themselves in a different static configuration. This seems unlikely: it is hard to discern any clear pattern. Moreover, molecules located at the same lattice site change orientation when the density changes: this should rule out a possible common oriented phase in the density range considered. This discrepancy may be caused by a limited sampling of the rotational

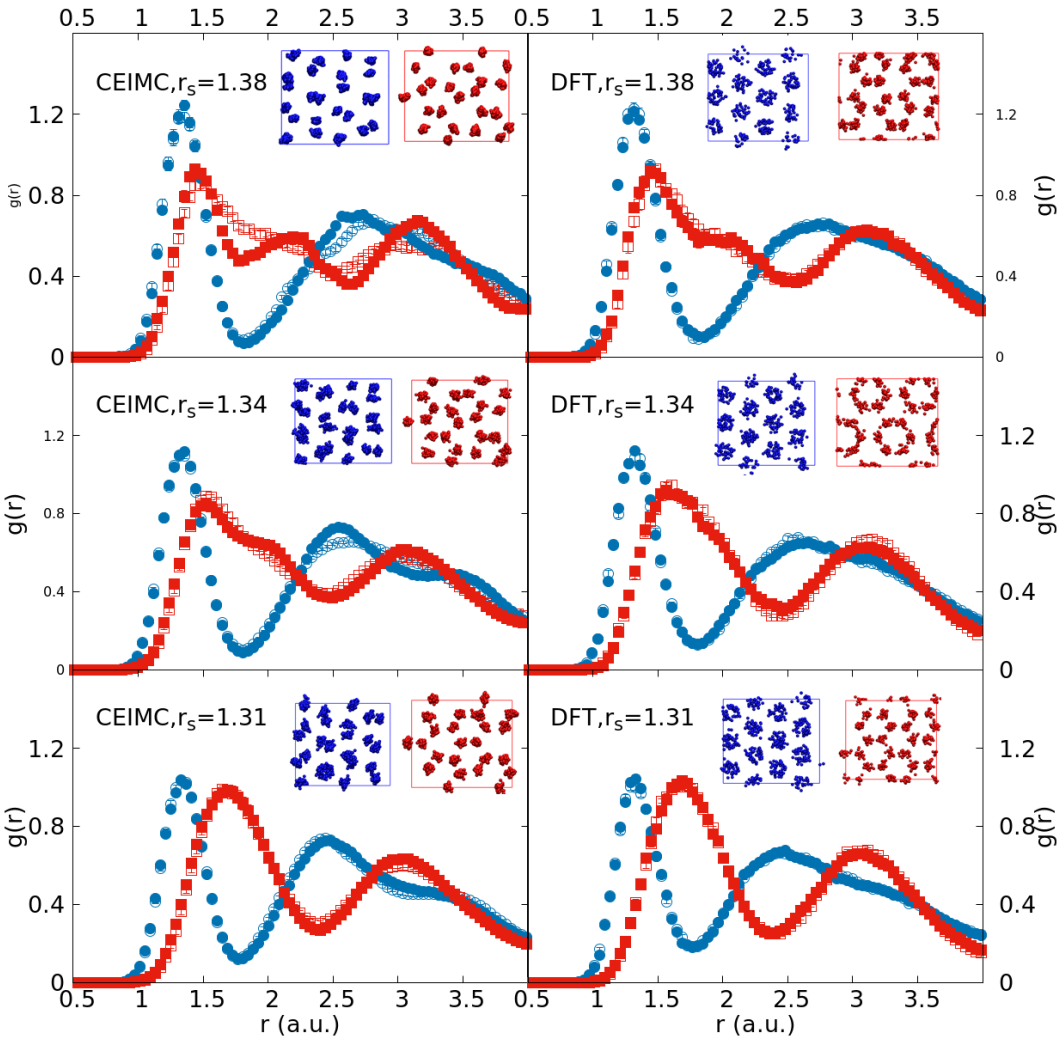

FIGURE 3.24: Pc48, Layer by layer pair correlation functions for DFT-PIMD and CEIMC simulations at the reported values of r_s (corresponding to the range of pressures $250 \leq P \leq 350$ GPa). The four different layers are represented by full and open symbols; layers with strongly bonded molecules are associated to the blue curves while weakly bonded molecular layers are red. Insets: nuclear positions sampled at equilibrium in two consecutive layers

phase space of the molecules and be an indication that longer runs are required to improve the statistics.

Weakly bonded layers show a tendency to rearrange in a hexagonal pattern when density is increased, reducing the distortion imposed by the initial configuration: this is true for both CEIMC and DFT-PIMD simulations. In general, the DFT-PIMD simulations display a higher degree of order: for example, well separated rings can be detected at $r_s = 1.34$. A closer inspection of the DFT trajectories reveals processes when atoms belonging to the same ring perform a collective rotation: evidence of this process is reported in fig. 3.26. These rotations are rare: we could observe 1-2 events in ≈ 2 ps, the length of an entire DFT-PIMD simulation. No rotations were detected in the CEIMC simulations: this was expected due to the computational cost of the method, which

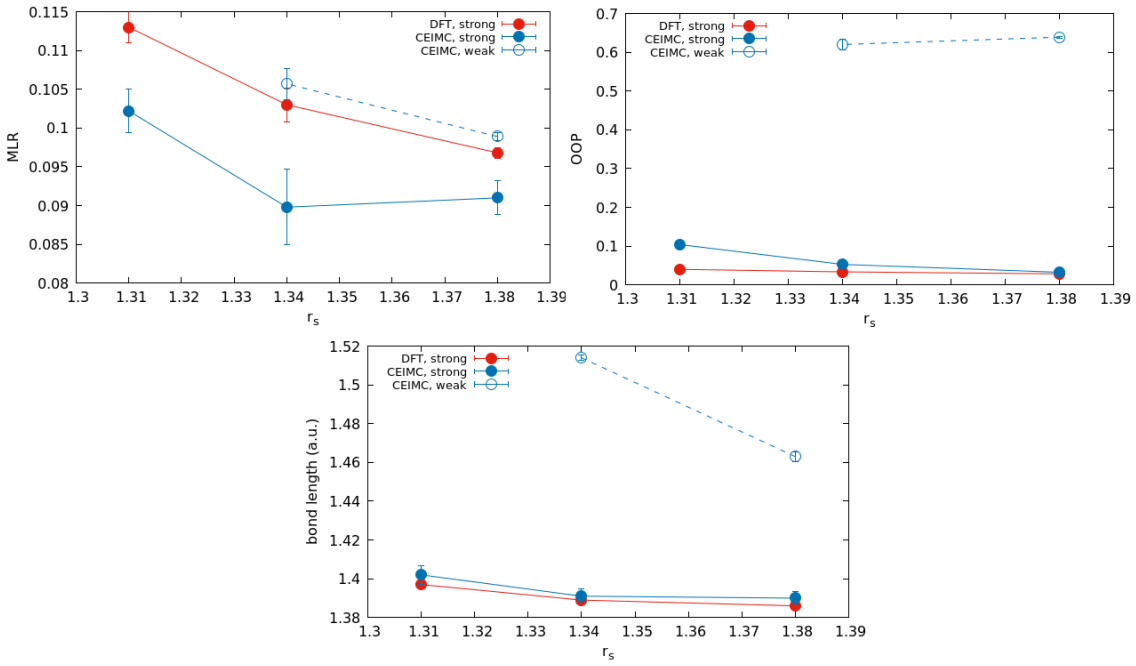

FIGURE 3.25: Pc48: structural properties obtained from CEIMC and DFT-PIMD simulations: molecular Lindemann ratio (MLR), orientational order parameter (OOP) and molecular bond length for strongly and weakly bonded molecular layers ("strong" and "weak", respectively). Only CEIMC weakly bonded molecular layers are reported, as explained in the text.

inevitably lowers the sampling efficiency and makes the detection of such rare events a task beyond our current scope.

To get a better picture of what happens in these layers for CEIMC simulations, we computed the electronic charge density for 16 representative CEIMC sampled along the trajectory and we averaged over them, obtaining the results in fig. 3.27. We see that the rings made up of three molecules get closer as the density is increased, resulting in an increased overlap of charge among atoms in the same rings. Eventually, it is difficult to distinguish atom belonging to a specific molecule: the right panel of fig. 3.27 shows well isolated molecules, but atoms without any clear molecular partner are present as well. This is an effect of the nuclear motion during the trajectory, which is amplified in DFT simulations; for these reasons, structural features of molecules are reported only for CEIMC weak layers at $r_s = 1.38$ and $r_s = 1.34$ in fig. 3.6.

Finally, we consider the electrical conductivity. The qualitative picture is the same as for the other structures considered: the band gap shrinks and, at some critical value of r_s, becomes zero; the electronic density of states has a depression around the Fermi energy that is filled when density is increased. The results are the conductivities reported in fig. 3.28: using DFT-PIMD, the system becomes metallic at $r_s = 1.34$ while with CEIMC the metallic state is found only at $r_s = 1.31$. Moreover, the conductivity is larger in the DFT case, probably because the higher nuclear mobility in the weakly bonded molecular layers favours the metallic state. In both cases, however, the conductivity is poor when compared with standard metals.

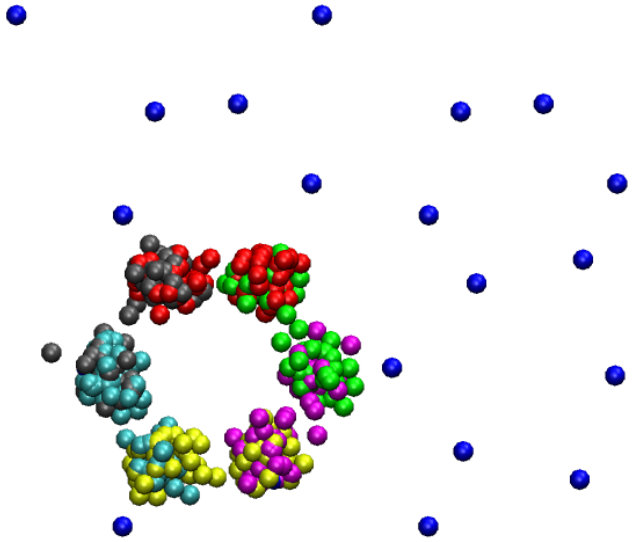

FIGURE 3.26: Picture illustrating a rotation of one ring of six atoms. The blue spheres represent the initial positions of the atoms within the weakly-bounded layer at $r_s = 1.31$. Several nuclear configurations visited along the trajectory by the nuclei belonging to the bottom left ring are pictured; each atom is associated to a different colour. It is apparent that each atom hopped between two lattice sites during the simulation; an investigation of the trajectory shows that the hoppings of the single atoms take place at the same time, generating a rotation of the whole ring.

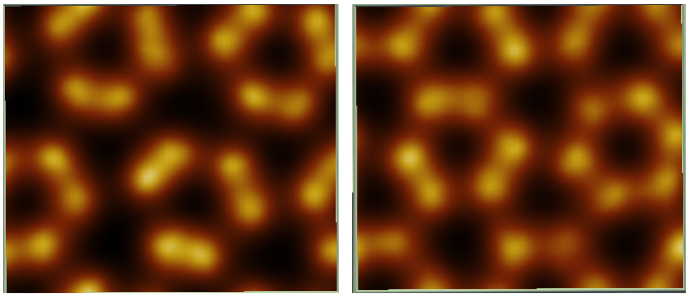

FIGURE 3.27: Pc48, electronic density of charge for the weakly bonded layers for CEIMC simulations. Left panel: $r_s = 1.38$. Right panel: $r_s = 1.31$. Average over 16 different protonic configurations

3.4.5 Discussion

From a theoretical standpoint, we can compare our findings both with previous dynamical DFT simulations and static QMC calculations mentioned at the beginning. Most of the dynamical simulations were performed at higher temperatures (except for ref. [111]), showing qualitative features similar to our PIMD results: a stable C2c at lower densities; a first transition to the Ibam structure when increasing pressure; a new transition to Cmca-4 at higher pressures [106–109]. These articles mainly focused on the properties of the mixed structures, especially on their hexagonal layers, finding contradicting results. However, as pointed out in [111] and [112], the energy landscape of high pressure hydrogen is not well represented by semilocal DFT functionals and nuclear quantum effects enhance the difference, while MD with classical protons could give rise to a cancellation of errors. In our case, we found that results from vdW-DF DFT depend on the initial symmetry of

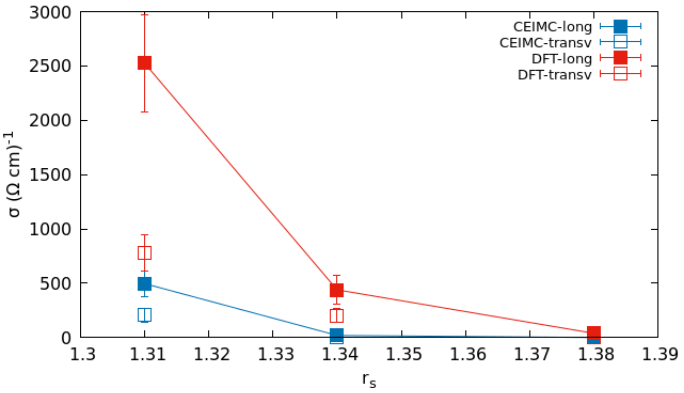

FIGURE 3.28: Longitudinal and transverse static conductivity for the Pc48 structure obtained from CEIMC and DFT-PIMD simulations

the crystal at least for the quantities considered in this work. For Cmca12, vdW-PIMD simulations give a picture consistent with CEIMC. For C2c, instead, the molecular dissociation in the hexagonal layers seems heavily overestimated. Ref. [112] suggests how energy barriers leading to molecular dissociation are probably underestimated by DFT; our runs confirm that even if non-equivalent layers appear, molecules do not dissociate at T=200 K. We see first signs of dissociation only when considering Pc48 at T=414 K. In DFT-PIMD simulations, protons in the weakly bonded layers tend to form rings, which become similar to a hexagonal network at the highest density considered; with CEIMC, at least some of the molecules in the weakly bonded layer are dissociated $r_s = 1.31$, as indicated by the right panel of fig.3.27. As discussed above, our simulations were ≈ 2 ps long, too short to see any diffusion event linked to the rotations of the rings, as pointed out by Liu [109]. It is possible that protonic diffusion results as a product of several rotations of different rings: this process is favoured by high density, when rings "merge" in a hexagonal network, as we observed at $r_s = 1.31$. We did not see different kinds of hexagonal layers, as proposed by Magdau [108].

In DFT simulations, we observed rare events also in the pure molecular phase at lower densities: this leads to sensible differences for the OOP and the MLR between CEIMC and DFT. While the same considerations about the length of the CEIMC simulations can be made, this may be another indication that energy barriers (in this case, involving rotations) are underestimated by DFT. In ref. [111] the same quantity is computed for C2c in similar thermodynamic conditions, employing both PIMD and MD with PBE. Both PIMD and MD give a low value of the OOP, showing that in this case nuclear quantum effects are of secondary importance and the main discrepancy probably comes from the DFT energetics.

Some discrepancies between DFT-PIMD and CEIMC are found at higher temperature as well: the rotational character of the strongly bonded molecules is different; the protonic motion in the weakly bonded layer is enhanced in the DFT simulations. We are still investigating if these differences could be attributed to a non exhaustive sampling in some of the CEIMC simulations or if the disagreement is at a more fundamental level.

3.5 Conclusions

Carefully studying solid hydrogen at high pressure requires the inclusion of nuclear quantum effects and the computation of accurate electronic energies. While nuclear quantum effects can be taken into account at finite temperature with Path Integrals Molecular Dynamics, DFT is usually used to obtain electronic energies. Unfortunately, the uncontrolled approximation introduced by the exchange-correlation functional can make DFT energies not accurate enough for solid hydrogen. To address both problems, we employed the CEIMC method, which is a combination of the Path Integral formalism (to account for quantum nuclei) and of Variational Monte Carlo (to obtain accurate electronic energies). While being computationally more expensive than DFT used in conjunction with Path Integrals, simulations performed with the CEIMC method can be used as a benchmark for DFT-PIMD; in particular, we performed DFT-PIMD and CEIMC simulations of selected structures of interest for solid hydrogen at high pressure (P>200 GPa) and temperature T=200 and 414 K, characterizing their structural and electronic properties. The comparison between DFT-PIMD and CEIMC at finite temperature shows how the stability of C2c is severely underestimated by DFT, in qualitative agreement with the results reported in [116] [104]. This could be linked to the vibrational and rotational activity of the molecules, which seems to be particularly enhanced in the C2c case: energy barriers may be lowered by DFT (as is suggested in ref. [112]), activating molecular rotations and increasing the configurational phase space visited by the protons, favouring structural rearrangements. A remarkable finding is the complete difference from this point of view between C2c and Cmca12 at the DFT level, with Cmca12 molecules frozen in their orientations during the whole trajectory. Both structures exhibit a semimetallic behaviour starting from 350 GPa.

The rotational activity can be observed in CEIMC simulations at higher temperature for Pc48: it is reasonable to think that the overall agreement between DFT-PIMD and CEIMC hints at the possibility that vdW-DF (or, generally, DFT) becomes a better and better approximation of the physical system when temperature increases and the nuclear quantum effects become less and less relevant.

Chapter 4

Liquid liquid phase transition

In this chapter we will apply the CEIMC method to study liquid hydrogen. In particular, an interesting open problem is the metallization of liquid hydrogen and the associated phase transition. As we saw in the previous chapter, solid metallic hydrogen still remains an open problem, despite some claims of the detection of metallic behaviour. Nevertheless, metallic hydrogen was unequivocally detected by Weir et al. [6] in the liquid phase at pressures of hundreds of GPa and temperatures of thousands of Kelvins using shock wave compression experiments. While metallic state itself was observed, that region of the phase diagram is not completely characterized yet. More importantly, the nature of the insulator-metal transition itself is object of debate: first-order or continuous? Which role does molecular dissociation play? In the region of interest, liquid hydrogen displays a rich optical activity. Performing experiments at such extreme conditions proves to be challenging, though: in chapter 1 we showed how experimental data are generally plagued by large error bars and how their interpretation is not straightforward.

We will start discussing previous works on the subject, presenting the current state of this field; then, we will describe how the CEIMC method and DFT-PIMD are employed to study dense liquid hydrogen, inserting them in the current context of the research. In particular, we will focus on characterizing the system under investigation through optical properties, which will constitute the our main results. Some of the results presented in this chapter were published in ref. [46]

4.1 Previous works

High pressure liquid hydrogen has been an active research field for at least twenty years: this section is by no means a complete review of the numerous publications concerning this system. Before the advent of feasible Ab Initio simulations, dense hydrogen at high temperatures has been studied by modeling the free energy of the system (chemical models). Typically, this procedure was based on writing the free energy as the sum of relevant terms, which could be evaluated in different ways: analytical approximations, equations of state obtained from effective interparticle potentials [120] [121]. These first studies considered the possibility of a first-order phase transition between two different states of the fluid, persisting at over 10000 K: however, this transition was

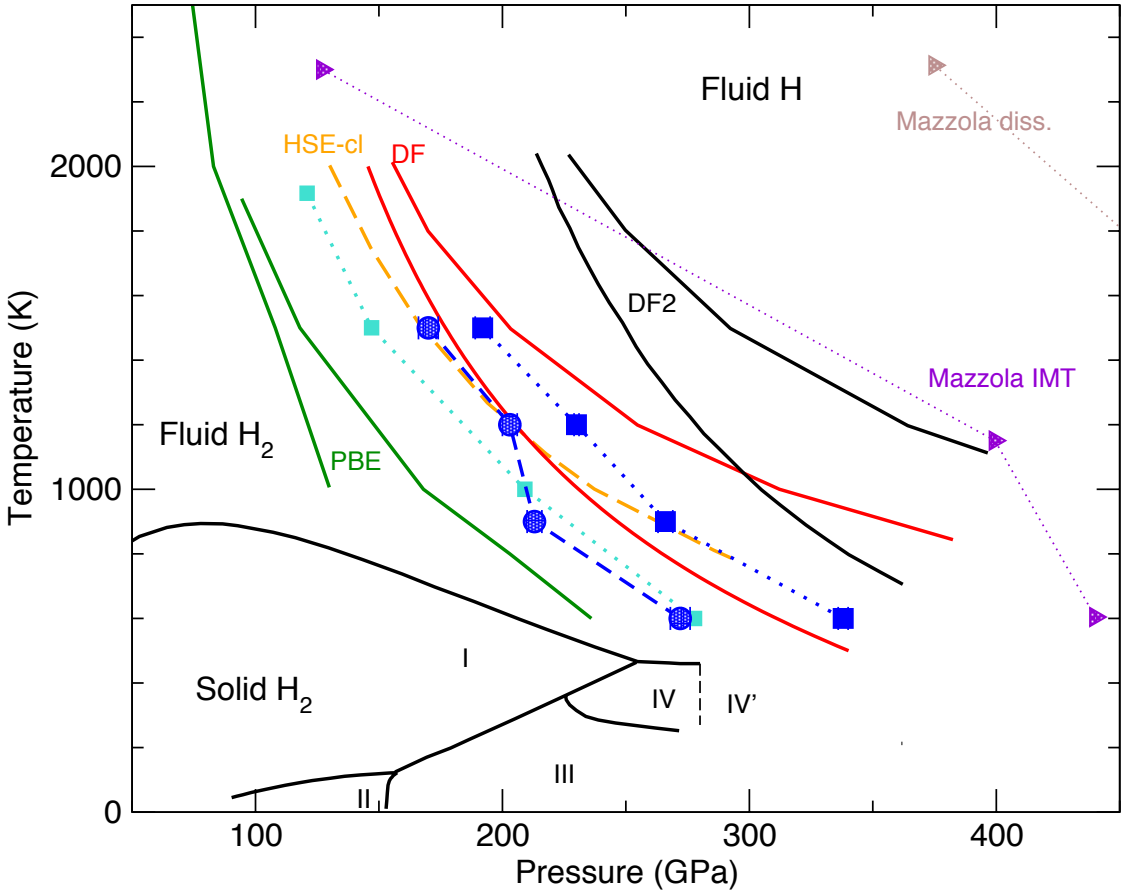

FIGURE 4.1: Comparison of CEIMC results for the liquid-liquid transition line with previous theoretical predictions. Blue circles and squares are CEIMC transition pressures for systems with quantum and classical protons, respectively. Continuous lines are predictions from Ab Initio MD or PIMD with different exchange-correlation functionals: vdW-DF2 (black lines), vdW-DF (red lines), PBE (green lines), HSE (orange dashed line). For each functional, except HSE, the line at lower pressure corresponds to quantum protons whereas the line at higher pressure corresponds to classical protons. For HSE only the classical protons line is shown. Triangles are predictions for metallization (violet) and molecular dissociation (brown) from MD-QMC . Earlier CEIMC data for classical protons are also reported as cyan squares [119]. Transition lines for the crystalline phases are shown by dashed lines. Figure from ref. [46]

found to be an intrinsic feature of the employed plasma models [122], making this prediction questionable.

An Ab Initio study was performed by Magro et al. [123], who used the Path Integral formalism in a range of temperatures from 5000 K to 10^5 K and described the state of the system as a mixture of interacting electrons and protons, without invoking the Born-Oppenheimer approximation. A first order phase transition is found between a molecular fluid and a partially ionized atomic fluid.

Scandolo [124] and Bonev [125] used the Car-Parrinello method [126] to run PBE-DFT simulations of classical protons: the former study was conducted by carrying out NPT simulations along an isotherm (T=1500 K), the latter used constant volume simulations to follow experimental Hugoniot curves. In both cases, a sharp transition between a molecular liquid and an atomic fluid is found. Moreover, in Scandolo's work, the molecular phase was found to be insulating, while the non

molecular one had a density of states that did not vanish at the Fermi level, hinting at metallic behaviour.

These simulations focused on the analysis of structural properties of the system (pair distribution functions, discontinuities in the volume vs pressure curve) while the metallic behaviour was inferred considering the electronic density of state by Scandolo. A first attempt to compute the electrical properties of the system (conductivity and reflectivity), which could be directly related to experiments, was performed by Holst et al. [127]: they ran PBE-DFT simulations at finite temperature and used the Kubo-Greenwood formula (eq. A.41) to obtain the conductivity and, thus, the reflectivity as averages over different sampled nuclear configurations. In this case, they obtain a smooth transition from a insulating molecular state to a metallic atomic fluid at any temperature considered, at variance with previous simulations. Subsequent similar calculations [128, 129] found a first order transitions for T<1500 K, which is assumed to be the critical temperature; the discrepancy is mostly due to finite size effects [45], which become very relevant when the system approaches the transition.

Morales et al. [119] employed the CEIMC method for the first time on liquid hydrogen, even if the trial wavefunction used was not as sophisticated as the one used in this work and the protons were treated as classical particles. As in previous calculations, the pair correlation functions are used to estimate the molecular character of the system; the conductivity is computed as in [127]. CEIMC results are then compared to standard PBE-DFT simulations: a first-order phase transition from molecular insulating liquid to an atomic conducting fluid is observed in both cases. However, the agreement is only qualitative: the location of the transition line can change by tens of GPa. The transition line is represented with cyan squares in fig. 4.1. Unfortunately, the CEIMC calculations were later found to be biased due to unconverged orbitals [83]

Ref. [110] presents a study which includes nuclear quantum effects at finite temperature (via Path Integrals) and non local exchange correlation functionals: PBE is compared to the vdW-DF2 functional. First of all, conductivities along a Hugoniot line obtained by PBE PIMD simulations are much higher than the vdW-DF2 PIMD ones, which in turn are consistent with experimental results: the quality of the results seems to depend on sampled nuclear configurations, while the functional used to compute the conductivities leads to minor differences. While both PBE and vdW-dF2 PIMD simulations exhibit a first order phase transition, there is a huge quantitative difference between the transition pressures: for example, at T=1000 K, they differ by more than 150 GPa. These results were complemented by Knudson et al. [14]: while their primary focus was reporting shock-wave experiments, they performed PIMD simulations with a variety of exchange correlation functionals. The transition lines are showed in fig. 4.1: there is huge variability of order 200 GPa in the transition pressures predicted using different functionals, with or without quantum effects.

Finally, Mazzola et al. [130, 131] employ a different kind of Quantum Monte Carlo method at finite temperature [132]: forces acting on the nuclei are obtained through Quantum Monte Carlo, resolving the infinite variance problem by an appropriate reweighting. The canonical ensemble is then sampled through a Langevin dynamics, where the noise given by the statistical evaluation of the forces is taken into account in order not to bias the procedure. Using this scheme, they find that the insulator-metallic phase transition and molecular dissociation are two distinct phenomena: the first transition leads to a mixed molecular metallic fluid, where molecules are short-lived; then

molecular dissociation takes place, resulting in an atomic, metallic fluid. These claims are based on considerations about the structure of the pair distribution functions and on the computation of the off-diagonal one-body density matrix: these two points will be addressed in more detail when discussing our results. We notice, however, that even the highest experimental insulator-metal transition pressures [14] are well below any of the computed pressures.

4.2 CEIMC simulations

We mentioned that CEIMC simulations were already used to study the liquid-liquid phase transition [119]; we also mentioned that the orbitals were not well converged and that, in the mean time, the method has evolved. It is therefore worthwhile repeating the earlier CEIMC simulations. Different kinds of contributions were made:

- inclusion of the nuclear quantum effects with the path integral formalism. While these effects were included in [110], the Ab Initio method chosen was vdW-DF2 DFT.
- characterization of an already existing set of CEIMC simulations with the computation of the conductivity of the system and of its one body density matrix
- runs of other CEIMC and PIMD simulations in the liquid state, studying thermo-optical properties in the portion of the phase diagram investigated

While conductivity is an obvious choice to characterize the system as insulating or metallic, we also introduce the one-body density matrix and point out how it can be used to help discriminate an insulating state from a metallic one.

4.2.1 One body density matrix

Generally speaking, insulators and metals are defined by the presence or absence of a band gap, having in mind an independent (quasi)particle picture of the system: this definition inevitably requires the knowledge of the excited states. However, this is not strictly necessary: one can define insulators and metals in terms of properties of the ground state only [56]. The one body density matrix of a system of N_e electrons in a many-body ground state $\Psi(\vec{r}_1, \ldots, \vec{r}_{N_e})$ is defined as [133]

$$\Lambda(\vec{r}, \vec{r}') = \int d\vec{r}_2 \ldots d\vec{r}_{N_e} \Psi(\vec{r}', \ldots, \vec{r}_{N_e}) \Psi^*(\vec{r}, \ldots, \vec{r}_{N_e}) \tag{4.1}$$

assuming that the wavefunction is correctly normalized to unity. It has been shown [134–137] that, for insulating systems described by single-particle orbitals in periodic potentials $\Lambda(\vec{r}, \vec{r}') \propto e^{-\gamma|\vec{r}-\vec{r}'|}$, based on the localized nature of the Wannier functions. For metals at zero temperature[1], on the other hand, the one body density matrix decays much slower, following a power-law [136] $|\Lambda(\vec{r}, \vec{r}')| \propto |\vec{r} - \vec{r}'|^{-\eta}$. These features, which assume a single particle band structure, can be extended to interacting systems [138].

[1] Since in our calculations the Born-Oppenheimer approximation is assumed, the electrons are always in their ground state, effectively being at zero temperature

The introduction of $\vec{\Delta r} = \vec{r}' - \vec{r}$ and elementary manipulations of eq. 4.1 lead to

$$\Lambda(\vec{r}, \vec{r} + \vec{\Delta r}) = \int d\vec{r}_2 \dots d\vec{r}_{N_e} \frac{\Psi(\vec{r} + \vec{\Delta r}, \dots, \vec{r}_{N_e})}{\Psi(\vec{r}, \dots, \vec{r}_{N_e})} \left|\Psi(\vec{r}, \dots, \vec{r}_{N_e})\right|^2 \tag{4.2}$$

which is now written as the average of an observable over the ground state probability distribution of the electrons (the square modulus of the ground state trial function, in VMC) and can be computed during a QMC calculation for fixed nuclear positions. In the liquid phase we assume translational invariance and isotropy. The first condition is equivalent to requiring that $\Lambda(\vec{r}, \vec{r} + \vec{\Delta r}) \equiv \Lambda(\vec{\Delta r})$: however, this is not true for the single nuclear configuration, where the positions of the nuclei break the translational invariance. Nevertheless, we can still define

$$\Lambda(\vec{\Delta r}) = \int \frac{d\vec{r}}{\Omega} \Lambda(\vec{r}, \vec{r} + \vec{\Delta r}) = \frac{1}{\Omega} \int d\vec{r}_1 \dots d\vec{r}_{N_e} \frac{\Psi(\vec{r_1} + \vec{\Delta r}, \dots, \vec{r}_{N_e})}{\Psi(\vec{r_1}, \dots, \vec{r}_{N_e})} \left|\Psi(\vec{r}, \dots, \vec{r}_{N_e})\right|^2 \tag{4.3}$$

as a simple, useful quantity to characterize the electronic state of the system. The expression in eq. 4.3 is proportional to an average in the electronic configurational space and can be evaluated during a Variational Monte Carlo calculation. In principle, $\frac{\Psi(\vec{r_1}+\vec{\Delta r}, \dots, \vec{r}_{N_e})}{\Psi(\vec{r_1}, \dots, \vec{r}_{N_e})}$ can be evaluated on a grid of vectors $\vec{\Delta r}$ collecting statistics for each $\vec{\Delta r}$ at each sampled electronic configuration $\vec{r_1}, \dots, \vec{r}_{N_e}$ through the Monte Carlo process. The computation of the electronic wavefunction is, however, quite expensive. In our case we compute $\frac{\Psi(\vec{r_1}+\vec{\Delta r}, \dots, \vec{r}_{N_e})}{\Psi(\vec{r_1}, \dots, \vec{r}_{N_e})}$ for a $\vec{\Delta r}$ uniformly sampled in the simulation box at each electronic step . Exploiting isotropy, we can average over the different directions of $\vec{\Delta r}$ and obtain $\Lambda(\Delta r) = \Lambda(|\vec{\Delta r}|)$, ensuring enough statistics for each point.

If we were to use a wavefunction with periodic boundary conditions, this would imply a periodic $\Lambda(\vec{\Delta r})$. In fact, a displacement along a lattice vector $\vec{L}_i$ produces

$$\begin{aligned} \Lambda(\vec{\Delta r} + \vec{L}_i) &= \frac{1}{\Omega} \int d\vec{r}_1 \dots d\vec{r}_{N_e} \frac{\Psi(\vec{r_1} + \vec{\Delta r} + \vec{L}_i, \dots, \vec{r}_{N_e})}{\Psi(\vec{r_1}, \dots, \vec{r}_{N_e})} \left|\Psi(\vec{r}, \dots, \vec{r}_{N_e})\right|^2 = \\ &= \frac{1}{\Omega} \int d\vec{r}_1 \dots d\vec{r}_{N_e} \frac{\Psi(\vec{r_1} + \vec{\Delta r}, \dots, \vec{r}_{N_e})}{\Psi(\vec{r_1}, \dots, \vec{r}_{N_e})} \left|\Psi(\vec{r}, \dots, \vec{r}_{N_e})\right|^2 = \Lambda(\vec{\Delta r}) \end{aligned} \tag{4.4}$$

However, if we use twist average boundary condition, we get

$$\begin{aligned} \Lambda_{\vec{k}}(\vec{\Delta r} + \vec{L}_i) &= \frac{1}{\Omega} \int d\vec{r}_1 \dots d\vec{r}_{N_e} \frac{\Psi_{\vec{k}}(\vec{r_1} + \vec{\Delta r} + \vec{L}_i, \dots, \vec{r}_{N_e})}{\Psi_{\vec{k}}(\vec{r_1}, \dots, \vec{r}_{N_e})} \left|\Psi_{\vec{k}}(\vec{r}, \dots, \vec{r}_{N_e})\right|^2 = \\ &= \frac{1}{\Omega} \int d\vec{r}_1 \dots d\vec{r}_{N_e} e^{i\theta_{\vec{k}}} \frac{\Psi_{\vec{k}}(\vec{r_1} + \vec{\Delta r}, \dots, \vec{r}_{N_e})}{\Psi_{\vec{k}}(\vec{r_1}, \dots, \vec{r}_{N_e})} \left|\Psi_{\vec{k}}(\vec{r}, \dots, \vec{r}_{N_e})\right|^2 = \\ &= e^{i\theta_{\vec{k}}} \Lambda_{\vec{k}}(\vec{\Delta r}) \end{aligned} \tag{4.5}$$

so that the final value of $\Lambda(\vec{\Delta r} + \vec{L}_i)$, averaged over the different twists, is:

$$\Lambda_{TABC}(\vec{\Delta r} + \vec{L}_i) = \frac{1}{N_{\vec{k}}} \sum_{\vec{k}} e^{i\theta_{\vec{k}}} \Lambda_{\vec{k}}(\vec{\Delta r}) \tag{4.6}$$

and the density matrix has no longer period equal to $\vec{L}_i$. In particular, if a Monkhorst-Pack grid $N_{k1} \times N_{k2} \times N_{k3}$ is used, the periodicity is $N_{ki}\vec{L}_i$. $\Lambda(\Delta r)$ for a fixed classical nuclear configuration at T=600 K and $P = 203.0 \pm 5$ GPa is reported in fig. 4.2 as an example of the qualitative

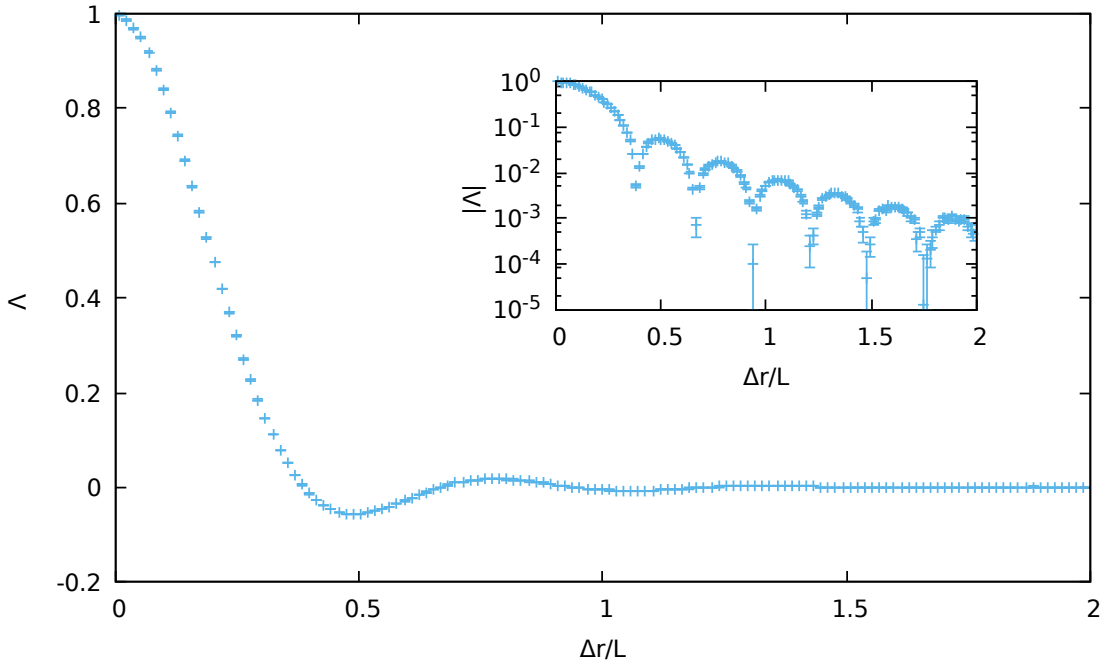

FIGURE 4.2: $\Lambda(\Delta r)$ at a fixed nuclear configuration at T=600 K, $P = 203.0 \pm 5$ GPa vs $\Delta r/L$, where L is the length of one side the cubic simulation box. In the inset, its absolute value $|\Lambda|$ on a semilog scale.

form found in our calculations: the functions decay while showing regular oscillations, that can be better appreciated in the inset. We are interested in the decay factor modulating these oscillations: following Mazzola [131], we compute the integral of the absolute value of the one body density matrix, that in this specific case can be written in spherical coordinates as

$$\Gamma_\Lambda = 4\pi \int_0^{r_c} d\Delta r |\Lambda(\Delta r)| \Delta r^2 \tag{4.7}$$

where r_c is a cutoff distance which will be discussed later. In this way we should be able to discriminate the two different asymptotic behaviours: for insulators, the exponential decay translates to a smaller value of the integral in eq. 4.7; on the other hand, the value of the integral for metals critically depends on the exponent η and may be also divergent for $r_c \to \infty$ ($\eta < 3$). In any case, we should be able to detect a radically distinct behaviour: for this reason, we call it electron localization parameter.

4.3 Methods

A set of pre-existing CEIMC simulations of liquid hydrogen was used to compute conductivities and the electron localization parameter Γ_Λ at T=600 K for classical protons over a range of different densities ($1.24 < r_s < 1.50$ a.u., where $\frac{4}{3}\pi r_s^3 = \frac{\Omega}{N}$). Cubic cells were employed for 54 protons; simulations of 128 protons were run at selected points to check for finite size effects.

Calculations of optical properties were performed for CEIMC-generated nuclear configurations within DFT, using a plane-wave energy cutoff of 1360 eV, an $8 \times 8 \times 8$ Monkhorst–Pack grid of k

points, a smearing of 0.086 eV in the self- consistent cycle. It is common practice to replace the delta function in eq. A.41 with Gaussian functions that smooth the appearance of the resulting conductivity, taking care of the finite spacing among different energy levels caused by an inevitable discrete sampling of the k-points. We use a smearing (i.e., the width of the Gaussian) of 0.3 eV to regularize the frequency- dependent conductivity. Both the PBE and vdW-DF1 exchange-correlation functionals were employed to check for their influence on the results. The dc conductivity has been estimated by extrapolating the isotropic dynamical conductivity to $\omega = 0$. The number of bands was set to 64 and 120 for systems of 54 and 128 electrons, respectively.

To study thermoelectrical properties, such as optical and thermal conductivities, absorption coefficients and reflectivities in a bigger region of the liquid phase diagram, additional CEIMC simulations were performed at different densities corresponding to the 50-250 GPa pressure range along the T=900,1200,1500 K isotherms. Systems of 54 atoms were considered. A different number of path integral beads N_P was used depending on temperature ($N_P = 6$ for T=900 K, $N_P = 4$ for T=1200,1500 K) Twisted boundary conditions were enforced on the trial wavefunction using a 4x4x4 k-point grid. The parameters of the trial wavefunction were optimized on random snapshots of a first, relatively short run for every density. DFT-PIMD simulations were performed using a customized version of VASP. The simulation cells were composed of 128 atoms; the Γ point was used, employing the vdW-DF1 exchange correlation functional. We considered the T=3000, 5000, 6000, 8000 K isotherms; $N_P = 4$ for T=3000 and 5000 K, $N_P = 2$ for T=6000 and 8000 K. For every trajectory, 16 snapshots of the nuclear configurations were extracted. Linear response theory within the DFT framework, described in the previous chapter, was then employed on these static configurations to compute and average the selected optical properties. We employed the HSE functional which, while being computationally expensive, is known to reproduce experimental band gaps for many semiconductors [139] and was already successfully used in [110]. Static values of these observables are generally plagued by finite size effects: in this work they were carefully extrapolated from the entire curve at finite frequencies. Additional PIMD simulations were performed at T=1500 and 2400 K around 141 GPa to compare with existing experiments. Both 54 and 128 atoms cells were used (3x3x3 k-grid and Γ point sampling, respectively); the number of beads N_P was 6 for T=1500 K and 4 for T=2400 K.

4.4 Results

4.4.1 Conductivity and one body density matrix

The parameters declared in the previous section were carefully tested. An example of a convergence study of the conductivity for a metallic configuration is reported in fig. 4.3: in this case, increasing the number of k-points smooths the oscillations of the function caused by the limited sampling of the Brillouin zone. A similar effect can be created at much lower computational cost by increasing the smoothing parameter. From fig. 4.3 we can also see that the conductivity sharply decreases when approaching $\omega = 0$ irrespective of the $\vec{k}$ point mesh. This is most likely due to the discrete energy differences among bands at the same k-point (vertical transitions are the only ones considered in eq. A.62), stemming from finite size effects. This is corroborated by fig. 4.4, where conductivities for five different protonic configurations with N=54 and five with N=128 are showed in the proximity

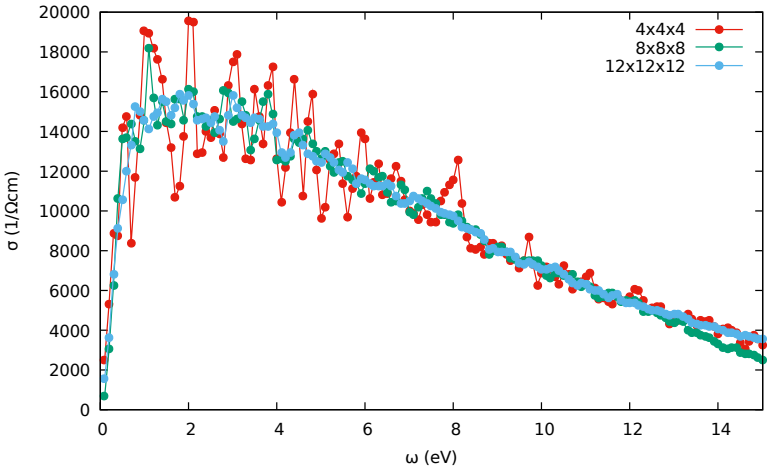

FIGURE 4.3: Effects of k-point sampling for conductivity of a classical protonic configuration sampled at T=1200 K, $r_s = 1.34$ a.u. The PBE functional was employed for the calculations

of $\omega = 0$: the configurations with the lower number of protons reach a systematically lower value of the conductivity. We assume that a better value of the dc conductivity can be obtained by fitting the function excluding a neighbourhood of the origin (approximately 0.6 eV for the case pictured).

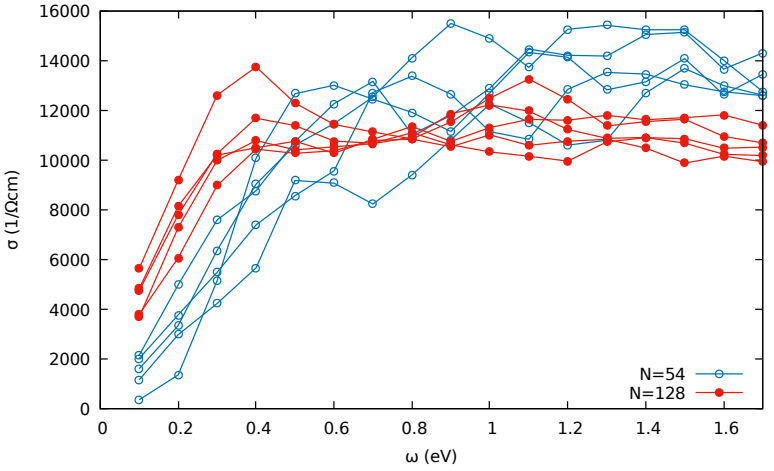

FIGURE 4.4: Finite size effects for different classical protonic configurations at T=1200 K, $r_s = 1.34$ a.u. The vdW-DF functional was employed for the calculations

At this point, another important parameter is the number of bands used to compute the optical properties: higher values of ω require a higher number of bands to get a converged conductivity, as shown in fig. 4.5.

We studied finite size effects for Γ_Λ as well. In fig. 4.6 the associated integral $I_\Lambda(\Delta r) = 4\pi \int_0^{\Delta r} d\Delta r' |\Lambda(\Delta r')| \Delta r'^2$ is plotted against its upper bound for two different system sizes ($N = 54$ and $N = 128$); for each size, ten different nuclear configurations were considered, resulting in the curves displayed in figure. They start nearly identical, becoming more and more different with increasing Δr: this suggests that the integral does not strongly depend on the specific nuclear configuration. At higher Δr one must also take into account that the radial integration magnifies the noise which affects $\Lambda(\Delta r)$ when Δr is large. The comparison between the two sizes shows that

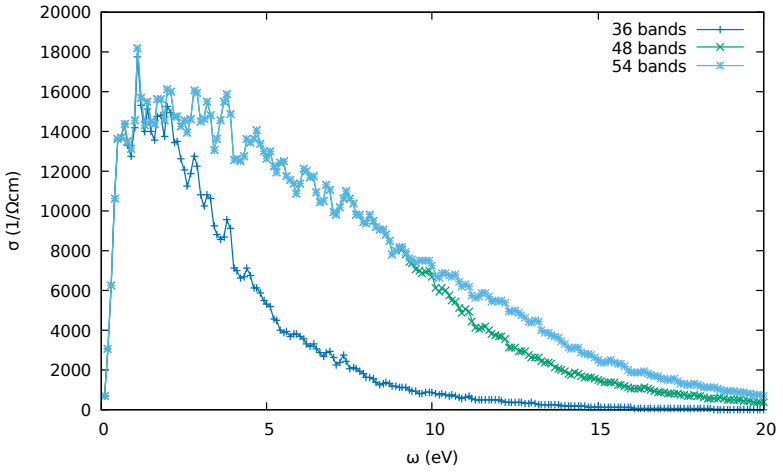

FIGURE 4.5: Convergence of the conductivity with respect to number of bands employed for a single classical protonic configuration at T=1200 K, $r_s = 1.34$ a.u. The PBE functional was employed for the calculations

the differences are smaller than the differences between two different nuclear configurations at the same size. We can now show the results obtained along an isotherm T=600 K for a system of

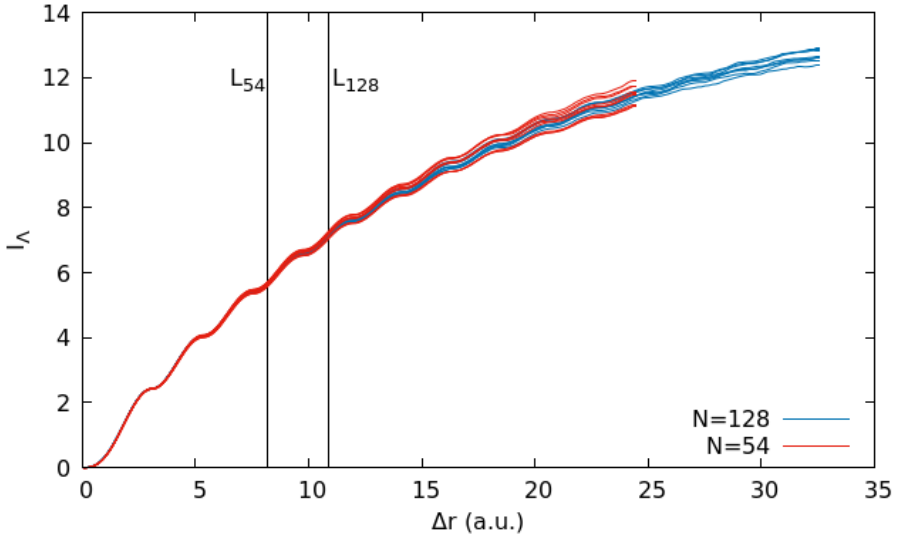

FIGURE 4.6: Integral of the absolute value of the one-body density matrix vs upper bound of integration: $I_\Lambda = 4\pi \int_0^{\Delta r} d\Delta r' |\Lambda(\Delta r')| \Delta r'^2$. We considered two systems with number of protons $N = 54$ and $N = 128$ at $r_s = 1.34$ and T=1200 K without nuclear quantum effects (classical protons). The vertical lines labelled L_{54} and L_{128} indicate the box length of the two simulation cells ($N = 54$ and $N = 128$, respectively). For each system size, ten curves corresponding to ten different nuclear configurations sampled along the trajectory are shown.

classical protons across the molecular dissociation transition. In fig. 4.7 we present four different quantities. Two are related to the structure of the system: the equation of state, pressure vs r_s, (top left panel) and the amplitude of the first maximum of the pair radial distribution function, corresponding to the bond length r_{mol} (bottom left panel). The other two quantities are the ones discussed above, namely conductivity and electronic localization parameter Γ. The discontinuity of the equation of state signals a first order phase transition; the simultaneous disappearance of the

first maximum in $g_{pp}(r)$ is evidence for molecular dissociation. At the same time, the conductivity shows a sharp increase at the dissociation pressure, smoothly increasing afterwards. We point out that while the conductivities obtained using the PBE and vdW-dF exchange correlation functionals are quantitatively slightly different, their qualitative behaviour is essentially the same. This strongly suggests that exchange-correlation functional used in the optical calculation has minor effects on the computation, while the proper statistical sampling of the nuclear configurations is much more important. This point was already raised by Morales [110].

The same discontinuity is evident for the localization parameter Γ: while the values of the integrals are not converged with respect to the finite size of the radial grid, it is still possible to identify two distinct behaviours across the transition if the upper bound of the integration r_{cut} is large enough. In this way, we can legitimately establish a connection between molecular dissociation and metallization, in contrast with the results obtained in [131].

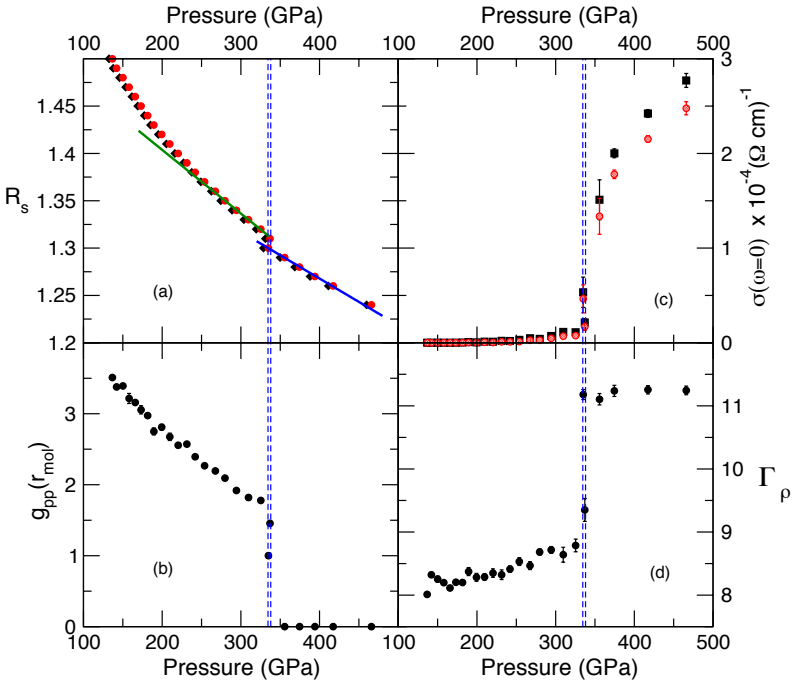

FIGURE 4.7: Results for the system with classical protons along the T = 600 K isotherm. (a, upper Left) Equation of state, showing the pressure dependence of the coupling parameter r_s. Raw data (black diamonds) and size-corrected results (red circles) are reported, together with linear fits for the two branches near the discontinuity. Note that below ∼ 200 GPa the equation of state is for the metastable fluid because the thermodynamically stable state should be the phase I crystal. (b, lower Left) Amplitude of the molecular peak observed in the proton–proton radial distribution functions $g_{pp}(r_{mol})$, where $r_{mol} \approx 1.4$ a.u. Beyond the vertical blue lines, $g_{pp}(r)$ does not exhibit a maximum but only a shoulder at the molecular distance. (c, upper Right) dc electrical conductivity as obtained by optical calculation within DFT with two X-C approximations (black squares, PBE; red circles, vdW-DF). The points are averages over 10 statistically independent nuclear configurations sampled during the CEIMC run at each density. (d, lower Right) Integral of the absolute value of the single-electron off-diagonal density matrix from variational Monte Carlo, as a measure of the electron localization, obtained by averaging over 10 independent nuclear configurations. In all panels the blue vertical dashed lines represent the transition pressure with its uncertainty. Picture from [46].

4.4.2 Optical properties around the liquid-liquid phase transition

As explained in the methods section, we performed additional CEIMC simulations at T=900,1200,1500 K to extend the pressure range under examination; at higher temperatures ($T = 3000, 5000, 6000, 8000$ K) we performed more affordable DFT-PIMD using vdW-DF exchange-correlation functional, which gives transition pressures consistent with the CEIMC ones at T=1200 and 1500 K (see fig. 4.1). The computation of the optical properties follows the procedure described above for the conductivity, with the same issues around $\omega = 0$. In particular, we computed

- the static conductivity σ_0, which is a direct indication of the metallicity of the system
- the reflectivity, which can be measured experimentally and is used, like σ_0, to characterize the metallic state of the system
- the absorption coefficient and the electronic thermal conductivity, which relate to the power absorbed by the system and to its heat conduction.

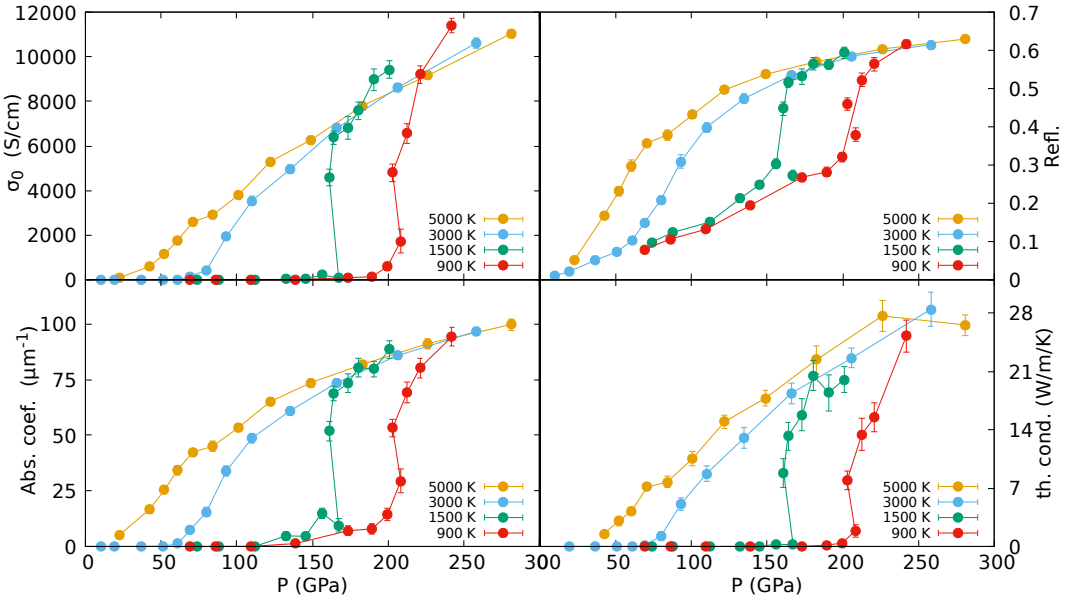

FIGURE 4.8: Top left panel: Static electrical conductivity σ_0 along different isotherms. Top right panel: reflectivity obtained at $\omega = 2.3$ eV, corresponding to a wavelength $\lambda = 539$ nm, assuming vacuum as the adjacent medium. Bottom left panel: absorption coefficient at $\omega = 2.3$ eV. Bottom right panel: thermal conductivity.

Our main results are reported in fig. 4.8: The electrical and thermal conductivities are static values ($\omega = 0$); the reflectivity and the absorption coefficient are computed at $\omega = 2.3$ eV, corresponding to a wavelength $\lambda = 539$ nm of electromagnetic radiation (visible light), close to the one used for example in [140] to probe the system. The top left panel clearly shows a discontinuity for the conductivity at lower temperatures, indicating a first-order phase transition. The curves then become smoother at higher temperatures, implying termination of the first order transition line at a critical temperature between 1500K and 3000K. Above the critical temperature molecular

dissociation and metallization become continuous processes. Incidentally, the highest computed conductivity would put liquid hydrogen on par with steel, that is a poor metal.

Other useful qualitative indications for experiments can be extracted from fig. 4.8. For example, the increase of the absorption coefficient in the visible spectrum can be directly related to the darkening of the sample by visual inspection. While dropping abruptly, the reflectivity does not vanish at the transition. This is an important point when evaluating experimental reflectivities: usually, only a part of the sample is assumed to undergo the metallization transition and become reflective, while the other part of the sample is assumed to remain insulating with vanishing reflectivity. From our data we can see that the reflectivity of hydrogen differs from zero even in the insulating state near the transition (see, for example, [10]). This can introduce systematic errors when trying to disentangle the contribution to the reflectivity coming from the metallic part of the system.

Some experimental works [10, 47] study the temperature of the sample while increasing the laser power: they find that the maximum observed temperature does not increase indefinitely with the laser power, but it reaches a plateau. Temperature not increasing while providing more power is interpreted as the signature of the transition (latent heat). We show that the absorption coefficient is discontinuous at the transition. Notice, however, that there seems to be a region both at T=900 and 1500 K before the transition pressure where the absorption coefficient smoothly increases from zero: depending on the supposed thickness of the heated part of the sample, this could implicate the observation of higher absorption and smaller transmittivity before the transition pressure where the discontinuity takes place. On the other hand, the thermal conductivity behaves as the optical one, showing a sharp increase at the transition.

As mentioned above, the experimental values can be affected by very large error bars. That is the case in fig. 4.9, where reflectivities compatible with T=6000 K (blue points) were taken from ref. [141]. We can compare these data with the reflectivity values we obtained along the T=6000 K isotherm: while one could say the two sets are compatible, smaller uncertainties would be needed to make a stronger statement.

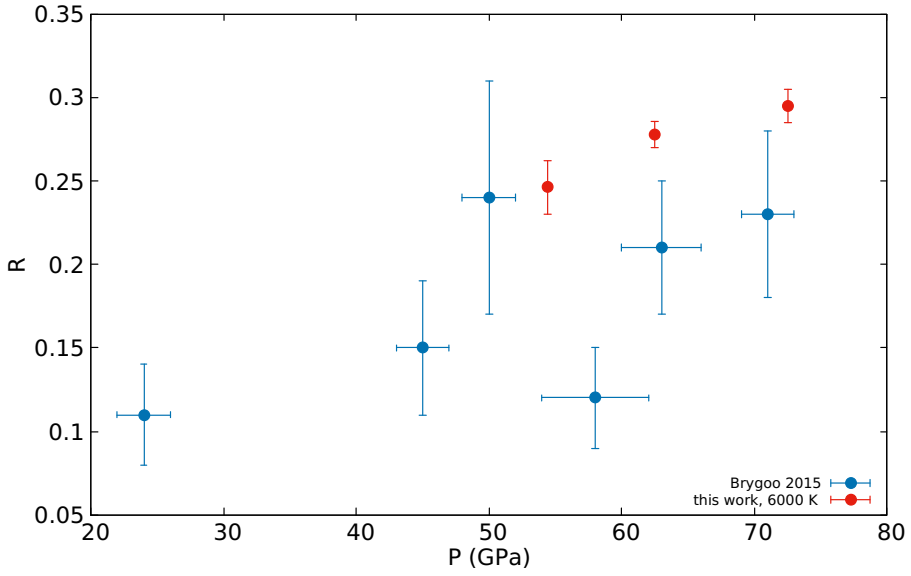

FIGURE 4.9: Comparison with experimental reflectivity

Fig. 4.10 shows experimental measurements for dynamical conductivity at T=2400 K [140], which points to an insulating state when extrapolated to $\omega = 0$. Two distinct groups of curves from our calculations are displayed, as well: metallic (yellow curves) and insulating states (blue curves). We also performed simulations with both CEIMC and DFT-PIMD at T=2400 K, with 54 and 128 protons, to check if different Ab Initio methods or finite size corrections showed any discrepancies. Since we are working at constant volume, the volume of the cell was guessed to provide a pressure close to the experimental one (141 GPa) by extrapolating the results at other pressures. Small size effects are observed for PIMD (0-2 GPa); on the other hand, CEIMC and PIMD pressures at similar volumes differ by about 15 GPa. The conductivities are obtained by averaging the dynamical conductivities over 16 different sampled protonic configurations, point by point. Our data at T=2400 K shows a clear metallic behaviour, at variance with the reported experimental measurements, which point at an insulating character of the system at the same thermodynamic point (yellow curves); a similar insulating behaviour can be found in our simulations at T=1500 K (blue curves). This indicates that a transition line compatible with the data from [140] should be shifted either towards higher temperatures or higher pressures than ours. Notice, however, that ref. [140] proposes a smooth transition, with a large portion of the phase diagram occupied by a semimetallic fluid. This is completely in contradiction with our results and with other experiments, which found a sharp first order transition.

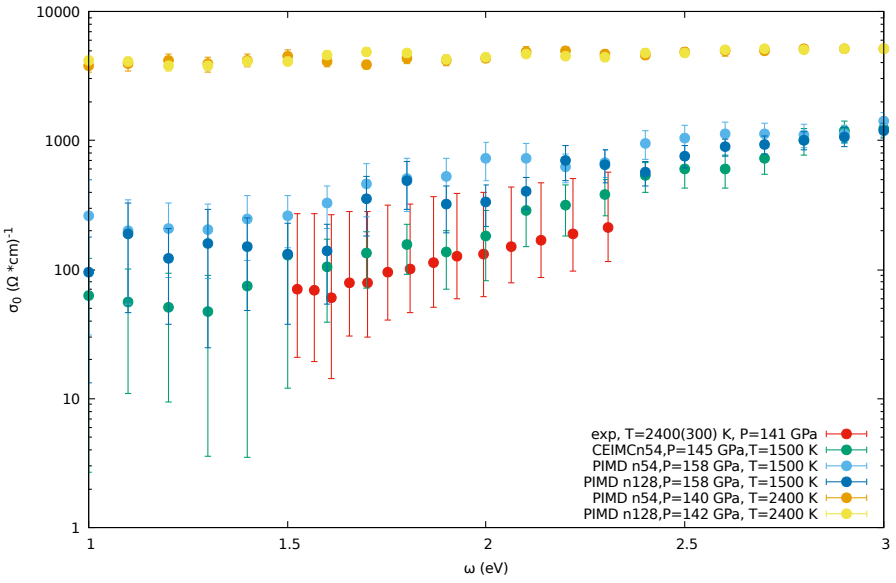

FIGURE 4.10: Comparison with experimental conductivity for different simulations. The volume cell for each simulation was chosen in order to give a pressure close to the experimental one (141 GPa). Different cell sizes and Ab Initio methods were used to check for any discrepancy.

We can compare our findings with previous theoretical works. As is apparent from the location of the transition line in fig. 4.1, results produced by DFT simulations highly depend on the exchange correlation functional used; nevertheless they provide sharp transitions, as indicated by the presence of lines. It is interesting to see if optical properties across the transition are also affected by the choice of the functional. Refs. [127] and [128] studied the transition in dense liquid hydrogen using PBE-DFT molecular dynamics with classical protons. They both computed the equation of state for liquid hydrogen and characterized the transition by computing optical properties: In particular, they obtained static conductivities at T=1500 K, which can be directly compared with our results

(see the blue and yellow curves in fig. 4.11). The blue curve [127] displays a smooth transition, very different from our red curve: the conductivity evolves continuously, showing a smooth transition from an insulating to a metallic state. It was later understood that this was caused by small simulation cells and insufficient $\vec{k}$-point sampling [45]: Lorenzen et al., after carefully studying the finite-size effects, produced the yellow curve, which displays a sharp increase at the transition. This shows how the nature of the transition can be sensitive to the computational parameters employed in the simulations (more specifically, to finite size effects). On the other hand, even if qualitatively similar to our red curve, the yellow curve displays a transition quantitatively shifted by about 40 GPa. As discussed above, when analyzing the conductivity and the electronic localization parameter, optical properties depend primarily on the sampled nuclear configurations: it is no surprise to detect a very different insulator-metal transition pressure for PBE and vdW-DF, since the transition pressures are essentially linked to the change in the structural properties of the system (discontinuity in the equation of state).

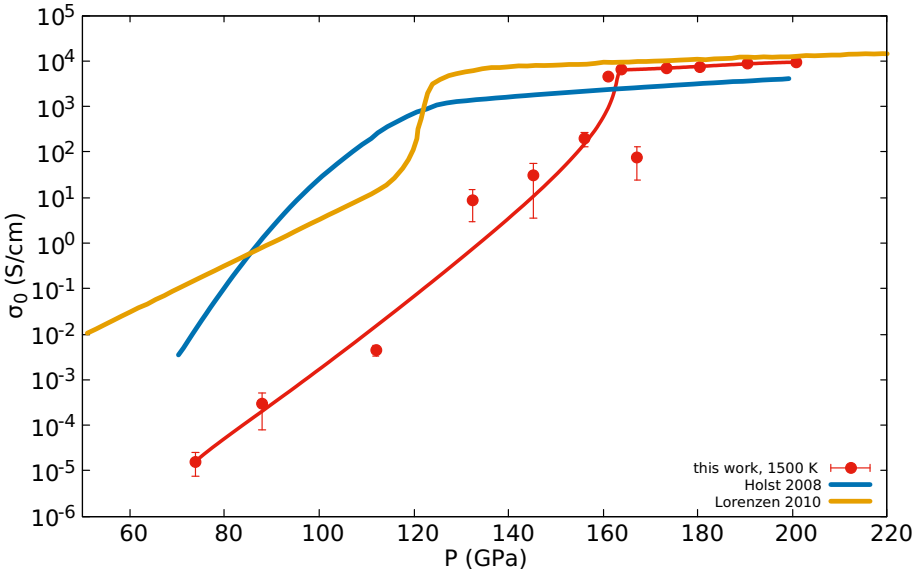

FIGURE 4.11: Comparison among conductivities at T=1500 K with previous theoretical calculations from [127, 128]

4.5 Conclusions

In this chapter, we showed how liquid hydrogen can successfully be characterized through the computation of several optical properties: we performed simulations of high pressure hydrogen using state of the art techniques, CEIMC and vdFW-PIMD, required to account for the different effects that are relevant for this system (nuclear quantum effects, dispersion interactions) and are usually neglected. We first focused on the region close to the molecular dissociation transition line, discussing how to compute conductivities and introducing an electronic localization parameter Γ. We then used these two quantities to show that, according to our simulations, molecular dissociation and the insulator-metal transition take place at the same time.

Furthermore, we extended the explored region of the phase diagram to have a better picture of the liquid over a wider range of pressures. From the study of thermooptical properties, we confirmed

a first-order insulator-metal phase transition with a critical temperature lying between 1500 and 3000 K. A direct comparison with experiments is not easy, because experimental data collected in dynamical experiments naturally have large error uncertainties and their interpretation must usually be supported by semiempirical models. The disagreement among different experiments (for example, concerning the location of the transition line in fig. 1.3) is a clear sign of the difficulties faced when performing these experiments. Given all these caveats, a meaningful quantitative agreement with experiments is difficult to pursue at the moment; however, our qualitative considerations about optical properties may, we hope, help experimentalists in processing their data, especially for measurements of reflectivity or absorption coefficients.

Finally, we discussed what level of accuracy is needed from a computational point of view to correctly describe the transition and its properties. The locations of the transition lines obtained from DFT simulations vary a lot depending on the functional used (see fig. 4.1). The very nature of CEIMC guarantees more reliable predictions due to the accurate electronic energies computed.

Conclusions

In this work, we performed Ab Initio simulations of high pressure hydrogen at finite temperature in the solid and liquid phases. We described in Chapter 1 how performing experiments at such high pressures is complicated and the information obtained is partial. For this reason, Ab Initio simulations are a valuable tool to complement and interpret experimental data and can also guide experiments with their predictive power. In Chapter 2 we introduced the foundations of Density Functional Theory (DFT), which is the method of choice to perform Ab Initio simulations for condensed matter at reasonable computational cost. We stressed how its predictive power for high pressure hydrogen is hindered by the exchange-correlation functional approximation, which is uncontrolled. In particular, we showed in Chapter 3 how enthalpy differences among candidate crystal structures for the molecular solid phases were so small (≈ 10 meV/proton) that changing the exchange-correlation functional has a deep impact on the resulting phase diagram in the pressure range considered ($P > 200$ GPa). At the same time, estimating nuclear quantum effects using the harmonic approximation leads to errors of the same order of magnitude, making questionable the picture obtained by DFT.

For these reasons, our efforts were devoted to employing the Coupled Electron Ion Monte Carlo (CEIMC) method to run finite temperature simulations of high pressure hydrogen. The electronic energies are evaluated using Variational Monte Carlo (VMC), a method which critically relies on the goodness of the trial wavefunction employed. However, thanks to the variational principle, we can tell if one wavefunction produces better or worse results than another one: we have a meaningful criterion to compare different wavefunctions. Path integrals take care of nuclear quantum effects exactly. We applied CEIMC both to the low temperature, solid phase and to the high-temperature, liquid phase.

In the first case, in particular, we performed DFT-PIMD and CEIMC simulations at T=200 K and T=414 K of selected structures of interest: C2c and Cmca12 at T=200 K, where Eremets et al. [18] claim to find metallic hydrogen at $P \approx 350$ GPa, and the mixed structure Pc48 at T=414 K, close to the melting line. A comparison between the results produced by the two methods shows different behaviours, depending on the initial structure considered and on the thermodynamic conditions. Using DFT, C2c is not stable across the interval of pressures investigated: while a rigorous study of the stability needs free energy calculations, a series of transitions to already known structures can be reasonably inferred, in qualitative agreement with the results reported in refs. [116] and [104]. This is in open contrast with our CEIMC results, which represent the benchmark to validate DFT: in particular, DFT seems to enhance rotational activity of the molecules, which may lead to an artificial lowering of energy barriers (suggested in ref. [112]), due to out of plane rotations. At

variance with C2c, the Cmca12 structure behaves in the same manner for both methods: molecules do not rotate and maintain their orientations during the whole trajectory. Even if their structural behaviour is clearly different, both structures exhibit a semimetallic behaviour at $r_s = 1.31$ (≈ 350 GPa), which increases with density, regardless of the Ab Initio method employed. This could be consistent with Eremets's findings, but the fact that the semimetallic behaviour is qualitatively the same does not enable us to discriminate among the different structures. At higher temperature, we find some discrepancies between DFT-PIMD and CEIMC, this time for Pc48: subtle differences in the protonic motion in the weakly bonded layers can condition significantly the electronic character of the system, as we reported.

In Chapter 4 we used CEIMC data to characterize the liquid-liquid phase transition, analyzing optical properties across the transition. The computation of conductivities and the introduction of the electronic localization parameter Γ showed that molecular dissociation and the insulator-metal transition take place at the same time; moreover, these processes can be classified as a first-order phase transition, because of the reported abrupt discontinuity in the equation of state and in the optical properties, The liquid can be better characterized by exploring a larger region of the phase diagram far from the transition: this can be relevant for experimentalists, who must often process their data in convoluted ways and with many assumptions, as in the case of reflectivity or absorption coefficients. Finally, we stressed how DFT-based simulations report highly variable results for the location of the liquid-liquid transition line and how CEIMC is inherently more accurate and reliable thanks to the VMC electronic energies: as such, it should be used as a benchmark for these calculations.

In conclusion, we showed how it is possible to successfully employ the CEIMC method to perform finite temperature simulations, given the proper amount of computational resources. In the solid phase, we were able to make qualitative statements that, nevertheless, highlight the inadequacy of DFT for the C2c structure at low temperatures; in the liquid phase, the CEIMC method, integrated with DFT, can be used to make strong predictions about the liquid-liquid phase transition and characterize to a large extent the fluid.

Appendix A

Transport and thermoelectrical kinetic coefficients

In this appendix, the linear theory of the transport and thermoelectrical kinetic coefficients is discussed. General expressions are obtained and then employed in the context of the Density Functional Theory framework.

In a linear regime, we can write the response of the electrical and heat current densities $\vec{J}_e$ and $\vec{J}_q$ to an external electric field $\vec{E}$ and to a temperature gradient ∇T as [142]

$$\begin{aligned} \vec{J}_e &= \sigma(\vec{E} - S\nabla T) \\ \vec{J}_q &= ST\vec{J}_e - \lambda\nabla T \end{aligned} \tag{A.1}$$

where σ is the electrical conductivity, S is the Seebeck coefficient and λ the thermal conductivity. These two equations sum up Ohm's law (σ) of electrical conduction, Fourier's law of thermal conduction (λ) and the Seebeck and Peltier effects (S), that couple the two phenomena. Thermoelectricity is an example of a wider class of irreversible processes that can be better understood from a theoretical point of view by considering the time evolution of the entropy of the system.

A.1 Irreversible thermodynamics and kinetic coefficients

When electrical and heat currents flow under the influence of an electric potential V or a temperature difference, the variation of the local entropy ds and the relative flux $\vec{J}_s$ can be written as [143]

$$ds = \frac{1}{T}de - \frac{\tilde{\mu}}{T}dn \tag{A.2}$$

$$\vec{J}_s = \frac{1}{T}\vec{J}_e - \frac{\tilde{\mu}}{T}\vec{J}_n \tag{A.3}$$

$$\tilde{\mu} = \mu + qV \tag{A.4}$$

where q is the charge of the carriers, de the variation of energy and dn the variation of the number particle density. During non equilibrium, irreversible processes there is a net generation of entropy,

i.e.

$$\frac{ds}{dt} = \frac{\partial s}{\partial t} + \nabla \cdot \vec{J}_s \quad , \quad \frac{ds}{t} > 0 \tag{A.5}$$

On the other hand, energy and number of particles are conserved, implying the validity of the following continuity equations:

$$0 = \frac{\partial e}{\partial t} + \nabla \cdot \vec{J}_e \tag{A.6}$$

$$0 = \frac{\partial n}{\partial t} + \nabla \cdot \vec{J}_n \tag{A.7}$$

Using eqs. A.2 and A.3, the two terms in eq. A.5 can be computed as

$$\frac{\partial s}{\partial t} = \frac{1}{T}\frac{\partial e}{\partial t} - \frac{\tilde{\mu}}{T}\frac{\partial n}{\partial t} \tag{A.8}$$

$$\nabla \cdot \vec{J}_s = \nabla\left(\frac{1}{T}\right) \cdot \vec{J}_e - \nabla\left(\frac{\tilde{\mu}}{T}\right) \cdot \vec{J}_n + \frac{1}{T}\nabla \cdot \vec{J}_e - \frac{\tilde{\mu}}{T}\nabla \cdot \vec{J}_n \tag{A.9}$$

Putting all together, eq. A.5 becomes

$$\begin{aligned} \frac{ds}{dt} &= \frac{1}{T}\left(\frac{\partial e}{\partial t} + \nabla \cdot \vec{J}_e\right) - \frac{\mu}{T}\left(\frac{\partial n}{\partial t} + \nabla \cdot \vec{J}_n\right) + \nabla\left(\frac{1}{T}\right) \cdot \vec{J}_e - \nabla\left(\frac{\mu}{T}\right) \cdot \vec{J}_n = \\ &= \nabla\left(\frac{1}{T}\right) \cdot \vec{J}_e - \nabla\left(\frac{\mu}{T}\right) \cdot \vec{J}_n \end{aligned} \tag{A.10}$$

Eq. A.10 is an example that shows how the irreversible variation of the entropy can be generally written as

$$\frac{ds}{dt} = \sum_k \vec{X}_k \cdot \vec{J}_k \quad , \quad \vec{X}_k = \nabla F_k \tag{A.11}$$

where $\vec{X}_k$ are the so called "affinities", generalized forces steming from non homogeneous intesive parameters ∇F_k. This expression will be convenient when we will introduce Kubo linear response theory. The set of affinities and fluxes is not unequivocally determined. When dealing with thermoelectrics, it is more convenient to use the heat flux:

$$\vec{J}_Q = T\vec{J}_s = \vec{J}_e - \tilde{\mu}\vec{J}_n \tag{A.12}$$

turning eq. A.10 in

$$\frac{ds}{dt} = \nabla\left(\frac{1}{T}\right) \cdot (\vec{J}_Q + \mu\vec{J}_n) - \nabla\left(\frac{\mu}{T}\right) \cdot \vec{J}_n = \nabla\left(\frac{1}{T}\right) \cdot \vec{J}_Q - \frac{\nabla\mu}{T} \cdot \vec{J}_n \tag{A.13}$$

Currents flow when affinities are present: in a linear regime, it is natural to write

$$\vec{J}_i = \sum_k \tilde{L}_{ik}\vec{X}_k \tag{A.14}$$

In the thermoelectrical case, this leads to

$$-\vec{J}_n = L_{11}\frac{1}{T}\nabla\tilde{\mu} + L_{12}\nabla\frac{1}{T} \tag{A.15}$$

$$\vec{J}_Q = L_{21}\frac{1}{T}\nabla\tilde{\mu} + L_{22}\nabla\frac{1}{T} \tag{A.16}$$

The coefficients L_{ij} are called kinetic coefficients:they can be easily related to the usual set of transport coefficients in eq. A.1. In fact, if the proper chemical potential μ is constant, $\tilde{\mu} = qV$ and a comparison of eq. A.1 and A.16 yields

$$\sigma = q^2\frac{L_{11}}{T} \tag{A.17}$$

$$\lambda = \frac{1}{T^2}\frac{L_{11}L_{22} - L_{12}^2}{L_{11}} \tag{A.18}$$

$$S = -\frac{L_{12}}{qTL_{11}} \tag{A.19}$$

The kinetic coefficients can be computed within the linear response theory framework which will be discussed next.

A.2 Quantum linear response theory

We consider a system with Hamiltonian $\hat{\mathcal{H}}_0$ which is affected by a small external perturbation [144–146] so that

$$\hat{\mathcal{H}}(t) = \hat{\mathcal{H}}_0 + \hat{\mathcal{H}}'(t) \tag{A.20}$$

$$\hat{\mathcal{H}}'(t) = e^{st}\hat{A} \tag{A.21}$$

where $\hat{A}$ does not explicitly depend on time and the exponential prefactor assures that $\lim_{t\to-\infty}\hat{\mathcal{H}}'(t) = 0$ (adiabatic switching). A density matrix $\hat{\rho}_0$ can be associated to the unperturbed system, whose form depends on the suitable statistical ensemble: however, since the system is at equilibrium, the density matrix is stationary and we require that $\left[\hat{\mathcal{H}}_0, \hat{\rho}_0\right] = 0$. Assuming that the density matrix is normalized, the average value of any observable B is

$$\langle B\rangle_0 = \mathrm{Tr}\left(\hat{\rho}_0\hat{B}\right) \tag{A.22}$$

If the time-independent part of the perturbation is small enough, the perturbed density matrix $\hat{\rho}'(t)$ can be written as

$$\hat{\rho}'(t) \approx \hat{\rho}_0 + e^{st}\Delta\hat{\rho}(t) \tag{A.23}$$

where $\Delta\hat{\rho}(t)$ is linear in $\hat{A}$. $\hat{\rho}'(t)$ satisfies the following time evolution equation:

$$i\frac{\partial}{\partial t}\hat{\rho}'(t) = \left[\hat{\mathcal{H}}_0 + \hat{\mathcal{H}}'(t), \hat{\rho}'(t)\right] \tag{A.24}$$

with the initial condition $\hat{\rho}'(t=-\infty)=\hat{\rho}_0$. The linearized version of eq. A.24 is:

$$is\Delta\hat{\rho}=\left[\hat{\mathcal{H}}_0,\Delta\hat{\rho}\right]+\left[\hat{A},\hat{\rho}_0\right] \tag{A.25}$$

At this point, it is convenient to switch to the interaction picture, introducing:

$$\Delta\hat{\rho}_I(t) \quad = \quad e^{i\hat{\mathcal{H}}_0 t}\Delta\hat{\rho}e^{-i\hat{\mathcal{H}}_0 t} \tag{A.26}$$

Thus, we have:

$$\frac{\partial}{\partial t}(e^{st}\Delta\hat{\rho}_I(t)) \quad = \quad e^{st}\left(s\Delta\hat{\rho}_I(t)+\frac{\partial\Delta\hat{\rho}_I(t))}{\partial t}\right)= \tag{A.27}$$

$$= \quad e^{st}\left(s\Delta\hat{\rho}_I(t)+i\left[\hat{\mathcal{H}}_0,\Delta\hat{\rho}_I(t)\right]\right)=ie^{st}\left[\hat{\rho}_0,\hat{A}_I(t)\right] \tag{A.28}$$

where in the last step we used eq.A.25. Integrating, we obtain

$$e^{st}\Delta\hat{\rho}_I(t)=i\int_{-\infty}^{t}dt'e^{st'}\left[\rho_0,\hat{A}_I(t')\right] \tag{A.29}$$

i.e.

$$\Delta\hat{\rho}=i\int_{-\infty}^{t}dt'e^{s(t'-t)}\left[\rho_0,\hat{A}_I(t'-t)\right]=i\int_0^{\infty}dte^{-st}\left[\rho_0,\hat{A}_I(-t)\right] \tag{A.30}$$

If the ensemble is canonical ($\hat{\rho}_0=\frac{e^{-\beta\hat{\mathcal{H}}_0}}{Z}$), eq. A.30 can be manipulated through the following identity:

$$i\hat{\rho}_0\int_0^{\beta}d\lambda\frac{\partial}{\partial t}\hat{A}_I(-t-i\lambda)=\hat{\rho}_0\int_0^{\beta}d\lambda\frac{\partial}{\partial\lambda}\hat{A}_I(-t-i\lambda)=$$

$$= \quad \hat{\rho}_0(\hat{A}_I(-t-i\beta)-\hat{A}_I(-t))=\hat{\rho}_0(e^{\beta\hat{\mathcal{H}}_0}\hat{A}_I(-t)e^{-\beta\hat{\mathcal{H}}_0}-\hat{A}_I(-t))=-\left[\rho_0,\hat{A}_I(-t)\right] \tag{A.31}$$

The average value of B under the influence of the perturbation $\mathcal{H}'$ is

$$\langle B\rangle' \quad = \quad \mathrm{Tr}\left(\hat{\rho}'(t)\hat{B}\right)\approx\langle B\rangle_0+\mathrm{Tr}\left(\Delta\hat{\rho}\hat{B}\right)=\langle B\rangle_0+i\int_0^{\infty}dte^{-st}\,\mathrm{Tr}\left(\left[\rho_0,\hat{A}_I(-t)\right]\hat{B}\right)$$

$$= \quad \langle B\rangle_0-\int_0^{\infty}dte^{-st}\int_0^{\beta}d\lambda\,\mathrm{Tr}\left(\hat{\rho}_0\frac{\partial}{\partial t}\hat{A}_I(-t-i\lambda)\hat{B}\right)= \tag{A.32}$$

$$= \quad \langle B\rangle_0-\int_0^{\infty}dte^{-st}\int_0^{\beta}d\lambda\langle\frac{\partial}{\partial t}\hat{A}_I(-t-i\lambda)\hat{B}\rangle \tag{A.33}$$

where $\langle..\rangle$ stands for the thermal average over ρ_0.

A.2.1 Conductivity

A first, relevant example is the calculation of the static conductivity [146]. In this case we assume a perturbation induced by a static electric field $\vec{E}=\vec{E}_0e^{i\vec{q}\cdot\vec{r}}$, slowly varying in space ($\vec{q}\to 0$): the

corresponding perturbation $\mathcal{H}'$ is

$$\mathcal{H}' = \lim_{s\to 0} e^{st} \int d\vec{r} n(\vec{r})\phi(\vec{r}) \quad , \quad \vec{E} = -\nabla\phi(\vec{r}) \tag{A.34}$$

We are interested in the electric current $\vec{J}$ generated by the perturbation. To apply eq. A.33 we need the time derivative of the perturbation, i.e.

$$\begin{aligned} \frac{\partial}{\partial t}\hat{A}_I(-t-i\lambda) &= \int d\vec{r}\phi(\vec{r})\frac{\partial}{\partial t}\hat{n}(\vec{r},-t-i\lambda) = -\int d\vec{r}\phi(\vec{r})\nabla\cdot\hat{\vec{J}}(\vec{r},-t-i\lambda) = \\ &= \int d\vec{r}\nabla\phi(\vec{r})\cdot\hat{\vec{J}}(\vec{r},-t-i\lambda) = -\int d\vec{r}\vec{E}\cdot\hat{\vec{J}}(\vec{r},-t-i\lambda) \end{aligned} \tag{A.35}$$

where we performed the integration by parts assuming periodic boundary conditions. The result for the expectation value of the electric current J^α is

$$J^\alpha(\vec{r}) = \langle\hat{J}^\alpha(\vec{r})\rangle = \lim_{s\to 0}\int_0^\infty dt e^{-st}\int d\vec{r}' e^{i\vec{q}\cdot\vec{r}'}\int_0^\beta d\lambda\langle\hat{\vec{J}}^\gamma(\vec{r}',-t-i\lambda)\hat{J}^\alpha(\vec{r})\rangle\vec{E}_0^\gamma \tag{A.36}$$

where we dropped the index I for the time evolution of the operators. We are not interested in the local details of the current: they can be eliminated by considering the spatial Fourier transform for operators and average values:

$$\hat{J}^\alpha_{\vec{q}} = \int d\vec{r} e^{-i\vec{q}\cdot\vec{r}}\hat{J}^\alpha(\vec{r}) \tag{A.37}$$

$$J^\alpha_{\vec{q}} = \int d\vec{r} e^{-i\vec{q}\cdot\vec{r}}J^\alpha(\vec{r}) = \lim_{s\to 0}\int_0^\infty dt e^{-st}\int_0^\beta d\lambda\langle\hat{\vec{J}}^\gamma_{-\vec{q}}(-t-i\lambda)\hat{J}^\alpha_{\vec{q}}\rangle\vec{E}_0^\gamma \tag{A.38}$$

and then considering in the limit for $\vec{q}\to 0$:

$$J^\alpha = \frac{1}{\Omega}\lim_{\vec{q}\to 0}\hat{J}^\alpha_{\vec{q}} = \lim_{s\to 0}\frac{1}{\Omega}\int_0^\infty dt e^{-st}\int_0^\beta d\lambda\langle\hat{\vec{J}}^\gamma(-t-i\lambda)\hat{J}^\alpha\rangle\vec{E}_0^\gamma \tag{A.39}$$

where Ω is the volume of the system. Since the electrical conductivity tensor is defined as

$$J^\alpha = \sigma^{\alpha\gamma}E_0^\gamma \tag{A.40}$$

by comparison, we obtain

$$\sigma^{\alpha\gamma} = \frac{1}{\Omega}\lim_{s\to 0}\int_0^\infty dt e^{-st}e^{-i\omega t}\int_0^\beta d\lambda\langle\hat{\vec{J}}^\gamma(-t-i\lambda)\hat{J}^\alpha\rangle \tag{A.41}$$

When dealing with isotropic systems (liquids, for instance), there is little point in considering the full conductiviy tensor. The isotropic conductivity is

$$\sigma = \frac{1}{3}\operatorname{Tr}\sigma^{\alpha\gamma} \tag{A.42}$$

A.2.2 Kinetic coefficients

We can apply the Kubo formula (eq. A.33) to the kinetic coefficients if we identify the perturbation $\mathcal{H}'$ as the energy change induced by the heat transfer [146]. In this case, the time derivative $\frac{\partial}{\partial t}\hat{A}_I(t)$

can be written as

$$\frac{\partial}{\partial t}\hat{A}(t) = T\frac{\partial s}{\partial t} = T\sum_k \vec{X}_k \cdot \int d\vec{r}\hat{\vec{J}}_k(\vec{r}) \tag{A.43}$$

We recall that for thermoelectric problems, we consider two currents: $\vec{J}_n \equiv \vec{J}_1$, the particle-density current, and $\vec{J}_Q \equiv \vec{J}_2$, the heat current. The operators $\hat{\vec{J}}_k(\vec{r})$ are the local operators correspoding to macroscopic average values $\vec{J}_k$.

Using the same manipulations as in the conductivity case, the result is

$$J_i^\alpha = -\frac{T}{\Omega}\lim_{s\to 0}\int_0^\infty dt e^{-st}\int_0^\beta d\lambda \sum_{k,\gamma}\langle \hat{J}_k^\gamma(-t-i\lambda)\hat{J}_i^\alpha\rangle X_k^\gamma \tag{A.44}$$

Consequently, the expressions for the kinetic coefficients (tensorial and isotropic forms) are the following:

$$L_{ik}^{\alpha\gamma} = -\frac{T}{\Omega}\lim_{s\to 0}\int_0^\infty dt e^{-st}\int_0^\beta d\lambda\langle \hat{J}_k^\gamma(-t-i\lambda)\hat{J}_i^\alpha\rangle \tag{A.45}$$

$$L_{ik} = \frac{1}{3}\operatorname{Tr} L_{ik}^{\alpha\gamma} \tag{A.46}$$

A.3 DFT implementation

A rigorous but computationally affordable method to evaluate eqs. A.41 and A.45 for extended interacting systems is not available at the moment. Still, at least qualitative indications can come from DFT. We will describe which form these equations take in an independent particle picture. To compute the kinetic coefficients, we must provide expressions for $\hat{\vec{J}}_n$ and $\hat{\vec{J}}_Q$. It is convenient to introduce them in a second quantization formalism [146]:

$$\begin{aligned}
\hat{\mathcal{H}} &= \sum_s E_s a_s^\dagger a_s \\
\hat{J}_i &= \sum_{s,s'}(j_i)_{s,s'} a_{s'}^\dagger a_s \\
(j_i)_{s,s'} &= \langle s|\hat{j}_i|s'\rangle \\
\hat{j}_1 = \hat{j}_n &= \hat{p} \\
\hat{j}_E &= \frac{1}{2}\left[\hat{\mathcal{H}}\hat{p} + \hat{p}\hat{\mathcal{H}}\right] \\
\hat{j}_2 = \hat{j}_Q &= \hat{j}_E - \mu\hat{j}_n \\
(j_i(t+i\lambda)_{s,s'}) &= \langle s|\hat{j}_i|s'\rangle\, e^{i(t+i\lambda)(E_s - E_{s'})}
\end{aligned} \tag{A.47}$$

where $a_s^\dagger$ and a_s are, respectively, fermionic creation and annihilation operators of the eigenstates s of the single electron Hamiltonian.

A.3.1 Static kinetic coefficients

Plugging the definitions of the currents into the isotropic expression of the kinetic coefficients in eq.A.46, we obtain

$$\begin{aligned} L_{ij} &= -\frac{T}{3\Omega}\lim_{\epsilon\to 0}\mathrm{Tr}\left(\rho_0\int_0^\beta d\lambda\int_0^\infty e^{-\epsilon t}dt\hat{\vec{J}}_i(0)\cdot\hat{\vec{J}}(t+i\lambda)\right)= \\ &= -\frac{T}{3\Omega}\lim_{\epsilon\to 0}\mathrm{Tr}\left(\rho_0\sum_{s,s',r,r'}\int_0^\beta d\lambda\int_0^\infty dte^{-\epsilon t}(\hat{\vec{j}}_i)_{ss'}\left[\hat{\vec{j}}_j(t+i\lambda)\right]_{rr'}a_s^\dagger a_{s'}a_r^\dagger a_{r'}\right) = \quad \text{(A.48)} \\ &= -\frac{T}{3\Omega}\lim_{\epsilon\to 0}\mathrm{Tr}\left(\rho_0\sum_{s,s',r,r'}\int_0^\beta d\lambda\int_0^\infty dte^{i(t+i\lambda)(E_r-E_{r'})}e^{-\epsilon t}(\hat{\vec{j}}_i)_{ss'}(\hat{\vec{j}}_j)_{rr'}a_s^\dagger a_{s'}a_r^\dagger a_{r'}\right) \end{aligned}$$

Applying Wick's theorem [147], the evaluation of the trace results in

$$\begin{aligned} \mathrm{Tr}\left(\rho_0 a_s^\dagger a_{s'}a_r^\dagger a_{r'}\right) &= f_s\delta_{s,s'}f_r\delta_{r,r'}+f_s\delta_{s,r'}(1-f_r)\delta_{r,s'} \quad \text{(A.49)} \\ f_s &= \frac{1}{e^{\beta(E_s-\mu)}-1} \quad \text{(A.50)} \end{aligned}$$

The first term is connected to the diagonal matrix element of the currents: they are assumed to be null, otherwise they would produce divergent contributions when performing the time integral [148]. Eq. A.49 becomes

$$L_{ij} = -\frac{T}{3\Omega}\lim_{\epsilon\to 0}\sum_{s\neq r}f_s(1-f_r)\int_0^\beta d\lambda\int_0^\infty dte^{i(t+i\lambda)(E_r-E_s)}e^{-\epsilon t}(\hat{\vec{j}}_i)_{sr}\cdot(\hat{\vec{j}}_j)_{rs}$$

The evaluation of the two integrals yields:

$$\begin{aligned} \int_0^\beta d\lambda e^{-\lambda(E_r-E_s)} &= \frac{1-e^{-\beta(E_r-E_s)}}{E_r-E_s} \quad \text{(A.51)} \\ \lim_{\epsilon\to 0}\int_0^\infty dte^{it(E_s-E_r-\epsilon t)} &= \pi\delta(E_r-E_s)+iP\left(\frac{1}{E_r-E_s}\right) \quad \text{(A.52)} \end{aligned}$$

Putting all together, we obtain

$$L_{ij} = \frac{T}{3\Omega}\sum_{s\neq r}\frac{f_r-f_s}{E_s-E_r}(\hat{\vec{j}}_i)_{sr}\cdot(\hat{\vec{j}}_j)_{rs}\pi\delta(E_s-E_r-\omega) \quad \text{(A.53)}$$

where the imaginary part vanishes because it is antisymmetric in r and s. At this point, we can discuss the form of the matrix elements: they can easily be computed as

$$(\hat{\vec{j}}_Q)_{sr} = \frac{1}{2}(E_s+E_r)(\hat{\vec{j}}_1)_{sr}-\mu(\hat{\vec{j}}_1)_{sr} \quad \text{(A.54)}$$

Since $\hat{\vec{j}}_1\equiv\hat{\vec{j}}_n$, $\hat{\vec{j}}_2\equiv\hat{\vec{j}}_Q$, their matrix elements can be written in a compact way as

$$(\hat{\vec{j}}_i)_{sr} = \left(\frac{1}{2}(E_s+E_r)-\mu\right)^{i-1}(\hat{\vec{j}}_1)_{sr} \quad \text{(A.55)}$$

For periodic systems, we work with Bloch waves and the quantum number s becomes $s \equiv \vec{k}, \mu$. Computing the matrix element of the current,

$$\begin{aligned}(\hat{\vec{j}})_{\vec{k},\mu\vec{k}',\nu} &= -i\frac{1}{\Omega}\int d\vec{r} e^{-i\vec{k}\cdot\vec{r}} u^*_{\vec{k},\mu}(\vec{r})\nabla\left(e^{i\vec{k}'\cdot\vec{r}} u_{\vec{k}',\nu}(\vec{r})\right) = \\ &= \delta_{\vec{k},\vec{k}'}\left(\vec{k}\delta_{\mu,\nu} - \frac{i}{\Omega}\int d\vec{r} u^*_{\vec{k},\mu}(\vec{r})\nabla\left(u_{\vec{k}',\nu}(\vec{r})\right)\right) \qquad \text{(A.56)}\end{aligned}$$

we see that it is non null only if the same $\vec{k}$ is considered. In the end, eq. A.53 becomes

$$\begin{aligned}L_{ij} &= \frac{T}{3\Omega}\sum_{s\neq r}\frac{f_r - f_s}{E_s - E_r}(E_s-\mu)^{i-1}(E_r-\mu)^{j-1}(\vec{j}_1)_{sr}\cdot(\vec{j}_1)_{rs}\left(\pi\delta(E_s-E_r)\right) = \qquad \text{(A.57)} \\ &= \frac{T}{3\Omega}\sum_{s\neq r}\frac{f_r - f_s}{E_s - E_r}(E_s-\mu)^{i-1}(E_r-\mu)^{j-1}(\vec{j}_1)_{sr}\cdot(\vec{j}_1)_{rs}\left(\pi\delta(E_s-E_r)\right) = \qquad \text{(A.58)} \\ &= \frac{T}{3\Omega}\sum_{\vec{k}\mu,\nu}(E_{\vec{k},\mu}-\mu)^{i-1}(E_{\vec{k},\nu}-\mu)^{j-1}\frac{f_{\vec{k},\nu}-f_{\vec{k},\mu}}{E_{\vec{k},\mu}-E_{\vec{k},\nu}} \\ &\times \langle\vec{k},\nu|(\hat{\vec{j}}_i)|\vec{k},\mu\rangle\cdot\langle\vec{k},\mu|(\hat{\vec{j}}_i)|\vec{k},\nu\rangle\,\delta(E_{\vec{k},\mu}-E_{\vec{k},\nu}) \qquad \text{(A.59)}\end{aligned}$$

The expression in eq. A.59 cannot be used computationally, since it contains the indeterminate form $\frac{f_s-f_r}{E_s-E_r}$ when $E_s = E_r$. We can tweak the expression by manually adding an ω dependence:

$$\begin{aligned}L_{ij}(\omega) &= \frac{T}{3\Omega}\pi\sum_{s\neq r}\frac{f_r - f_s}{\omega}(E_s-\mu)^{i-1}(E_r-\mu)^{j-1}(\vec{j}_1)_{sr}\cdot(\vec{j}_1)_{rs}\delta(E_s-E_r-\omega) = \\ &= \frac{T\pi}{3\omega}\sum_{\vec{k}\mu,\nu}(E_{\vec{k},\mu}-\mu)^{i-1}(E_{\vec{k},\nu}-\mu)^{j-1}(f_{\vec{k},\nu}-f_{\vec{k},\mu}) \\ &\times \langle\vec{k},\nu|(j_i)|\vec{k},\mu\rangle\,\langle\vec{k},\mu|(j_i)|\vec{k},\nu\rangle\,\delta(E_{\vec{k},\mu}-E_{\vec{k},\nu}-\omega) \qquad \text{(A.60)} \\ L_{ij} &= \lim_{\omega\to 0} L_{ij}(\omega) \qquad \text{(A.61)}\end{aligned}$$

The static kinetic coefficients are then obtained through a limit process ($\omega \to 0$). Notice that $L_{ij}(\omega)$ are, in general, not the correct kinetic coefficients for time dependent perturbations, but only a "trick" to resolve the indeterminate form and get the static limit. The real $L_{ij}(\omega)$ have a slightly different form, but it was showed [129] that the static limit of the thermal conductivity λ, which is the transport coefficient we are interested in, is unaffected.

A.3.2 Dynamical conductivity and optical properties

An exception is the dynamical conductivity $\sigma^{\alpha\gamma}(\omega)$, which is proportional to L_{11}(eq. A.19). In fact, adding the ad hoc ω term, the resulting expression for the conductivity is

$$\mathbf{Re}(\sigma^{\alpha\gamma}(\omega)) = \frac{\pi}{\omega}\sum_{\vec{k}\mu,\nu}(f_{\vec{k},\nu}-f_{\vec{k},\mu})\,\langle\vec{k},\nu|(j^\alpha)|\vec{k},\mu\rangle\,\langle\vec{k},\mu|(j^\gamma)|\vec{k},\nu\rangle\,\delta(E_{\vec{k},\mu}-E_{\vec{k},\nu}-\omega) \qquad \text{(A.62)}$$

Eq. A.62 is the Kubo-Greenwood formula, which can be rigorously proved using a time dependent electrical field as external perturbation [146, 149]. The imaginary part, that we disregarded, can be

conveniently evaluated using the Kramers-Kronig relations [150]:

$$\mathbf{Im}(\sigma^{\alpha\gamma}(\omega)) = -\frac{1}{\pi} P \int_{-\infty}^{\infty} d\omega' \frac{\mathbf{Re}(\sigma^{\alpha\gamma}(\omega'))}{\omega - \omega'} \tag{A.63}$$

Once the conductivity is computed, other interesting optical properties (the dielectric constant $\epsilon(\omega)$, the complex refractive index $\tilde{n}(\omega)$, the reflectivity $R(\omega)$, the absorption coefficient $\alpha(\omega)$) can be derived through well known equalities [151]:

$$\epsilon(\omega) = 1 + \frac{4\pi\sigma(\omega)}{\omega} \tag{A.64}$$

$$\tilde{n}(\omega) = n(\omega) + ik(\omega) = \sqrt{\epsilon(\omega)} \tag{A.65}$$

$$R(\omega) = \frac{(1 - n(\omega))^2 + k(\omega)^2}{(1 + n(\omega))^2 + k(\omega)^2} \tag{A.66}$$

$$\alpha(\omega) = \frac{2\omega}{c} k(\omega) \tag{A.67}$$

Bibliography

[1] H. U.S. Institute for Basic Standards. Cryogenics Division and Roder, *Survey of the properties of the hydrogen isotopes below their critical temperatures*. U.S. Dept. of Commerce, National Bureau of Standards, for sale by the Supt. of Docs., U.S. Govt. Print. Off., 1973. (Page iii).

[2] E. Wigner and H. B. Huntington, "On the Possibility of a Metallic Modification of Hydrogen," *J. Chem. Phys.*, vol. 3, pp. 764–770, 1935. (Pages iii, 1).

[3] N. W. Ashcroft, "Metallic hydrogen: A high-temperature superconductor?," *Physical Review Letters*, vol. 21, no. 26, pp. 1748–1749, 1968. (Page iii).

[4] H.-k. Mao and R. Hemley, "Ultrahigh-pressure transitions in solid hydrogen," *Reviews of Modern Physics*, vol. 66, no. 2, 1994. (Pages iii, 2, 3, 5).

[5] R. T. Howie, P. Dalladay-Simpson, and E. Gregoryanz, "Raman spectroscopy of hot hydrogen above 200 GPa.," *Nature materials*, vol. 14, no. February, pp. 1–5, 2015. (Pages iii, 2, 5, 46, 51).

[6] S. T. Weir, A. C. Mitchell, and W. J. Nellis, "Metallization of fluid molecular hydrogen at 140 GPa (1.4 Mbar)," *Physical Review Letters*, vol. 76, no. 11, pp. 1860–1863, 1996. (Pages iii, 1, 6, 7, 72).

[7] J. W. Stewart, "Compression of solidified gases to 20,000 kg/cm2 at low temperature," *Journal of Physics and Chemistry of Solids*, vol. 1, no. 3, pp. 146–158, 1956. (Page 1).

[8] H. K. Mao, "High-pressure physics: sustained static generation of 1.36 to 1.72 megabars.," *Science (New York, N.Y.)*, vol. 200, no. 4346, pp. 1145–7, 1978. (Page 1).

[9] H. K. Mao and P. M. Bell, "Observations of Hydrogen at Room Temperature (25 °C) and High Pressure (to 500 Kilobars).," *Science (New York, N.Y.)*, vol. 203, no. August, pp. 1004–1006, 1979. (Pages 1, 3).

[10] M. Zaghoo, A. Salamat, and I. F. Silvera, "Evidence of a first-order phase transition to metallic hydrogen," *Physical Review B - Condensed Matter and Materials Physics*, vol. 93, no. 15, pp. 1–7, 2016. (Pages 1, 6, 7, 83).

[11] K. Ohta, K. Ichimaru, M. Einaga, S. Kawaguchi, K. Shimizu, T. Matsuoka, N. Hirao, and Y. Ohishi, "Phase boundary of hot dense fluid hydrogen," *Nature Scientific Reports*, vol. 5, p. 16560, 2015. (Pages 1, 6, 7).

[12] W. J. Nellis, "Dynamic compression of rare gases and deuterium at high pressures," *Contributions to Plasma Physics*, vol. 45, no. 3-4, pp. 243–253, 2005. (Page 1).

[13] W. J. Nellis, "Dynamic compression of materials: metallization of fluid hydrogen at high pressures," *Reports on Progress in Physics*, vol. 69, no. 5, p. 1479, 2006. (Page 1).

[14] M. D. Knudson, M. P. Desjarlais, A. Becker, R. W. Lemke, K. R. Cochrane, M. E. Savage, D. E. Bliss, T. R. Mattsson, and R. Redmer, "Direct observation of an abrupt insulator-to-metal transition in dense liquid deuterium," *Science*, vol. 348, no. 6242, pp. 1455–1460, 2015. (Pages 1, 7, 74, 75).

[15] Y. Akahama, M. Nishimura, H. Kawamura, N. Hirao, Y. Ohishi, and K. Takemura, "Evidence from x-ray diffraction of orientational ordering in phase III of solid hydrogen at pressures up to 183 GPa," *Physical Review B - Condensed Matter and Materials Physics*, vol. 82, no. 6, pp. 3–6, 2010. (Pages 2, 4, 5).

[16] I. Goncharenko and P. Loubeyre, "Neutron and X-ray diffraction study of the broken symmetry phase transition in solid deuterium.," *Nature*, vol. 435, no. 7046, pp. 1206–9, 2005. (Pages 2, 4).

[17] P. Dalladay-Simpson, R. T. Howie, and E. Gregoryanz, "Evidence for a new phase of dense hydrogen above 325 gigapascals," *Nature*, vol. 529, no. 7584, pp. 63–67, 2016. (Pages 2, 5).

[18] M. I. Eremets, I. A. Troyan, and A. P. Drozdov, "Low temperature phase diagram of hydrogen at pressures up to 380 GPa. A possible metallic phase at 360 GPa and 200 K," *arXiv preprint arXiv:1601.04479*, jan 2016. (Pages 2, 5, 6, 44, 65, 87).

[19] R. P. Dias, O. Noked, and I. F. Silvera, "New insulating low temperature phase in dense hydrogen: The phase diagram to 421 GPa," *arXiv preprint arXiv:1603.02162*, 2016. (Pages 2, 6).

[20] W. H. Keesom, J. De Smedt, and H. H. Mooy, "„" *Commun. Kamerlingh Onnes Lab., Univ. Leiden*, vol. 19, no. 209d, 1930. (Page 3).

[21] R. L. Mills and A. F. Schuch, "Crystal structure of normal hydrogen at low temperatures," *Physical Review Letters*, vol. 15, no. 18, pp. 722–724, 1965. (Page 3).

[22] I. Silvera, "The solid molecular hydrogens in the condensed phase: Fondamentals and static properties," *Reviews of Modern Physics*, vol. 52, no. 2, pp. 393–452, 1980. (Page 3).

[23] R. M. Hazen, H. K. Mao, L. W. Finger, and R. J. Hemley, "Single-crystal x-ray diffraction of n-H2 at high pressure," *Physical Review B*, vol. 36, no. 7, pp. 3944–3947, 1987. (Page 3).

[24] H. K. Mao, a. P. Jephcoat, R. J. Hemley, L. W. Finger, C. S. Zha, R. M. Hazen, and D. E. Cox, "Synchrotron X-ray Diffraction Measurements of Single-Crystal Hydrogen to 26.5 Gigapascals.," *Science*, vol. 239, no. 4844, pp. 1131–4, 1988. (Page 3).

[25] J. Van Kranendonk, *Solid hydrogen: Theory of the properties of Solid H_ 2, HD, and D_ 2.* Springer US, 1983. (Page 3).

[26] E. J. Allin, T. Feldman, and H. L. Welsh, "Raman Spectra of Liquid and Solid Hydrogen," *The Journal of Chemical Physics*, vol. 24, no. 5, p. 1116, 1956. (Page 3).

[27] S. S. Bhatnagar, E. J. Allin, and H. L. Welsh, "The {Raman} spectra of liquid and solid {H_2}, {D_2}, and HD at high resolution," *Can. J. Phys.*, vol. 40, no. 1, p. 9, 1962. (Page 3).

[28] R. J. Hemley, H. K. Mao, and J. F. Shu, "Low-frequency vibrational dynamics and structure of hydrogen at megabar pressures," *Physical Review Letters*, vol. 65, no. 21, pp. 2670–2673, 1990. (Page 3).

[29] A. F. Goncharov, R. J. Hemley, and H. K. Mao, "Vibron frequencies of solid H2 and D2 to 200 GPa and implications for the P-T phase diagram," *Journal of Chemical Physics*, vol. 134, no. 17, pp. 1–5, 2011. (Pages 3, 4, 5).

[30] I. F. Silvera and R. J. Wijngaarden, "New low-temperature phase of molecular deuterium at ultrahigh pressure," *Physical Review Letters*, vol. 47, no. 1, pp. 39–42, 1981. (Pages 3, 4, 5).

[31] H. E. Lorenzana, I. F. Silvera, and K. A. Goettel, "Orientational Phase-Transitions in Hydrogen At Megabar Pressures," *Physical Review Letters*, vol. 64, no. 16, pp. 1939–1942, 1990. (Page 3).

[32] R. J. Hemley, J. H. Eggert, and H. K. Mao, "Low-frequency Raman spectroscopy of deuterium to megabar pressures at 77-295 K," *Physical Review B*, vol. 48, no. 9, pp. 5779–5788, 1993. (Page 3).

[33] M. Hanfland, R. J. Hemley, and H. K. Mao, "Novel infrared vibron absorption in solid hydrogen at megabar pressures," *Physical Review Letters*, vol. 70, no. 24, pp. 3760–3763, 1993. (Pages 3, 5).

[34] A. F. Goncharov, I. I. Mazin, J. H. Eggert, R. J. Hemley, and H. K. Mao, "Invariant points and phase transitions in deuterium at megabar pressures," *Physical Review Letters*, vol. 75, no. 13, pp. 2514–2517, 1995. (Pages 3, 5).

[35] A. Goncharov, R. Hemley, H. Mao, and J. Shu, "New High-Pressure Excitations in Parahydrogen," *Physical Review Letters*, vol. 80, no. 1, pp. 101–104, 1998. (Page 3).

[36] L. Cui, N. H. Chen, and I. F. Silvera, "Excitations, order parameters, and phase diagram of solid deuterium at megabar pressures," *Physical Review B*, vol. 51, no. 21, pp. 14987–14997, 1995. (Page 4).

[37] I. I. Mazin, R. J. Hemley, A. F. Goncharov, M. Hanfland, and H.-k. Mao, "Quantum and Classical Orientational Ordering in Solid Hydrogen," *Physical Review Letters*, vol. 78, no. 6, pp. 1066–1069, 1997. (Page 5).

[38] C. S. Zha, Z. Liu, and R. J. Hemley, "Synchrotron infrared measurements of dense hydrogen to 360 GPa," *Physical Review Letters*, vol. 108, no. 14, pp. 1–5, 2012. (Page 5).

[39] M. I. Eremets and I. a. Troyan, "Conductive dense hydrogen," *Nature materials*, vol. 10, no. 12, pp. 927–931, 2011. (Page 5).

[40] R. T. Howie, C. L. Guillaume, T. Scheler, A. F. Goncharov, and E. Gregoryanz, "Mixed molecular and atomic phase of dense hydrogen," *Physical Review Letters*, vol. 108, no. 12, pp. 1–5, 2012. (Page 5).

[41] R. T. Howie, T. Scheler, C. L. Guillaume, and E. Gregoryanz, "Proton tunneling in phase IV of hydrogen and deuterium," *Physical Review B - Condensed Matter and Materials Physics*, vol. 86, no. 21, pp. 3–8, 2012. (Pages 5, 45).

[42] C. S. Zha, Z. Liu, M. Ahart, R. Boehler, and R. J. Hemley, "High-pressure measurements of hydrogen phase IV using synchrotron infrared spectroscopy," *Physical Review Letters*, vol. 110, no. 21, pp. 1–5, 2013. (Page 5).

[43] C. J. Pickard, M. Martinez-Canales, and R. J. Needs, "Density functional theory study of phase IV of solid hydrogen," *Physical Review B*, vol. 85, p. 214114, jun 2012. (Pages 5, 45, 46, 48, 53).

[44] V. E. Fortov, R. I. Ilkaev, V. A. Arinin, V. V. Burtzev, V. A. Golubev, I. L. Iosilevskiy, V. V. Khrustalev, A. L. Mikhailov, M. A. Mochalov, V. Y. Ternovoi, and M. V. Zhernokletov, "Phase transition in a strongly nonideal deuterium plasma generated by quasi-isentropical compression at megabar pressures," *Physical Review Letters*, vol. 99, no. 18, pp. 2–5, 2007. (Page 7).

[45] J. M. McMahon, M. a. Morales, C. Pierleoni, and D. M. Ceperley, "The properties of hydrogen and helium under extreme conditions," *Reviews of Modern Physics*, vol. 84, pp. 1607–1653, nov 2012. (Pages 7, 74, 85).

[46] C. Pierleoni, M. A. Morales, G. Rillo, M. Holzmann, and D. M. Ceperley, "Liquid–liquid phase transition in hydrogen by coupled electron–ion Monte Carlo simulations," *Proceedings of the National Academy of Sciences*, vol. 113, no. 18, p. 201603853, 2016. (Pages 7, 72, 73, 81).

[47] V. Dzyabura, M. Zaghoo, and I. F. Silvera, "Evidence of a liquid – liquid phase transition in hot dense hydrogen," *Proceedings of the National Academy of Sciences*, vol. 110, no. 20, pp. 8040–8044, 2013. (Pages 6, 83).

[48] P. Hohenberg and W. Kohn, "The Inhomogeneous Electron Gas," *Phys. Rev.*, vol. 136, no. 3B, p. B864, 1964. (Pages 8, 13).

[49] W. Kohn and L. J. Sham, "Self-consistend equations including exchange and correlation effects," *Physical Review*, vol. 140, no. 1951, p. A1133, 1965. (Pages 8, 15, 17).

[50] C. Corminboeuf, F. Tran, and J. Weber, "The role of density functional theory in chemistry: Some historical landmarks and applications to zeolites," *Journal of Molecular Structure: THEOCHEM*, vol. 762, no. 1-3, pp. 1–7, 2006. (Page 8).

[51] R. O. Jones, "Density functional theory: Its origins, rise to prominence, and future," *Reviews of Modern Physics*, vol. 87, no. 3, pp. 897–923, 2015. (Page 8).

[52] M. Born and R. Oppenheimer, "Zur Quantentheorie der Molekeln," *Annalen der Physik*, vol. 389, no. 20, pp. 457–484, 1927. (Page 9).

[53] B. Bransden and C. Joachain, "Physics of Atoms and Molecules (2nd Edition)," 2003. (Page 9).

[54] P. Ballone, "Modeling potential energy surfaces: From first-principle approaches to empirical force fields," *Entropy*, vol. 16, no. 1, pp. 322–349, 2014. (Pages 9, 10).

[55] R. Feynman, *Statistical Mechanics*. 1998. (Pages 10, 26, 28).

[56] W. Kohn, "Theory of the insulating state," *Physical Review*, vol. 133, no. 1A, 1964. (Pages 11, 75).

[57] H. Eschrig, "The Fundamentals of Density Functional Theory (revised and extended version)," *Materials Research*, p. 204, 2003. (Pages 13, 15).

[58] E. Engel and R. M. Dreizler, *Density Functional Theory*. Theoretical and Mathematical Physics, Berlin, Heidelberg: Springer Berlin Heidelberg, 2011. (Pages 13, 15).

[59] N. W. Ashcroft and N. D. Mermin, "Solid State Physics," 1976. (Page 17).

[60] G. Kresse and J. Furthmüller, "Efficient iterative schemes for ab initio total-energy calculations using a plane-wave basis set," *Physical Review B*, vol. 54, no. 16, pp. 11169–11186, 1996. (Pages 18, 54).

[61] G. Kresse and J. Furthmüller, "Efficiency of ab-initio total energy calculations for metals and semiconductors using a plane-wave basis set," *Computational Materials Science*, vol. 6, no. 1, pp. 15–50, 1996. (Page 18).

[62] P. Giannozzi, S. Baroni, N. Bonini, M. Calandra, R. Car, C. Cavazzoni, D. Ceresoli, G. L. Chiarotti, M. Cococcioni, I. Dabo, A. Dal Corso, S. de Gironcoli, S. Fabris, G. Fratesi, R. Gebauer, U. Gerstmann, C. Gougoussis, A. Kokalj, M. Lazzeri, L. Martin-Samos, N. Marzari, F. Mauri, R. Mazzarello, S. Paolini, A. Pasquarello, L. Paulatto, C. Sbraccia, S. Scandolo, G. Sclauzero, A. P. Seitsonen, A. Smogunov, P. Umari, and R. M. Wentzcovitch, "QUANTUM ESPRESSO: a modular and open-source software project for quantum simulations of materials," *Journal of Physics: Condensed Matter*, vol. 21, no. 39, p. 395502, 2009. (Pages 18, 53).

[63] P. Schwerdtfeger, "The pseudopotential approximation in electronic structure theory," *ChemPhysChem*, vol. 12, no. 17, pp. 3143–3155, 2011. (Page 19).

[64] G. Kresse, "From ultrasoft pseudopotentials to the projector augmented-wave method," *Physical Review B*, vol. 59, no. 3, pp. 1758–1775, 1999. (Pages 19, 54).

[65] H. J. Monkhorst and J. D. Pack, "Special points for Brillonin-zone integrations," *Physical Review B*, vol. 16, no. 4, pp. 1748–1749, 1977. (Page 19).

[66] J. P. Perdew, K. Burke, and M. Ernzerhof, "Generalized Gradient Approximation Made Simple," *Physical Review Letters*, vol. 77, no. 18, pp. 3865–3868, 1996. (Page 19).

[67] M. Dion, H. Rydberg, E. Schröder, D. C. Langreth, and B. I. Lundqvist, "Van der Waals density functional for general geometries," *Physical Review Letters*, vol. 92, no. 24, pp. 246401–1, 2004. (Pages 19, 53, 54).

[68] C. W. Gardiner, "Handbook of stochastic methods: For Physics, Chemistry and the Natural Sciences," 1996. (Pages 20, 26, 34).

[69] W. K. Hastings, "Monte carlo sampling methods using Markov chains and their applications," *Biometrika*, vol. 57, no. 1, pp. 97–109, 1970. (Page 20).

[70] M. P. Allen and D. J. Tildesley, *Computer Simulation of liquids*, vol. 18. 1987. (Pages 20, 21).

[71] W. McMillan, "Ground state of liquid He 4," *Physical Review*, vol. 138, no. 2, pp. 442–451, 1965. (Page 22).

[72] D. Ceperley, G. V. Chester, and M. H. Kalos, "Monte Carlo simulation of a many-fermion study," *Physical Review B*, vol. 16, no. 7, pp. 3081–3099, 1977. (Pages 22, 40).

[73] W. M. C. Foulkes, P. C. Road, U. Kingdom, L. Mitas, R. J. Needs, G. Rajagopal, and M. Road, "Quantum Monte Carlo simulations of solids," vol. 73, no. 1, pp. 33–83, 2001. (Pages 22, 23).

[74] T. Kato, "On the eigenfunctions of many-particle systems in quantum mechanics," *Communications on Pure and Applied Mathematics*, vol. 10, pp. 151–177, 1957. (Page 23).

[75] R. T. Pack and B. W. Brown, "Cusp Conditions for Molecular Wavefunctions," *The Journal of Chemical Physics*, vol. 45, no. 2, p. 556, 1966. (Page 23).

[76] R. Jastrow, "Many-body problem with strong forces," *Physical Review*, vol. 98, no. 5, pp. 1479–1484, 1955. (Page 25).

[77] T. Gaskell, "The Collective Treatment of a Fermi Gas: II," *Proceedings of the Physical Society*, vol. 77, no. 6, pp. 1182–1192, 1961. (Page 25).

[78] C. Pierleoni and D. M. Ceperley, *Computer Simulations in Condensed Matter Systems: From Materials to Chemical Biology Volume 1*, vol. 703 of *Lecture Notes in Physics*. Berlin, Heidelberg: Springer Berlin Heidelberg, 2006. (Pages 25, 36, 37, 40, 43).

[79] D. M. Ceperley and B. J. Alder, "Ground state of solid hydrogen at high pressures," *Phys. Rev. B*, vol. 36, pp. 2092–2106, 1987. (Page 25).

[80] M. Holzmann, D. M. Ceperley, C. Pierleoni, and K. Esler, "Backflow correlations for the electron gas and metallic hydrogen.," *Physical review. E, Statistical, nonlinear, and soft matter physics*, vol. 68, no. 4 Pt 2, p. 046707, 2003. (Page 26).

[81] Y. Kwon, D. M. Ceperley, and R. M. Martin, "Effects of Backflow Correlation in the Three-Dimensional Electron Gas: Quantum Monte Carlo Study," vol. 58, no. 11, p. 14, 1998. (Page 26).

[82] C. Pierleoni, K. T. Delaney, M. A. Morales, D. M. Ceperley, and M. Holzmann, "Trial wave functions for high-pressure metallic hydrogen," *Computer Physics Communications*, vol. 179, no. 1-3, pp. 89–97, 2008. (Pages 26, 39).

[83] M. A. Morales, R. Clay, C. Pierleoni, and D. M. Ceperley, "First Principles Methods: A Perspective from Quantum Monte Carlo," *Entropy*, vol. 16, pp. 287–321, 2014. (Pages 27, 39, 74).

[84] G. Rajagopal, R. Needs, A. James, S. Kenny, and W. Foulkes, "Variational and diffusion quantum Monte Carlo calculations at nonzero wave vectors: Theory and application to diamond-structure germanium," *Physical Review B*, vol. 51, no. 16, pp. 591–600, 1995. (Page 27).

[85] N. Byers and C. N. Yang, "Theoretical considerations concerning quantized magnetic flux in superconducting cylinders," *Physical Review Letters*, vol. 7, no. 2, pp. 46–49, 1961. (Page 27).

[86] C. Lin, F. H. Zong, and D. M. Ceperley, "Twist-averaged boundary conditions in continuum quantum Monte Carlo algorithms.," *Physical review. E, Statistical, nonlinear, and soft matter physics*, vol. 64, no. 1 Pt 2, p. 016702, 2001. (Page 27).

[87] M. Holzmann, B. Bernu, and D. M. Ceperley, "Finite-size analysis of the Fermi liquid properties of the homogeneous electron gas," vol. 012020, p. 6, 2011. (Page 27).

[88] D. Ceperley, "Path integrals in the theory of condensed helium," *Reviews of Modern Physics*, 1995. (Pages 28, 29, 32).

[89] A. Klemm and R. Storer, "The structure of quantum fluids: Helium and neon," *Australian journal of physics*, vol. 26, no. October 1971, p. 43, 1973. (Page 32).

[90] M. E. Tuckerman, F. Breu, S. Guggenbichler, and J. Wollmann, "Statistical Mechanics: Theory and Molecular Simulation," *New York*, p. 713, 2010. (Page 32).

[91] M. Ceriotti, M. Parrinello, T. E. Markland, and D. E. Manolopoulos, "Efficient stochastic thermostatting of path integral molecular dynamics," *Journal of Chemical Physics*, vol. 133, no. 2010, 2010. (Pages 33, 34, 35).

[92] G. Bussi and M. Parrinello, "Accurate sampling using Langevin dynamics," *Physical Review E - Statistical, Nonlinear, and Soft Matter Physics*, vol. 75, 2007. (Page 35).

[93] M. Ceriotti, G. Bussi, and M. Parrinello, "Colored-noise thermostats àla Carte," *Journal of Chemical Theory and Computation*, vol. 6, no. 4, pp. 1170–1180, 2010. (Page 35).

[94] M. Ceriotti, D. E. Manolopoulos, and M. Parrinello, "Accelerating the convergence of path integral dynamics with a generalized Langevin equation," *Journal of Chemical Physics*, vol. 134, no. 8, 2011. (Page 35).

[95] M. Ceriotti, J. More, and D. E. Manolopoulos, "I-PI: A Python interface for ab initio path integral molecular dynamics simulations," *Computer Physics Communications*, vol. 185, pp. 1019–1026, 2014. (Page 35).

[96] M. Ceriotti, W. Fang, P. G. Kusalik, R. H. McKenzie, A. Michaelides, M. A. Morales, and T. E. Markland, "Nuclear Quantum Effects in Water and Aqueous Systems: Experiment, Theory, and Current Challenges," *Chemical Reviews*, p. acs.chemrev.5b00674, 2016. (Page 35).

[97] D. Ceperley, M. Dewing, and C. Pierleoni, *The Coupled Electronic-Ionic Monte Carlo Simulation Method*, pp. 473–500. Berlin, Heidelberg: Springer Berlin Heidelberg, 2002. (Page 36).

[98] D. M. Ceperley and M. Dewing, "The Penalty Method for Random Walks with Uncertain Energies," vol. 61801, 2008. (Page 38).

[99] C. Pierleoni, M. A. Morales, G. Rillo, M. Holzmann, and D. M. Ceperley, "Supporting Information for: Liquid–liquid phase transition in hydrogen by coupled electron–ion Monte Carlo simulations," *Proceedings of the National Academy of Sciences*, vol. 113, no. 18, p. 201603853, 2016. (Pages 39, 54).

[100] P. J. Rossky, J. D. Doll, and H. L. Friedman, "Brownian dynamics as smart Monte Carlo simulation," *The Journal of Chemical Physics*, vol. 69, no. 10, p. 4628, 1978. (Page 41).

[101] D. E. Sands, "Introduction to Crystallography," *Advances in Imaging and Electron Physics*, vol. 123, no. C, p. 179, 1993. (Page 45).

[102] C. J. Pickard and R. J. Needs, "Structure of phase III of solid hydrogen," *Nature Physics*, vol. 3, pp. 473–476, may 2007. (Pages 45, 46, 47).

[103] C. Pickard, M. Martinez-Canales, and R. Needs, "Erratum: Density functional theory study of phase IV of solid hydrogen [Phys. Rev. B 85, 214114 (2012)]," *Physical Review B*, vol. 86, no. 5, p. 214114, 2012. (Pages 48, 49, 53).

[104] N. D. Drummond, B. Monserrat, J. H. Lloyd-Williams, P. L. Ríos, C. J. Pickard, and R. J. Needs, "Quantum Monte Carlo study of the phase diagram of solid molecular hydrogen at extreme pressures," *Nature Communications*, vol. 6, p. 7794, 2015. (Pages 49, 52, 71, 87).

[105] H. Liu, L. Zhu, W. Cui, and Y. Ma, "Room-temperature structures of solid hydrogen at high pressures," *Journal of Chemical Physics*, vol. 137, no. 7, pp. 1–8, 2012. (Page 46).

[106] A. F. Goncharov, J. S. Tse, H. Wang, J. Yang, V. V. Struzhkin, R. T. Howie, and E. Gregoryanz, "Bonding, structures, and band gap closure of hydrogen at high pressures," *Physical Review B - Condensed Matter and Materials Physics*, vol. 87, no. 2, pp. 1–8, 2013. (Pages 49, 69).

[107] H. Liu and Y. Ma, "Proton or deuteron transfer in phase IV of solid hydrogen and deuterium," *Physical Review Letters*, vol. 110, no. 2, pp. 1–5, 2013. (Pages 49, 69).

[108] I. B. Magdău and G. J. Ackland, "Identification of high-pressure phases III and IV in hydrogen: Simulating Raman spectra using molecular dynamics," *Physical Review B - Condensed Matter and Materials Physics*, vol. 87, no. 17, pp. 1–8, 2013. (Pages 49, 50, 69, 70).

[109] H. Liu, J. Tse, and Y. Ma, "Robust diffusive proton motions in phase IV of solid hydrogen," *Journal of Physical Chemistry C*, vol. 118, no. 22, pp. 11902–11905, 2014. (Pages 49, 69, 70).

[110] M. a. Morales, J. M. McMahon, C. Pierleoni, and D. M. Ceperley, "Nuclear quantum effects and nonlocal exchange-correlation functionals applied to liquid hydrogen at high pressure," *Physical Review Letters*, vol. 110, no. 6, pp. 1–6, 2013. (Pages 50, 74, 75, 78, 81).

[111] M. a. Morales, J. M. McMahon, C. Pierleoni, and D. M. Ceperley, "Towards a predictive first-principles description of solid molecular hydrogen with density functional theory," *Physical Review B*, vol. 87, p. 184107, may 2013. (Pages 50, 53, 54, 56, 69, 70).

[112] J. Chen, X. Ren, X.-Z. Li, D. Alfè, and E. Wang, "On the room-temperature phase diagram of high pressure hydrogen: an ab initio molecular dynamics perspective and a diffusion Monte Carlo study.," *The Journal of chemical physics*, vol. 141, p. 024501, jul 2014. (Pages 51, 57, 69, 70, 71, 87).

[113] S. Azadi, W. M. C. Foulkes, and T. D. Kuhne, "Quantum Monte Carlo study of high pressure solid molecular hydrogen," *New Journal of Physics*, vol. 15, 2013. (Page 51).

[114] S. Azadi, B. Monserrat, W. M. C. Foulkes, and R. J. Needs, "Dissociation of high-pressure solid molecular hydrogen: Quantum Monte Carlo and anharmonic vibrational study," pp. 1–5, 2014. (Page 51).

[115] B. Monserrat, N. Drummond, and R. Needs, "Anharmonic vibrational properties in periodic systems: energy, electron-phonon coupling, and stress," *Physical Review B*, vol. 87, p. 144302, apr 2013. (Page 51).

[116] J. McMinis, R. C. Clay, D. Lee, and M. a. Morales, "Molecular to Atomic Phase Transition in Hydrogen under High Pressure," *Physical Review Letters*, vol. 114, no. 10, pp. 1–6, 2015. (Pages 51, 52, 71, 87).

[117] R. C. Clay, J. McMinis, J. M. McMahon, C. Pierleoni, D. M. Ceperley, and M. a. Morales, "Benchmarking exchange-correlation functionals for hydrogen at high pressures using quantum Monte Carlo," *Physical Review B - Condensed Matter and Materials Physics*, vol. 89, no. 18, pp. 1–11, 2014. (Pages 53, 54).

[118] A. Soper, "Empirical potential Monte Carlo simulation of fluid structure," *Chemical Physics*, vol. 202, no. 2-3, pp. 295–306, 1996. (Page 55).

[119] M. A. Morales, C. Pierleoni, E. Schwegler, and D. M. Ceperley, "Evidence for a first-order liquid-liquid transition in high-pressure hydrogen from ab initio simulations," *Proceedings of the National Academy of Sciences*, vol. 107, no. 29, pp. 12799–12803, 2010. (Pages 73, 74, 75).

[120] W. Ebeling and W. Richert, "Plasma phase transition in hydrogen," *Physics Letters A*, vol. 108, no. 2, pp. 80–82, 1985. (Page 72).

[121] D. Saumon and G. Chabrier, "Fluid hydrogen at high density: The plasma phase transition," *Physical Review Letters*, vol. 62, no. 20, pp. 2397–2400, 1989. (Page 72).

[122] G. Chabrier, D. Saumon, and W. C., "Hydrogen and Helium at High Density and Astrophysical Implications," *Astrophys. Space Sci.*, vol. 307, pp. 263–267, 2007. (Page 73).

[123] W. R. Magro, D. M. Ceperley, C. Pierleoni, and B. Bernu, "Molecular Dissociation in Hot , Dense Hydrogen," *Physical Review Letters*, vol. 76, no. 8, pp. 1240–43, 1996. (Page 73).

[124] S. Scandolo, "Liquid – liquid phase transition in compressed hydrogen from first-principles simulations," *Proceedings of the National Academy of Sciences*, vol. 100, no. 6, pp. 3051–3053, 2003. (Page 73).

[125] S. A. Bonev, B. Militzer, and G. Galli, "Ab initio simulations of dense liquid deuterium : Comparison with gas gun shock wave experiments," *Phys. Rev. B*, vol. 69, no. 014101, 2003. (Page 73).

[126] R. Car and M. Parrinello, "Unified Approach for Molecular Dynamics and Density-Functional Theory," *Physical Review Letters*, vol. 55, no. 22, pp. 2471–2474, 1985. (Page 73).

[127] B. Holst, R. Redmer, and M. P. Desjarlais, "Thermophysical properties of warm dense hydrogen using quantum molecular dynamics simulations," *Physical Review B - Condensed Matter and Materials Physics*, vol. 77, no. 18, pp. 1–7, 2008. (Pages 74, 84, 85).

[128] W. Lorenzen, B. Holst, and R. Redmer, "First-order liquid-liquid phase transition in dense hydrogen," *Physical Review B - Condensed Matter and Materials Physics*, vol. 82, no. 19, pp. 1–6, 2010. (Pages 74, 84, 85).

[129] B. Holst, M. French, and R. Redmer, "Electronic transport coefficients from ab initio simulations and application to dense liquid hydrogen," *Physical Review B*, vol. 83, no. 23, p. 235120, 2011. (Pages 74, 96).

[130] G. Mazzola, S. Yunoki, and S. Sorella, "Unexpectedly high pressure for molecular dissociation in liquid hydrogen by electronic simulation," *Nature Communications*, vol. 5, no. 3485, pp. 1–6, 2014. (Page 74).

[131] G. Mazzola and S. Sorella, "Distinct Metallization and Atomization Transitions in Dense Liquid Hydrogen," *Physical Review Letters*, vol. 114, no. 105701, pp. 1–5, 2015. (Pages 74, 77, 81).

[132] C. Attaccalite and S. Sorella, "Stable Liquid Hydrogen at High Pressure by a Novel Ab Initio Molecular-Dynamics Calculation," *Physical Review Letters*, vol. 114501, no. March, pp. 1–4, 2008. (Page 74).

[133] P.-o. Lowdin, "Quantum Theory of Many-Particle Systems. I. Density Matrices, Natural Spin-Orbitals, and Convergence Problems in Method of Configuration Interaction," *Physical Review*, vol. 376, no. 17, 1931. (Page 75).

[134] J. D. Cloizeaux, "Energy bands and projection operators in a crystal: Analytic and asymptotic properties," *Physical Review*, vol. 135, no. 3A, 1964. (Page 75).

[135] J. D. Cloizeaux, "Analytical properties of n-dimensional energy bands and wannier functions," *Physical Review*, vol. 135, no. 3A, 1964. (Page 75).

[136] S. Ismail-Beigi and T. A. Arias, "Locality of the Density Matrix in Metals, Semiconductors, and Insulators," *Physical Review Letters*, vol. 82, no. 10, pp. 2127–2130, 1999. (Page 75).

[137] L. He and D. Vanderbilt, "Exponential decay properties of Wannier functions and related quantities," *Physical Review Letters*, vol. 86, no. 23, pp. 5341–5344, 2001. (Page 75).

[138] E. Koch and S. Goedecker, "Locality properties and Wannier functions for interacting systems," *Solid State Communications*, vol. 119, no. 2, pp. 105–109, 2001. (Page 75).

[139] J. Heyd, J. E. Peralta, G. E. Scuseria, R. L. Martin, J. Heyd, J. E. Peralta, G. E. Scuseria, and R. L. Martin, "Energy band gaps and lattice parameters evaluated with the Heyd-Scuseria-Ernzerhof screened hybrid functional Energy band gaps and lattice parameters evaluated with the Heyd- Scuseria-Ernzerhof screened hybrid functional," *Journal of Chemical Physics*, vol. 123, no. 174101, 2005. (Page 78).

[140] R. S. McWilliams, D. A. Dalton, M. F. Mahmood, and A. F. Goncharov, "Optical Properties of Fluid Hydrogen at the Transition to a Conducting State," *Physical Review Letters*, vol. 116, no. 25, pp. 1–6, 2016. (Pages 82, 84).

[141] S. Brygoo, M. Millot, P. Loubeyre, A. E. Lazicki, S. Hamel, T. Qi, P. M. Celliers, F. Coppari, J. H. Eggert, D. E. Fratanduono, D. G. Hicks, J. R. Rygg, R. F. Smith, D. C. Swift, G. W. Collins, and R. Jeanloz, "Analysis of laser shock experiments on precompressed samples using a quartz reference and application to warm dense hydrogen and helium," *Journal of Applied Physics*, vol. 118, p. 195901, nov 2015. (Page 83).

[142] L. E. Reichl, *A Modern Course in Statistical Physics*. A Wiley-Interscience publication, Wiley, 1998. (Page 89).

[143] H. B. Callen, *Thermodynamics and an Introduction to Thermostatistics*. Wiley, 1985. (Page 89).

[144] R. Kubo, "Statistical-mechanical theory of irreversible processes. I. general theory and simple applications to magnetic and conduction problems," *Journal of the Physical Society of Japan*, vol. 12, no. 6, pp. 570–586, 1957. (Page 91).

[145] J. M. Luttinger, "Theory of thermal transport coefficients," *Physical Review*, vol. 135, no. 6A, 1964. (Page 91).

[146] G. D. Mahan, *Many-Particle Physics*. Physics of Solids and Liquids, Springer, 2000. (Pages 91, 92, 93, 94, 96).

[147] G. C. Wick, "The Evaluation of the Collision Matrix," *Phys. Rev.*, vol. 80, pp. 268–272, oct 1950. (Page 95).

[148] G. V. Chester and A. Thellung, "The Law of Wiedemann and Franz," *Proceedings of the Physical Society*, vol. 77, no. 5, pp. 1005–1013, 1961. (Page 95).

[149] D. a. Greenwood, "The Boltzmann Equation in the Theory of Electrical Conduction in Metals," *Proceedings of the Physical Society*, vol. 71, no. 4, pp. 585–596, 1958. (Page 96).

[150] B. Y.-K. Hu, "Kramers–Kronig in two lines," *American Journal of Physics*, vol. 57, no. 9, p. 821, 1989. (Page 97).

[151] G. R. Fowles, "Introduction to Modern Optics," *American Journal of Physics*, vol. 36, no. 8, p. 770, 1968. (Page 97).